4RD SEMESTER, MASTER

ROBUST CONTROL OF HYDRAULIC PITCH SYSTEM.

31 May 2024

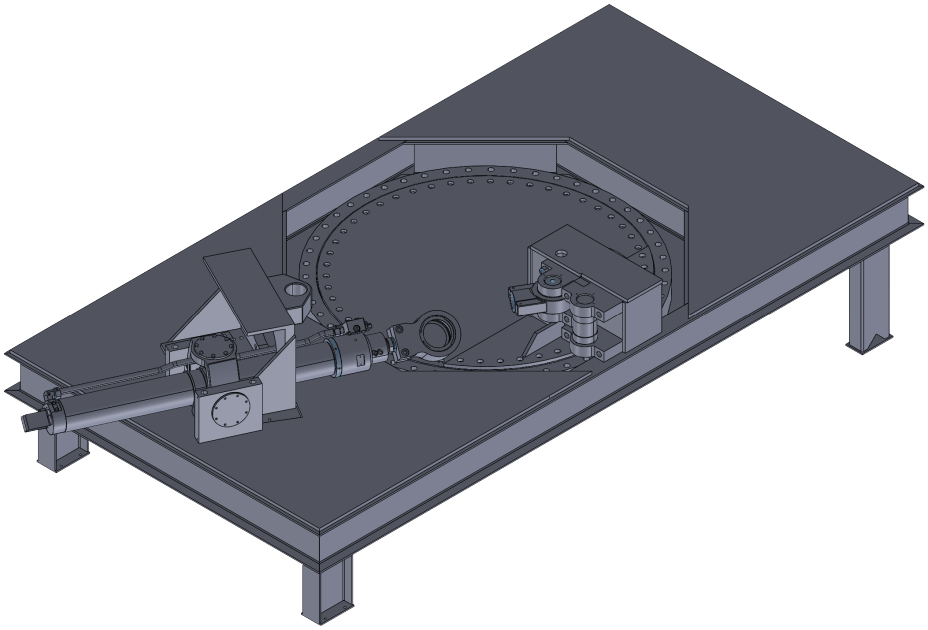

Mechatronic Control Engineering, MCE4-1023
AAU Energy, Aalborg University

AALBORG UNIVERSITY
STUDENT REPORT

AAU Energy
Mechatronic Control Engineering
Pontopidanstræde 111
9220 Aalborg Øst

Title:
Robust Control of Hydraulic pitch system.

Project:
4rd semester, Master

Project period:
5 February to 31 May 2024

Project group:
MCE4-1023

Email:
et-24-mce-4-1023@student.aau.dk

Supervisor:
Henrik C. Pedersen
Mohit Bhola

Pages:
83

Appendices:
21

Participants:
Casper Strøm Pedersen
Magnus Fink

Abstract:

Wind turbines are a huge part of the transition towards renewable energy. Studies have shown that maintenance and downtime of wind turbines are a large contributor to the Cost of Energy, where especially the wind turbine pitch system is the largest contributor to failures and downtime. This project examines the influence of subjecting a pitch system to an internal leakage fault, as studies have shown this fault has the highest Risk Priority Number. Introducing a leakage fault to the pitch system is seen to decrease the performance of the nominal pitch position controller. Therefore, a Fault Tolerant Control strategy is designed to be robust towards internal leakage faults. The FTC design includes using an Unscented Kalman Filter to estimate the internal leakage and load torque. The leakage estimate is then used to design an Active Flow Feed Forward algorithm with leakage compensation to compensate for internal leakage faults. It is in this project shown that the UKF algorithm is capable of accurately estimating internal leakage and load torque, as well as it is found to be very robust towards parameter uncertainties. Including the UKF leakage estimate as a feedback in the design of a Active FFW yields an increased controller performance compared to the nominal position controller designed for a healthy pitch system.

Synopsis

Two of the biggest factors contributing to the Cost of Energy for wind turbines, are maintenance and downtime. The wind turbine pitch system is the biggest contributor to the overall failure rate and is a critical subsystem, as the pitch system ensures safe operation. Within the hydraulic pitch system, internal leakage faults have the highest Risk Priority Number. The focus of this project is therefore to investigate a hydraulic pitch system, how internal leakage faults affects the system and develop a fault tolerant control strategy that is tolerant towards a internal leakage fault. To investigate the pitch system, a non-linear lumped parameter model is developed and linearized in order to use linear system analysis techniques to analyse the system. Furthermore, the linear model is used to design a nominal pitch position controller, which in this project is used as a baseline controller. The designed position controller is a PI-pole controller with an added passive flow feed forward algorithm. The baseline controller is tested in simulations under normal working conditions. These results are then compared to simulations where the pitch system is subjected to a internal leakage fault. Comparison of the results showed a decrease in performance when subjecting the pitch system to a leakage fault. The decrease in performance leads to the design of a Fault Tolerant Control design. This project proposes the design of a strategy that includes estimation of the internal leakage flow. To estimate the leakage an Unscented Kalman Filter is used, due to the very non-linear behaviour of a pitch system. It is here found that the leakage flow can be accurately estimated using an UKF. Additionally, an UKF is used to estimate the load torque disturbance acting on the pitch cylinder, as it was found this increased the performance of the leakage estimation. Through different simulations the UKF estimator is found to be very robust towards parameter uncertainties. To mitigate the effect a leakage fault has on the control performance, this project designs an active flow feed forward algorithm with leakage compensation, as it was found the performance of the passive flow feed forward algorithm decreased significantly, when introduced to a leakage fault. The designed active flow feed forward is added to the nominal controller instead of the passive and tested through various simulations. Using different wind speed pitch reference trajectories, it was found that the new controller increased tracking performance, when subjecting the system to an internal leakage fault. At 7 m/s wind speed the mean tracking error was reduced from 0.048° to 0.021° and at 17 m/s wind speed it was reduced from 0.057° to 0.04°.

Preface

This project is written by the 4rd semester, Master students of group MCE4-1023, studying Mechatronic Control Engineering at Aalborg University. It is written in the period 5 February to 31 May 2024 under the supervision of Henrik C. Pedersen & Mohit Bhola. The project chosen is *Robust Control of Hydraulic pitch system.*

We would like to thank Henrik C. Pedersen & Mohit Bhola for all the help and advice they have given as our supervisors in this project. We would also like to thank our fellow students for bouncing ideas with us and giving feedback.

During the making of this project, the following programs have been used:

- Overleaf LaTeX—For text processing and layout of this report
- MathWorks MATLAB & Simulink—For modelling, calculations, simulation, data processing.
- Draw.io, InkScape, SolidWorks—For creating sketches and diagrams.

Casper Strøm Pedersen

Magnus Fink

Aalborg University, 31 May 2024

Contents

1 Introduction

Wind turbines are one of the major components of the transition towards renewable energy, where it is expected that an increase in wind energy capacity is needed [1]. The increase in demand infers the need for installing more wind turbines, while also increasing the operational demand for each wind turbine.

In offshore wind turbines maintenance and downtime are large factors contributing to the Cost of Energy, due to the difficulty in reaching the turbines to perform maintenance and the large size of the turbines [2]. Since unscheduled maintenance is both costly and takes time due to distances required to travel by sea, it would be beneficial if the turbine could be kept operational in some capacity when a fault occurs.

In Caroll et al. [2] the wind turbine is divided into the different sub systems. Here it is described how the hydraulic pitch system is the main contributor to the overall failure rate of a wind turbine with 13 %. The sub system group 'Other Components' consist of failures to auxiliary components such as lifts, ladders, nacelle seals etc. contributing with 12.2 %. Hereafter, the generator, gearbox and blades contributes with respectively 12.1 %, 7.6 % and 6.2 % failure rates.

As the hydraulic pitch system is the main contributor to the overall failure rate it is chosen as the focus of this project. The main purpose of the pitch system is to accurately control the pitch angle of the turbine blades to maintain safe operation and optimal power production. If a fault degrades the control system performance, a system shutdown can become necessary. However, if the fault effect can be mitigated, performance can be maintained. This lies in the field of Fault Detection and Diagnosis (FDD), and Fault Tolerant Control (FTC).

The objective of the project is then to investigate wind turbine pitch system faults that affect performance, and methods for mitigating these faults.

System Description 2

In this chapter a turbine pitch system will be described. The pitch system centers around a disk that connects the turbine blade to the rotor hub through a bearing. As the bearing disk is fixed to the blade, the angle of the disk is equal to the blade pitch angle. The bearing disk is actuated by a hydraulic cylinder that pushes on the disk at an angle. The pitch cylinder is controlled by a 4/3 proportional valve connected to a accumulator which is periodically refilled by a Hydraulic Power Unit (HPU) in the turbine nacelle, connected through a hydraulic rotary union. The pitch cylinder incorporates flow regeneration when pitching out of the wind. Additionally a locking circuit is incorporated, along with safety systems for the hydraulic circuits, and a cooling circuit. A hydraulic diagram of a wind turbine pitch system can be seen Figure 2.1.

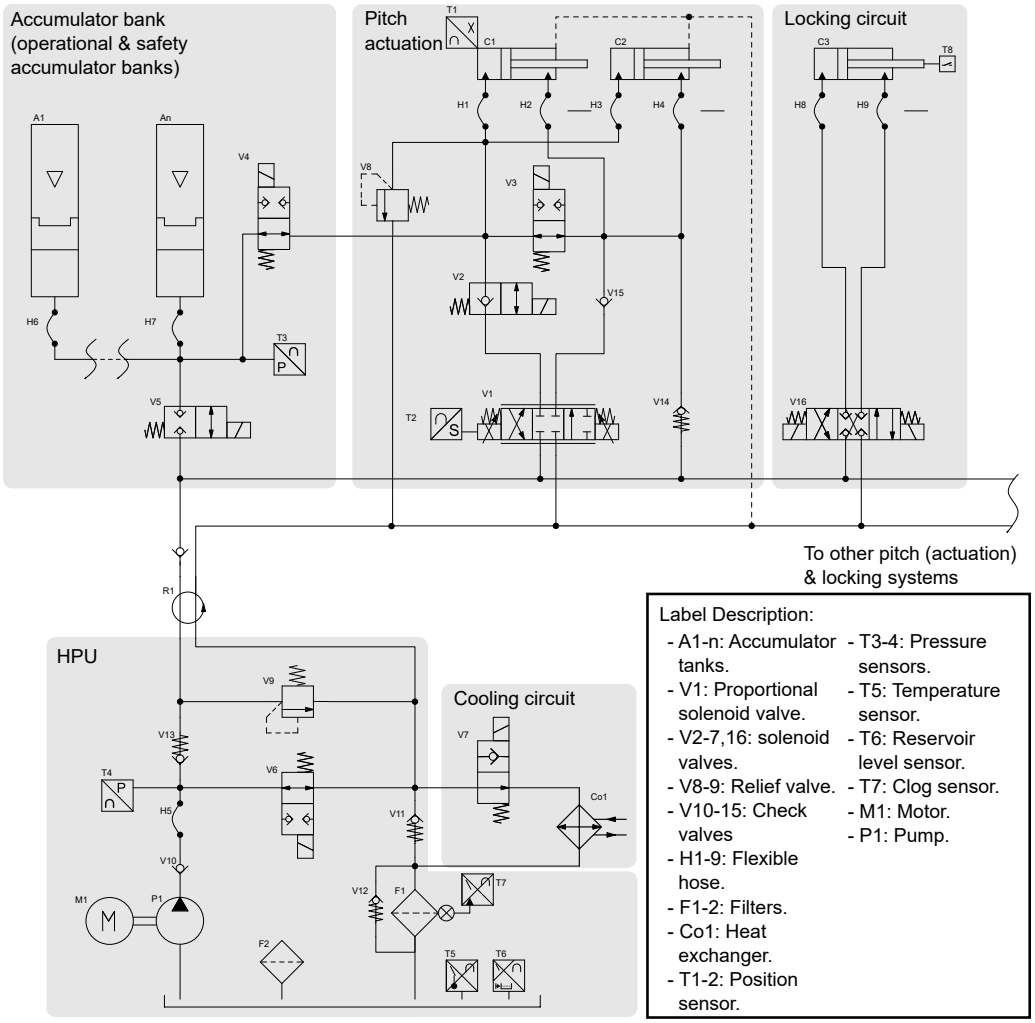

Figure 2.1. Hydraulic diagram of a turbine pitch system. All valves are shown as de-energized.

2.1 Fault Review

As described in Chapter 1 the focus of this project is to maintain pitch control performance in the presence of faults. To do this first an understanding of the possible faults in the system is required. Many papers have been written on this subject, therefore this section will be based on such work. The following list of faults is based on the work by Alessio Dallabona et al. [3].

Friction fault

Increased friction in the cylinder and bearing. This can be caused by sludge formation in the hydraulic oil, cylinder and cylinder component wear, bearing lubricant degradation or other damage. This fault will degrade system performance, and can become critical if friction becomes too high.

Oil degradation fault

Change in parameters related to the hydraulic oil. Can be caused be e.g. gas leaking into the oil from the gas loaded accumulators. This fault will affect the bulk modulus of the oil, which will affect system dynamics.

Leakage fault

Oil leakage from the cylinder to the exterior or between the cylinder chambers, known as external and internal leakage respectively. This can be caused by e.g. seal wear or production defects. Depending on the cause of the fault the effect can be slow or abrupt. External leakage can be quit severe, as even a small leakage can drain the system over time, leading to full turbine shutdown. Internal leakage is not as severe, it will, however, affect the systems dynamic behavior, and can degrade system performance.

Valve fault

Faults relating to the valve. This can be changes in opening area characteristics, valve spool command offset, valve actuator degradation or valve position sensor drop-out. As long as the valve is able to operate a valve fault is generally not severe, however if the valve is stuck it becomes very severe.

Accumulator fault

Gas leakage in the accumulator, specifically the effect it has on the accumulator. Generally caused by gas leaking into the hydraulic oil or out of the accumulator. This fault will result in a reduction in gas volume, which will reduce performance, and is generally slow varying. This fault becomes severe if the accumulator can no longer function, as it is a major component in safety systems.

Sensor Fault

Faults relating to sensor measurements. Severity of these faults is dependent of which sensor is affected. Since the position sensor for the pitch cylinder has no redundancy, a fault in this sensor is very severe.

Caroll et al. [2] describes the overall failure contribution within the hydraulic pitch system. Here oil issues contribute with 17 % of the overall failures, where oil issues consists of leakage faults

and unscheduled oil changes. 13 % of the overall failures are due to valve faults in the system and 10 % of the fault contribution is due to the accumulator. Furthermore, Liniger [4] presents the Risk Priority Number (RPN) for different fault in a hydraulic pitch system, where it is found that an internal leakage fault has the highest RPN.

Friction faults can have a significant impact on system dynamics, but it is also very hard to detect [3], and its occurrence is in the lower end of the spectrum [4]. Oil (specifically bulk modulus) and leakage faults are easier to detect, while also impacting the system dynamics [3]. Accumulator faults have a less significant impact on dynamic behavior of the pitch system, and are therefore less relevant for this project. Finally sensor faults, specifically cylinder position sensor drop-out has a critical impact on the pitch control system.
Based on its high occurrence, Risk Priority Number and effect on the system dynamics, the internal leakage fault is chosen as the focus of this project.

2.2 AAU Test Setup

This project will take offset in the Hydraulic Pitch System test setup at AAU. This is a full scale test bench for a 3 MW wind turbine pitch system. The test setup consist of a large bearing disk, a pitch actuation cylinder with accompanying control valve, an accumulator tank and a HPU. The test setup also has a second load cylinder to imitate wind loading on the pitch system. As this load cylinder is not a part of an actual turbine pitch system it will not be included in this project. Additional hydraulic systems such as the pitch locking, safety and cooling systems are also not included as these have little to no impact on the pitch control. Figure 2.2 shows a diagram of the simplified pitch system.

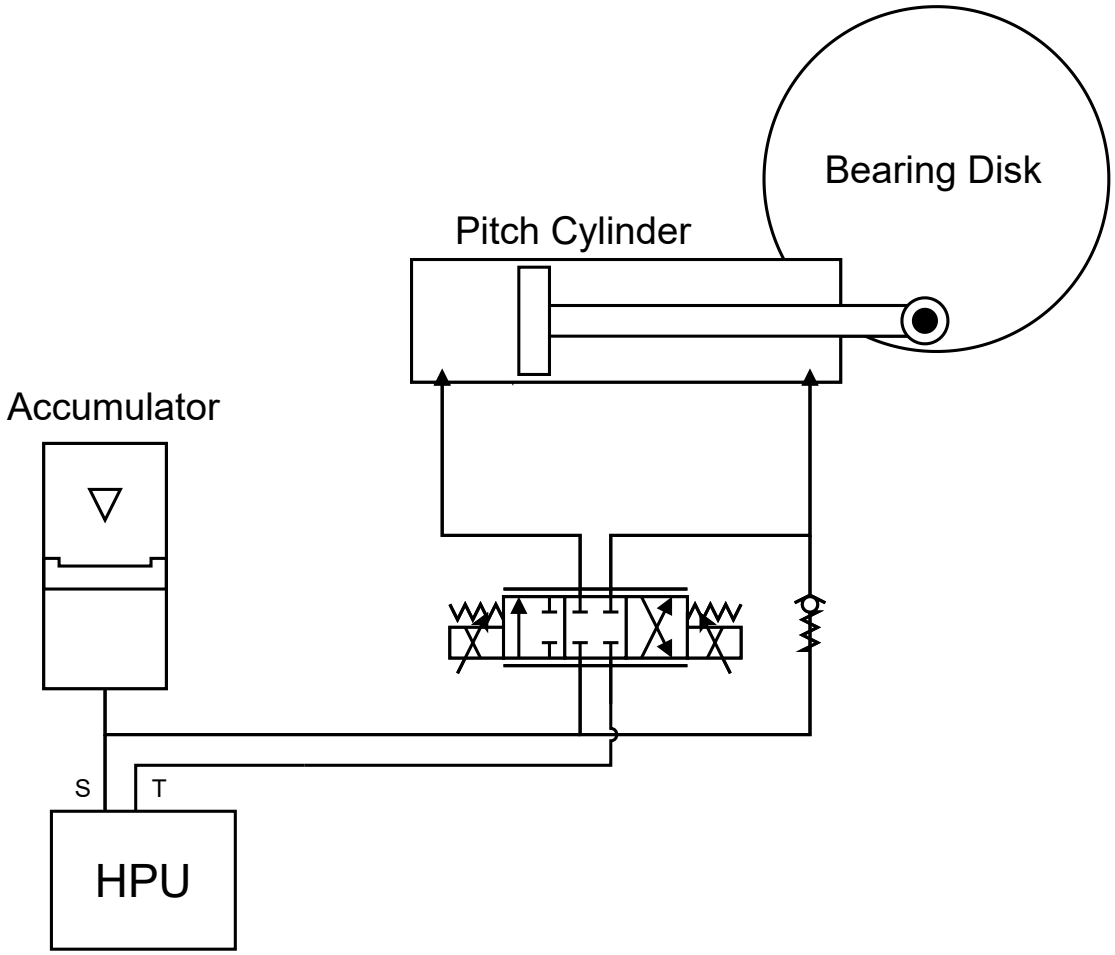

Figure 2.2. Simplified diagram of the AAU hydraulic pitch system test setup.

In this setup there are pressure sensors on the two cylinder chambers and the accumulator, and a linear position sensor on the pitch cylinder. The pressure sensor measurements have a standard deviation of ≈0.2 bar and the position sensor measurement has a standard deviation of ≈0.5 cm. The pitch controller is assumed to run at a sampling frequency of $Fs = 1\,\text{kHz}$.

Due to technical issues with the AAU test setup it will not be possible to perform test, or get any measurement data from the setup, however all modelling will still be based on this setup even though it can not be validated or tested on.

2.3 FAST

The simulation studies of this project takes offset in the FAST software developed by the National Renewable Energy Laboratory (NREL). The FAST software simulates the working conditions of a 5 MW offshore wind turbine [5] [6]. Figure 2.3 shows a block diagram of the FAST simulation model structure. The interest of this project is to focus on the pitch system of a wind turbine, with the purpose of developing a pitch angle position controller that is fault tolerant towards leakage faults. This project uses the FAST software to obtain different pitch angle references,

$\theta_{p_{ref}}$, as well as the corresponding blade pitch load torques, τ_{load}. The blade pitch load torque extracted from FAST is the load torque seen on each pitch cylinder. In Chapter 3 the wind turbine pitch system is modelled with the purpose of using the model to design pitch position controller as well as testing the designed controllers.

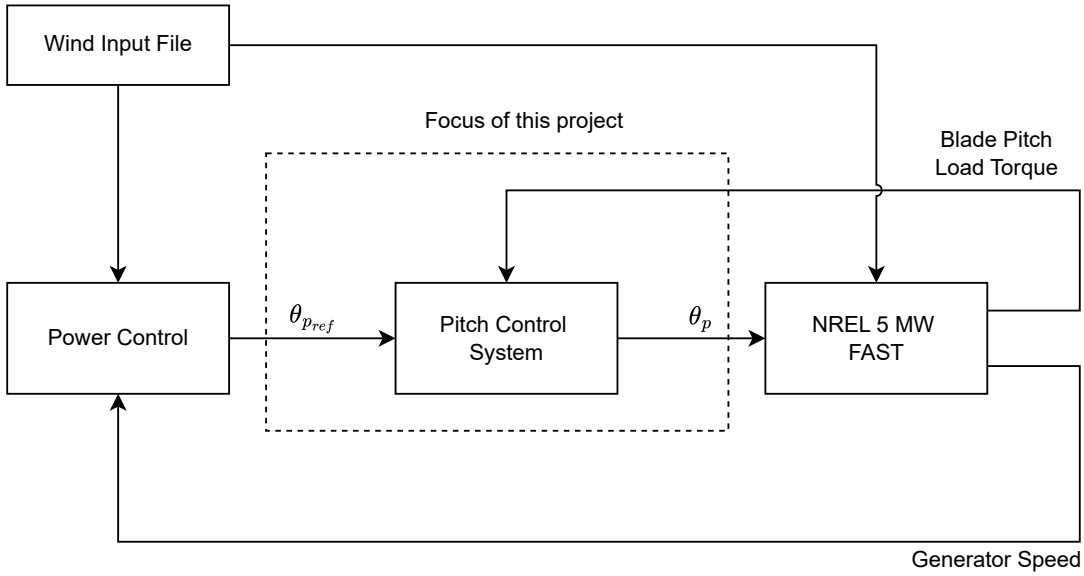

Figure 2.3. Block diagram of the FAST software.

The obtained pitch angle references and blade pitch load torques are seen in Figures 2.4 and 2.5 for different mean wind speeds. It is noted that for all the simulations the wind turbine rotor speed is 12 RPM.

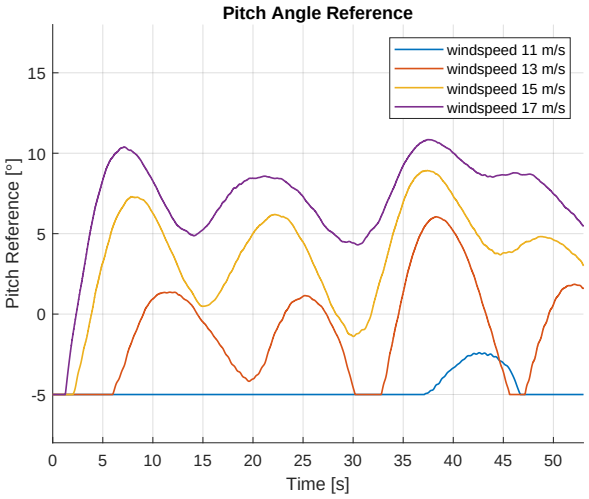

Figure 2.4. Pitch reference at different mean windspeeds. The data is taken from the FAST software.

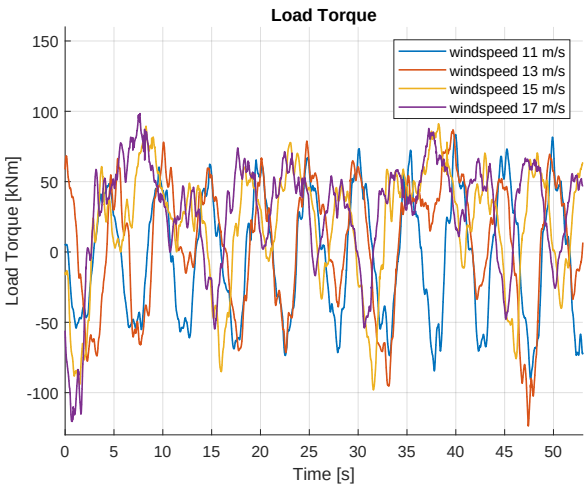

Figure 2.5. Load torques at different mean windspeeds. The data is taken from the FAST software.

In this project $-5°$ pitch reference has been used as the zero pitch angle, meaning that the

turbine blade is pitched fully into the wind at this angle. The wind load data is generated using an IECKAI turbulence model with 'NTM' type turbulence and turbulence characteristic 'A'.

Non-linear model of Wind Turbine Pitch System 3

In this chapter a non-linear model of the wind turbine pitch system is derived. Firstly, the hydraulic model of the pitch system is derived, including a model of the proportional valve. In the non-linear hydraulic model the supply pressure is assumed constant, however a model of the accumulator is derived if a varying supply pressure is needed. Hereafter, a mechanical model of the pitch system is derived applying the Euler Lagrange equation.

3.1 Hydraulic Model

A diagram of the hydraulic system that actuates the pitch cylinder can be seen in Figure 3.1. The figure shows the different flow directions as well as the control volumes, which is the two cylinder chambers denoted V_p and V_r. The supply pressure is assumed constant in this section, however for the accumulator model the volume V_{acc} is also considered a control volume.

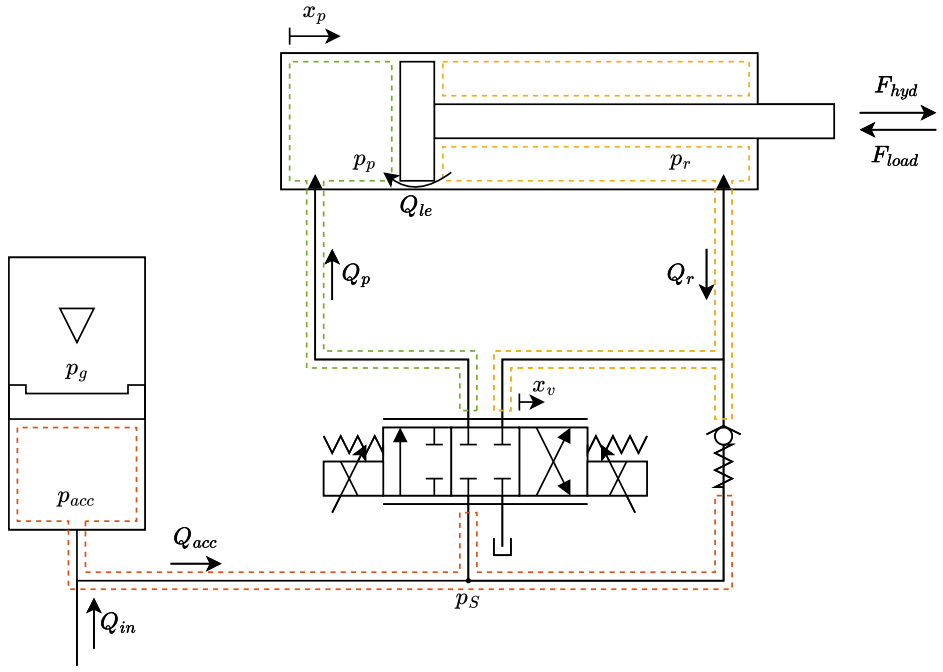

Figure 3.1. Diagram of the hydraulic system with definitions for flow, force and movement directions shown. The three separate volumes are highlighted with different colors.

Considering the flows, it is seen that the flow Q_p is defined positive flowing into V_p and the flow Q_r is defined negative when flowing into V_r. For positive valve spool position, Q_p flows through

the proportional valve while Q_r flows through the check valve. The flow through the check valve is modelled as a laminar flow, with the cracking pressure being, $p_{cr} = 5\,\text{bar}$. For a negative spool position both flows flow through the proportional valve. The orifice equations describing the flows are seen in Equations (3.1) and (3.2).

$$Q_p(t) = \begin{cases} C_{dva}A_{va}(|x_v(t)|)\sqrt{\frac{2}{\rho}}\sqrt{|p_S(t) - p_p(t)|} \cdot \text{sign}(p_S(t) - p_p(t)), & x_v > 0 \\ C_{dvr}A_{vr}(|x_v(t)|) \cdot \text{sign}(x_v)\sqrt{\frac{2}{\rho}}\sqrt{|p_p(t) - p_T|} \cdot \text{sign}(p_p(t) - p_T), & x_v < 0 \end{cases} \tag{3.1}$$

$$Q_r(t) = \begin{cases} C_{qr}(p_r(t) - (p_S(t) + p_{cr}(t))), \quad p_r > p_S + p_{cr}, & x_v > 0 \\ C_{dvb}A_{vb}(|x_v(t)|) \cdot \text{sign}(x_v)\sqrt{\frac{2}{\rho}}\sqrt{|p_S(t) - p_r|} \cdot \text{sign}(p_S(t) - p_r), & x_v < 0 \end{cases} \tag{3.2}$$

The leakage flow, which is defined to be positive flowing into the piston side chamber, is modelled as a laminar flow in Equation (3.3).

$$Q_{le}(t) = C_{le}(p_r(t) - p_p(t)) \tag{3.3}$$

The control volumes, V_p and V_r, are modelled by the continuity equation. The effective bulk modulus is modelled as a function of both air content and the respective chamber pressures. The effective bulk modulus model is further described in Subsection 3.1.1. The continuity equations are expressed in Equations (3.4) and (3.5).

$$\dot{p}_p(t) = \frac{\beta_{eff}(p_p(t))}{V_p(x_p(t))}\Big(Q_p(t) + Q_{le}(t) - \dot{V}_p(\dot{x}_p(t))\Big) \tag{3.4}$$

$$\dot{p}_r(t) = \frac{\beta_{eff}(p_r(t))}{V_r(x_p(t))}\Big(- Q_r(t) - Q_{le}(t) - \dot{V}_r(\dot{x}_p(t))\Big) \tag{3.5}$$

The respective control volumes and the change in volumes are position and velocity dependent respectively. Equations (3.6) to (3.9) describe the volumes and the change in volumes with respect to time, where V_{p_0} and V_{r_0} are constant volumes describing the dead volumes of the system such as hose volumes.

$$V_p(x_p(t)) = V_{p0} + A_p \cdot x_p(t) \tag{3.6}$$

$$V_r(x_p(t)) = V_{r0} + A_r(x_{p_{max}} - x_p(t)) \tag{3.7}$$

$$\dot{V}_p(\dot{x}_p(t)) = A_p \cdot \dot{x}_p(t) \tag{3.8}$$

$$\dot{V}_r(\dot{x}_p(t)) = -A_r \cdot \dot{x}_p(t) \tag{3.9}$$

The hydraulic model and the mechanical model derived in the next section is combined by the hydraulic force acting on the bearing disk. The hydraulic force acting on the bearing disk is given in Equation (3.10).

$$F_{hyd} = A_p \cdot p_p - A_r \cdot p_r \tag{3.10}$$

The friction of the cylinder is not accounted for in the hydraulic force equation, but is included as a part of the friction in the bearing disk in the mechanical model. The parameters used for the hydraulic model of the pitch system is seen in Table 3.1:

Parameters

Name	Value	Description
p_S	210 bar	Supply Pressure
p_T	1 bar	Tank pressure
V_{p0}	$3.7 \cdot 10^{-4}$ m^3	Piston side dead volume
V_{r0}	$1.5 \cdot 10^{-4}$ m	Rod side dead volume
p_{cr}	5 bar	Crack pressure of the check valve
C_{qr}	$1.8 \cdot 10^{-8}$ m^3/(s bar)	Linear flow coefficient of check valve
C_{le}	1.258 L/min/hbar	Leakage coefficient
A_p	0.0154 m^2	Piston side area of pitch cylinder
A_r	0.009 m^2	Rod side area of pitch cylinder
C_{dva}, C_{dvr} and C_{dvb}	0.6	Discharge coefficient for valve orifices
$x_{p_{max}}$	1.314 m	Pitch cylinder max stroke
ρ	885 kg/m^3	Oil density

Table 3.1. The parameters used in modelling the hydraulics of the pitch system.

3.1.1 Effective Bulk Modulus

According to [7] the effective bulk modulus can be modelled as Equation (3.11):

$$\beta_{eff} = \frac{(1-\alpha) \cdot e^{\left(\frac{p_{atm}-p}{\beta_0}\right)} + \alpha \left(\frac{p_{atm}}{p}\right)^{\frac{1}{n}}}{\frac{1-\alpha}{\beta_0} \cdot e^{\left(\frac{p_{atm}-p}{\beta_0}\right)} + \frac{\alpha}{np_{atm}} \left(\frac{p_{atm}}{p}\right)^{\frac{n+1}{n}}} \tag{3.11}$$

Where α is the air content of the fluid, p_{atm} is the atmospheric pressure, p is the fluid pressure, n is the adiabatic index and β_0 is the fluid bulk modulus. Table 3.2 showcases the different parameters used for the model which can be seen in Figure 3.2.

Parameter	β_0	α	n
Value	10000 bar	0.04 %	1.4

Table 3.2. Parameters used for the Effective Bulk Modulus model.

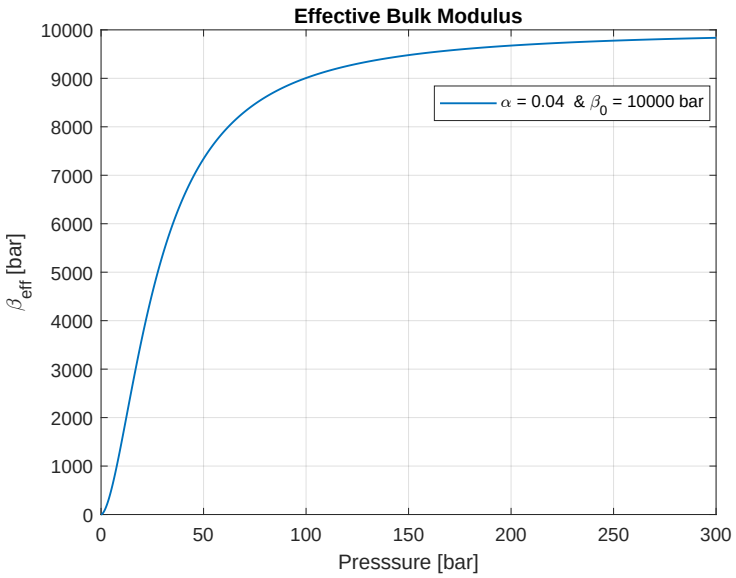

Figure 3.2. Effective bulk modulus.

3.1.2 Valve Model

The proportional valve used for the pitch system is the 4/3 Bosch Rexroth proportional directional valve of type 4WREE. The response and flow characteristics of the valve are found in the valve datasheet [8]. The closed loop bode plot of the valve dynamics is seen in Figure 3.3, where the frequency response shows that for frequencies below 100 Hz, the response can be approximated by a second order system. As will be shown later the system dynamics is below 100 Hz and therefore the valve is approximated by the second order system seen in Equation (3.12):

$$G_{valve}(s) = \frac{X_v(s)}{X_{v_{ref}}(s)} = \frac{\omega_n^2}{s^2 + 2 \cdot \zeta \cdot \omega_n \cdot s + \omega_n^2} \tag{3.12}$$

Figure 3.4 shows the step response of the valve, where from the closed loop system is assumed to be critically damped as there is no overshoot. The natural eigenfrequency of the system is determined from Figure 3.3 to be 50 Hz, as the natural eigenfrequency of a second order system corresponds to the phase being equal to $-90°$ such that $-90° = \angle G_{valve}(j \cdot \omega_n)$. In Figure 3.3 three different bode plots can be seen corresponding to different spool position references. The natural eigenfrequency is determined from the $\pm 10\%$ signal as this is the fastest response. When implemented in the non-linear simulation model a slew rate is therefore also implemented. The slew rate is determined as the slope of the step responses of the left side of Figure 3.4. Table 3.3 shows the valve model parameters:

Parameter	ω_n	ζ	Slew Rate
Value	50 Hz	1	35.4 m/s

Table 3.3. Parameters of the valve model

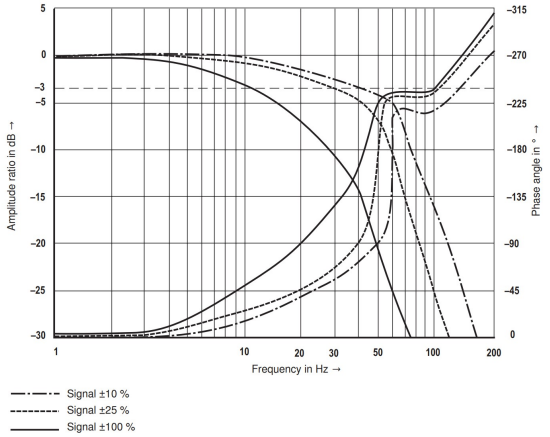

Figure 3.3. Closed loop bodeplot of the 4/3 Bosch Rexroth proportional directional valve[8].

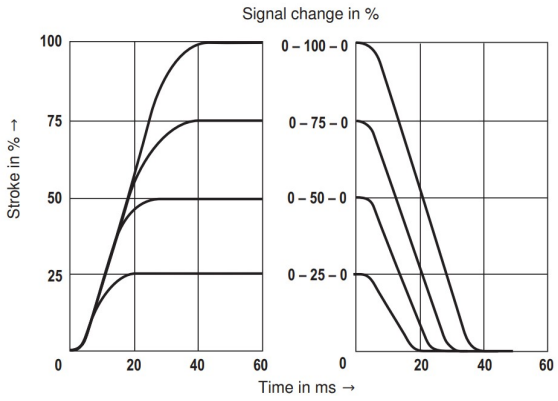

Figure 3.4. Step response of the 4/3 Bosch Rexroth proportional directional valve [8].

In Section 3.1 the orifice flows through the proportional valve is modelled using the orifice equation seen in Equation (3.13).

$$Q = C_d \cdot A(x_v) \cdot \sqrt{\frac{2}{\rho}} \cdot \sqrt{\Delta p} \tag{3.13}$$

$$\Updownarrow$$

$$A(x_v) = \frac{Q}{C_d \cdot \sqrt{\frac{2}{\rho}} \cdot \sqrt{\Delta p}} \tag{3.14}$$

Figure 3.5 shows the flow characteristic of the valve, where from the area characteristic of the valve with respect to the valve spool position, x_v, is found. Assuming a discharge coefficient of, $C_d = 0.6$ the area characteristic with respect to the normalized spool position is determined using polynomial regression and $\Delta p = 50\,bar, \rho = 869\,\mathrm{kg/m^3}$. The area characteristic with respect to the normalized valve spool position is given in Equation (3.15), and the polynomial coefficients are given in Table 5.1:

$$A(x_v) = a_7 x_v^7 + a_6 x_v^6 + a_5 x_v^5 + a_4 x_v^4 + a_3 x_v^3 + a_2 x_v^2 + a_1 x_v + a_0 \tag{3.15}$$

Area Polynomial Coefficients

Coefficient	a_7	a_6	a_5	a_4
Value	-0.0016	0.0051	-0.006	0.0031
	a_3	a_2	a_1	a_0
	$-5.9 \cdot 10^{-4}$	$1.03 \cdot 10^{-4}$	$-6.8 \cdot 10^{-6}$	$-2.2 \cdot 10^{-9}$

Table 3.4. The polynomial coefficients for the approximated valve area characteristic.

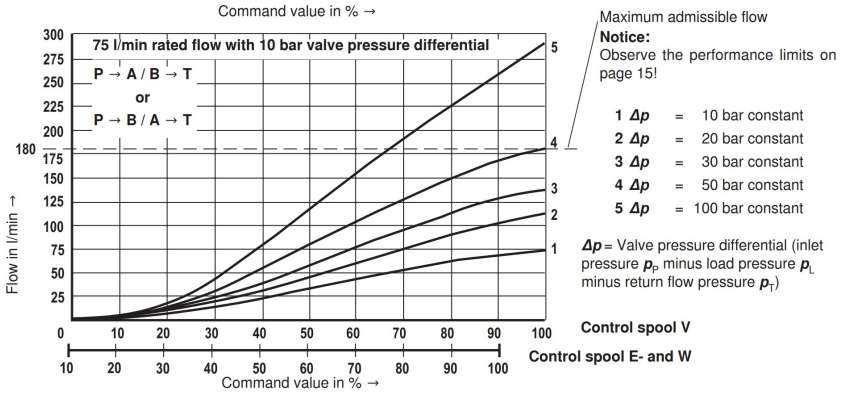

Figure 3.5. Flow characteristic of the 4/3 Bosch Rexroth proportional directional valve [8].

3.1.3 Accumulator Model

The accumulator for the pitch system is a gas loaded piston accumulator. The purpose of modelling the accumulator is to be able to model a varying supply pressure. Here a simple accumulator model is used, which is described in [7], where it is assumed that the gas is an ideal gas undergoing an adiabatic process. This entails that the poly-tropic index used for this model is, $n = 1.4$. Under the assumption that the gas in the accumulator undergoes an adiabatic process the ideal gas law is used to model the pressure of the gas:

$$p_g \cdot V_g^n = \text{Constant} \tag{3.16}$$

$$\Updownarrow \tag{3.17}$$

$$p_g = \frac{p_{g0} \cdot V_{g0}^n}{V_g^n} \tag{3.18}$$

Where the volumes of the accumulator cylinder is given as:

$$V_{acc}(x_{acc}(t)) = V_{acc_0} + A \cdot x_{acc}(t) \tag{3.19}$$

$$V_g(x_{acc}(t)) = V_{g0} - A \cdot x_{acc}(t) \tag{3.20}$$

The supply pressure delivered from the accumulator is then described using the continuity equation to describe the change of pressure and newtons second law describing the movement of the cylinder piston position:

$$\ddot{x}_{acc} = \frac{1}{m_{acc}} \left(A \cdot p_{acc} - A \cdot p_g - F_{fr}(\dot{x}_{acc}) \right) \tag{3.21}$$

$$\dot{p}_{acc} = \frac{\beta_{acc}}{V_{acc}(x_{acc})} \left(Q_{acc} - A \cdot \dot{x}_{acc} \right) \tag{3.22}$$

Where Q_{acc} is the input flow supplied from the pump and F_{fr} is modelled as viscous friction. The parameters used for the accumulator model is given in Table 3.5:

Parameters

Name	Value	Description
$x_{acc_{max}}$	1 m	Max stroke length of accumulator piston
A	0.2121 m^2	Accumulator piston area
V_{g0}	0.2121 m^3	Initial gas volume
V_{acc0}	0.02 m^3	Hydraulic dead volume
$B_{v_{acc}}$	700 N s/m	Viscous friction constant
m_{acc}	50 kg	Accumulator piston mass
β_{acc}	10 000 bar	Accumulator bulk modulus
p_{g0}	10 bar	Initial gas pressure

Table 3.5. The parameters used in modelling the accumulator of the pitch system.

3.2 Mechanical Model

A simplified diagram of the pitch system can be seen in Figure 3.6.

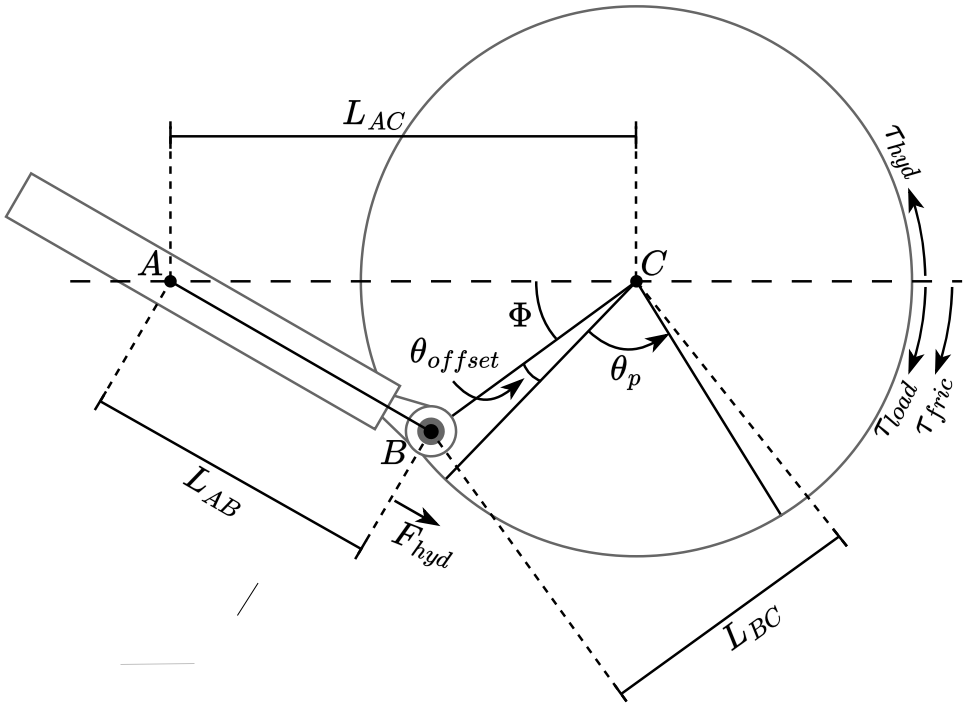

Figure 3.6. Simplified diagram of the turbine pitch system

Here θ_p is the pitch angle, in the range $-8°$ to $82°$, with the blade fully out of the wind at $\theta_p = 82°$, and fully into the wind at $\theta_p = -5°$. A is the point around which the pitch cylinder rotates, B is the point where the pitch cylinder connects to the bearing disk, and C is the center of the bearing disk.
The Parameters used to model the mechanics of the pitch system are seen in Table 3.6:

Parameters

Name	Value	Description
$x_{p_{max}}$	1.314 m	Pitch cylinder max stroke
m_P	104 kg	Pitch cylinder mass
J_b	280 kgm^2	Pitch bearing inertia
L_{AB}	1.251 m	Length between pitch cylinder mounting points in fully retracted position
L_{BC}	0.985 m	Length from pitch cylinder tip mount to bearing center
L_{AC}	1.87 m	Length between pitch cylinder root mount and bearing center
Φ	38°	Angle between center line and pitch cylinder tip mount at fully retracted position
θ_{offset}	8°	Angle offset between $\theta_p = 0°$ and $x_p = 0$ m
$\theta_{p_{max}}$	82°	Max pitch angle
B_v	175 Nm/(°/s)	Viscous friction constant
$\tau_{coulomb}$	2000 Nm	Coulomb friction constant

Table 3.6. The parameters used in the modelling of the mechanics of a pitch system.

Since the pitch cylinder is linked to the bearing disk, extension of the pitch cylinder, x_p, can be described by pitch angle θ_p. Equation (3.23) showns the relation between θ_p and x_p, derived using the cosine relation.

$$x_p(\theta_p) = \sqrt{L_{AC}^2 + L_{BC}^2 - 2L_{AC}L_{BC}\cos\left(\Phi + \theta_p + \theta_{off}\right)} - L_{AB} \tag{3.23}$$

A variable gearing can then be found from this relation by finding the Drive Jacobian of x_p with regards to θ_p:

$$\mathcal{J}(\theta_p) = \frac{\partial x_p}{\partial \theta_p}, \qquad \dot{x}_p = \mathcal{J}(\theta_p) \cdot \dot{\theta}_p \tag{3.24}$$

A graph of this gearing function is shown in Figure 3.8, with the relation between x_p and θ_p shown in Figure 3.7.

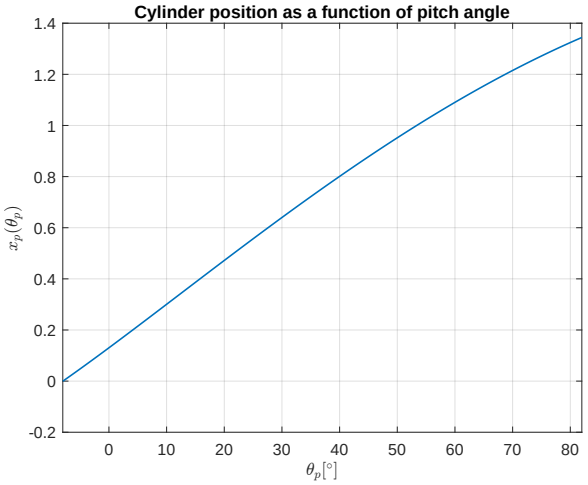

Figure 3.7. The pitch cylinder position x_p plotted as a function of pitch angle.

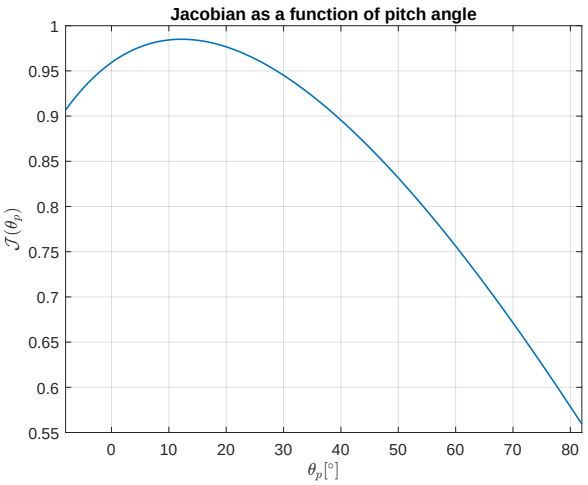

Figure 3.8. The Drive Jacobian plotted as a function of pitch angle.

By assuming no power loss in the gearing between x_p and θ_0, the cylinder torque on the bearing disk can also be found using the Drive Jacobian:

$$\tau_{hyd} = F_{hyd} \cdot \mathcal{J}(\theta_p) \tag{3.25}$$

Dynamics

To model the dynamics of the mechanical part of the turbine pitch system the Euler-Lagrange equation is used. This method is chosen as it gives a well-structured approach for modelling dynamics of a multi-body system, while resulting in a model well-suited for control purposes [9]. The Euler-Lagrange equation is shown in Equation (3.26);

$$\tau_{ext} = \frac{\partial}{\partial t}\left(\frac{\partial \mathcal{L}}{\partial \dot{q}}\right) - \frac{\partial \mathcal{L}}{\partial q} \tag{3.26}$$

with τ_{ext} being the external torque, $\mathcal{L}$ being the Lagrangian, and q being the generalized coordinates. In this case the pitch angle θ_p is chosen as the generalized coordinate. The left side of Equation (3.26) represent the non-conservative forces acting on the system, while the right side represents the conservative forces. The external torque includes the torque exerted by the hydraulic pitch cylinder, the load torque exerted by the wind and friction torques:

$$\tau_{ext} = \tau_{hyd} - \tau_{fric} - \tau_{load} \tag{3.27}$$

With friction torque being described as:

$$\tau_{fric} = B_v \cdot \dot{\theta}_p + \tau_{coulomb} \cdot \tanh\left(K_{tanh} \cdot \dot{\theta}_p\right) \tag{3.28}$$

Where B_v and $\tau_{coulomb}$ are combined values for the cylinder and bearing disk, and K_{tanh} is a constant that adjusts the hyperbolic tangent curve.
The Lagrangian describes the difference between kinetic ($\mathcal{K}$) and potential ($\mathcal{P}$) energy in the system, so therefore equations for the kinetic and potential energy of the system must be set up. The kinetic energy of the system is described in Equation (3.29) as the sum of rotational and translational kinetic energy of all bodies of the system.

$$\mathcal{K} = \tfrac{1}{2} m_p \dot{x}_p(\theta_p(t))^2 + \tfrac{1}{2} J_b \dot{\theta}_p(t)^2 \tag{3.29}$$

$$= \frac{1}{2}\Big(m_p \mathcal{J}(\theta_p(t))^2 + J_b\Big) \cdot \dot{\theta}_p(t)^2 \tag{3.30}$$

Here the rotational kinetic energy of the pitch cylinder is neglected, as this simplifies the model, and the rotational speed and inertia of the cylinder is assumed to be significantly smaller than that of the bearing disk. Equation (3.29) is rewritten to Equation (3.30) by inserting Equation (3.24).
The potential energy is determined to be zero, therefore the Lagrangian becomes:

$$\mathcal{L} = \mathcal{K} - \mathcal{P} \tag{3.31}$$

$$= \frac{1}{2}\Big(m_p \mathcal{J}(\theta_p(t))^2 + J_b\Big) \cdot \dot{\theta}_p(t)^2$$

The two terms of Equation (3.26) can now be calculated;

$$\frac{\partial}{\partial t}\left(\frac{\partial \mathcal{L}}{\partial \dot{\theta}_p}\right) = \left(m_p \mathcal{J}(\theta_p(t))^2 + J_b\right)\ddot{\theta}_p(t) + 2m_p \mathcal{J}(\theta_p(t)\dot{\mathcal{J}}(\theta_p(t))\dot{\theta}_p(t)^2 \tag{3.32}$$

$$\frac{\partial \mathcal{L}}{\partial \theta_p} = m_p \mathcal{J}(\theta_p(t)\dot{\mathcal{J}}(\theta_p(t))\dot{\theta}_p(t)^2 \tag{3.33}$$

and an equation for the acceleration of the bearing disk can be found:

$$\tau_{ext} = \left(m_p \mathcal{J}(\theta_p(t))^2 + J_b\right)\ddot{\theta}_p(t) + m_p \mathcal{J}(\theta_p(t)\dot{\mathcal{J}}(\theta_p(t))\dot{\theta}_p(t)^2 \tag{3.34}$$

$$\Updownarrow$$

$$\ddot{\theta}_p(t) = \frac{\tau_{ext} - m_p \mathcal{J}(\theta_p(t)\dot{\mathcal{J}}(\theta_p(t))\dot{\theta}_p(t)^2}{m_p \mathcal{J}(\theta_p(t))^2 + J_b} \tag{3.35}$$

3.3 Summary

The non-linear system equations have been described and a simulation model is set up. As mentioned in Chapter 2 the AAU test setup is not available for testing, therefore the model cannot be validated at this time. However, the pitch test setup is a well examined system, that has been modelled and validated before. The parameters in this project are based on a previous validated model of the pitch test setup made by AAU [10]. Therefore it is assumed that the non-linear pitch system model is a good representation of the actual system.

System Analysis 4

In this chapter the wind turbine pitch system is analyzed with the purpose of designing a nominal controller for the system. This chapter utilizes linear analysis techniques, therefore the chapter includes a section where the non-linear model is linearized. The linear analysis includes investigating the influence of varying certain parameters as well as investigating different linearization points.

4.1 Linear Model

In this section the non-linear model derived in Chapter 3 is linearized. The model is linearized using the first order Taylor approximation given in Equation (4.1).

$$\Delta f(\mathbf{x}) = \frac{\delta f(\mathbf{x})}{\delta x_1}\bigg|_{\mathbf{x_0}} \Delta x_1 + ... + \frac{\delta f(\mathbf{x})}{\delta x_n}\bigg|_{\mathbf{x_0}} \Delta x_n = k_1 \Delta x_1 + ... + k_n \Delta x_n \tag{4.1}$$

Inserting the orifice equations into the continuity equations, the linear model is represented as in Equations (4.2) to (4.4).

$$\Delta\ddot{\theta}_p = k_1\Delta p_p + k_2\Delta p_r + k_3\Delta\dot{\theta}_p + k_4\Delta\tau_{load} + k_5\Delta\theta_p \tag{4.2}$$

$$\Delta\dot{p}_p = \beta_{p_0}\left(k_6\Delta x_v + k_7\Delta p_p + k_8\Delta p_r + k_9\Delta\dot{\theta}_p + k_{10}\Delta\theta_p\right) \tag{4.3}$$

$$\Delta\dot{p}_r = \beta_{r_0}\left(k_{11}\Delta x_v + k_{12}\Delta p_r + k_{13}\Delta p_p + k_{14}\Delta\dot{\theta}_p + k_{15}\Delta\theta_p\right) \tag{4.4}$$

$k_1(+)$	$k_2(-)$	$k_3(-)$	$k_4(-)$	$k_5(\pm)$
$k_6(+)$	$k_7(-)$	$k_8(+)$	$k_9(-)$	$k_{10}(\pm)$
$k_{11}(-)$	$k_{12}(-)$	$k_{13}(+)$	$k_{14}(+)$	$k_{15}(\pm)$

Table 4.1. A overview of the sign of the linear model coefficients, where a (-) means the constant is negative, a (+) means the constant is positive and a ($\pm$) means the constant can be both positive and negative depenedent on the linearization point.

The linear model represented is a general linear model that is valid for both positive and negative valve spool positions. Here is is noted that when changing between positive and negative spool position the equations for k_6, k_7, k_{11} and k_{12} change due to the orifice equation, whereas the rest are independent of the spool position. Table 4.1 provides an overview of the sign of the coefficients as it is found some of the different coefficients are dependent of both pitch angle and velocity. Furthermore, it is assumed that the bulk modulus, β_p and β_r are constants. This assumption is valid for working pressures above 50 bar, which can be seen in Figure 3.2 on

page 12 showing the bulk modulus model used in this project. To further emphasize the validity of this assumption, it is noted that due to the design of the pitch system, the pressure p_r is almost constant at supply pressure and the pressure p_p rarely drops below 50 bar. However, the influence of the bulk modulus is later analyzed by varying the bulk modulus parameter to investigate the dynamic influence it has in the system.

Through Equations (4.5) to (4.8) the linear model is represented in state space form where, **A** is the state matrix, **B** is the input matrix, **D** is the disturbance matrix and **C** is the output matrix.

$$\dot{\mathbf{x}} = \mathbf{Ax} + \mathbf{Bu} + \mathbf{Dd} \tag{4.5}$$

$$\mathbf{y} = \mathbf{Cx} \tag{4.6}$$

$$\mathbf{x} = \begin{bmatrix} \theta_p & \dot{\theta}_p & p_p & p_r \end{bmatrix}^T \qquad u = x_v \qquad d = \tau_{load} \tag{4.7}$$

$$\mathbf{A} = \begin{bmatrix} 0 & 1 & 0 & 0 \\ k_5 & k_3 & k_1 & k_2 \\ \beta_{p_0} k_{10} & \beta_{p_0} k_9 & \beta_{p_0} k_7 & \beta_{p_0} k_8 \\ \beta_{r_0} k_{15} & \beta_{r_0} k_{14} & \beta_{r_0} k_{13} & \beta_{r_0} k_{12} \end{bmatrix} \quad \mathbf{B} = \begin{bmatrix} 0 \\ 0 \\ \beta_{p_0} k_6 \\ \beta_{r_0} k_{11} \end{bmatrix} \quad \mathbf{C} = \begin{bmatrix} 1 & 0 & 0 & 0 \\ 0 & 0 & 1 & 0 \\ 0 & 0 & 0 & 1 \end{bmatrix} \quad \mathbf{D} = \begin{bmatrix} 0 \\ k_4 \\ 0 \\ 0 \end{bmatrix} \tag{4.8}$$

4.1.1 Linearization Points

Since some of the linearization constants will depend on the states and the input, values for these must be found to linearize the system. To do so the non-linear system equations are solved in steady state:

$$0 = \mathbf{F}(\theta_p, \dot{\theta}_p, p_p, p_r, x_v) = \begin{bmatrix} \ddot{\theta}_p \\ \dot{p}_p \\ \dot{p}_r \end{bmatrix} \tag{4.9}$$

Since there are three equations to solve and five unknowns, and since the bounds of θ_p and $\dot{\theta}_p$ are known, a set of values are chosen for θ_p and $\dot{\theta}_p$. This set of values are chosen to be within the normal working range of the pitch system. The remaining three variables are found using the $fsolve()$ command in MatLab. Based on the pitch reference data in Chapter 2 on page 3, θ_p and $\dot{\theta}_p$ are chosen in the range shown in Table 4.2:

	Min	Max
θ_p	-5°	20°
$\dot{\theta}_p$	$\pm 1.72 \frac{^\circ}{\mathrm{s}}$	$\pm 8.02 \frac{^\circ}{\mathrm{s}}$

Table 4.2. Working range of θ_p and $\dot{\theta}_p$.

4.1.2 Linear Model Validation

To ensure that the model is linearized correctly it is validated against the non-linear model. This is done by initializing both the linear and non-linear models with values from the selected

linearization point and then giving them both a 1 ms impulse. Since the linear model is derived using change variables, the linearization point values are added to the state output of the linear model and subtracted from the input to the linear model. Validation Results can be seen in Figure 4.1 and 4.2.

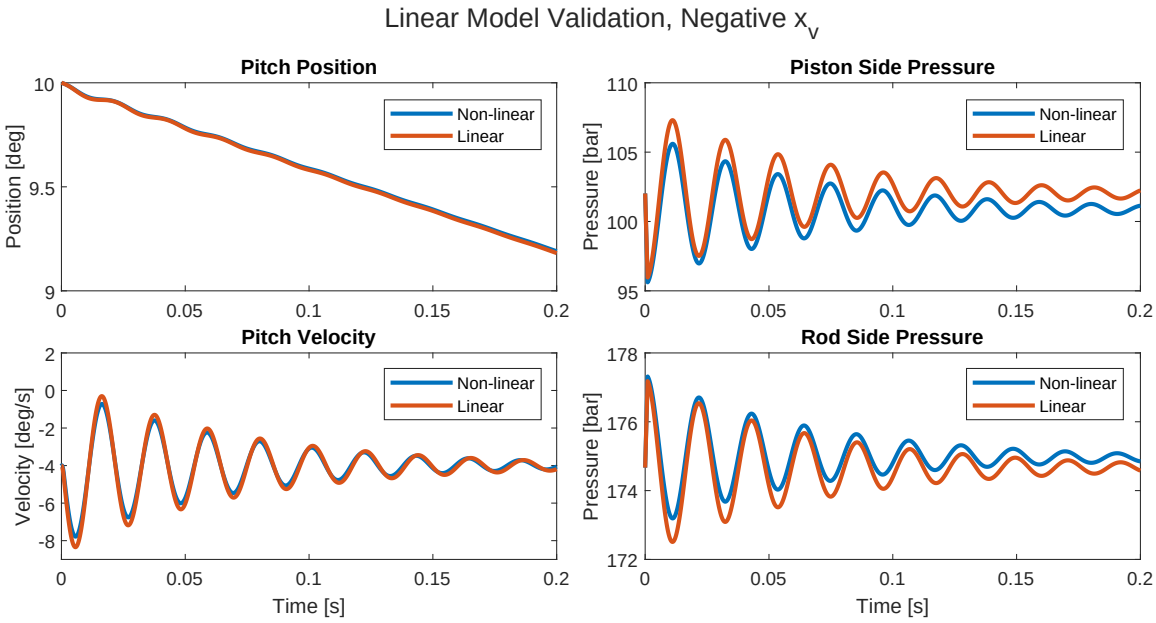

Figure 4.1. Comparison of the linear and non-linear models when given an impulse in the negative direction.

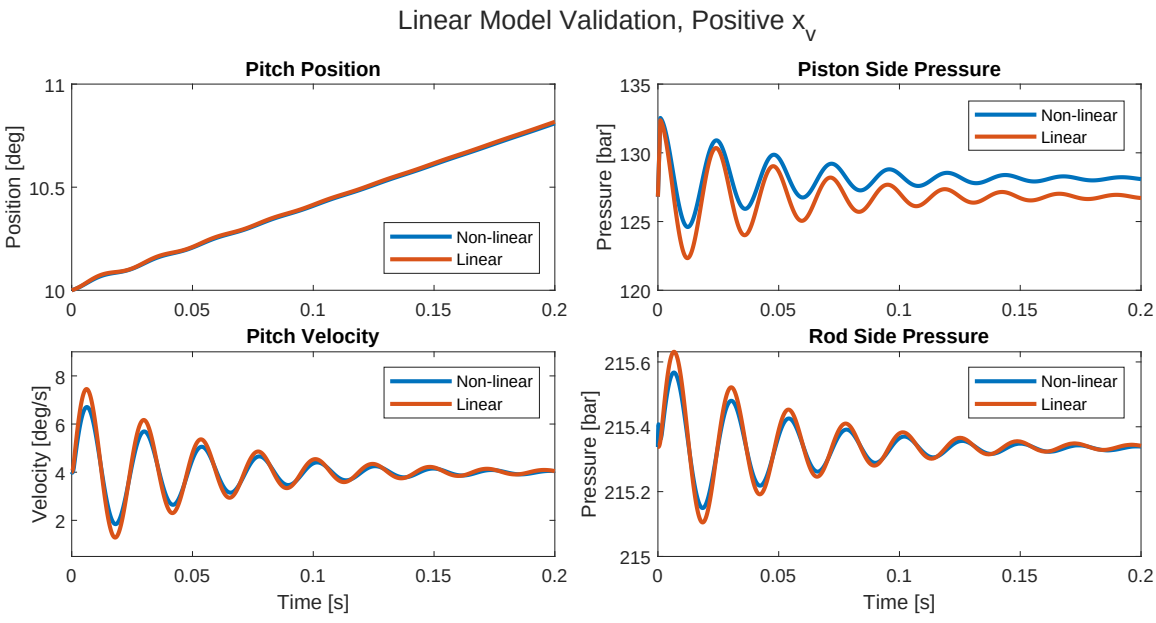

Figure 4.2. Comparison of the linear and non-linear models when given an impulse in the negative direction.

It should be noted that the pitch position measurement shown for the linear model is the integral of the linear velocity, with linearization point offset added. This is shown instead of the position output of the linear model, as this output would be constant when the linear velocity is equal

to the linearization speed. The offset between the linear and non-linear pressures is found to be due to Coulomb friction in the non-linear model. The reason for there not being an offset in the rod side pressure in the positive direction is due to the actuator valve setup. As can be seen in Figure 4.1 and 4.2, the frequency, phase and damping matches for all states. Based on this the linear model is determined to be validated.

4.2 Frequency Analysis

With the linear model done, the system can be analysed using linear analysis technique's. Figure 4.3 shows the Bode plot of the pitch system at different linearization points within the working range.

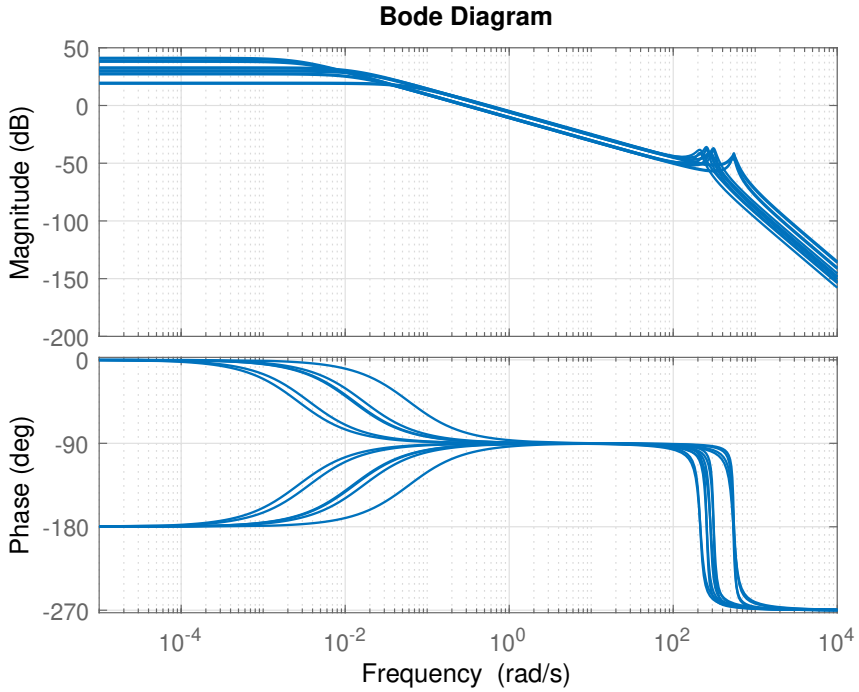

Figure 4.3. System Bode plots for different linearization points

Here it can be seen that pitch system is a Type 0 system with an under-damped 2^{nd} order pole between 10^2 and 10^3 $\frac{rad}{s}$ creating a resonance peak, and a 1^{st} order pole at between 10^{-3} and 10^{-1} $\frac{rad}{s}$. It can seen that in some linearization points the phase starts in -180° and breaks upward at the 1^{st} order pole instead of starting at 0° and breaking downward as would be expected. This indicates that for some linearization points the 1^{st} order pole moves into the right hand plane, making the system a non-minimum phase system that is unstable for low feedback gains. This is also evident when looking at a pole-zero map for the linearization points, as shown in Figure 4.4 and 4.5.

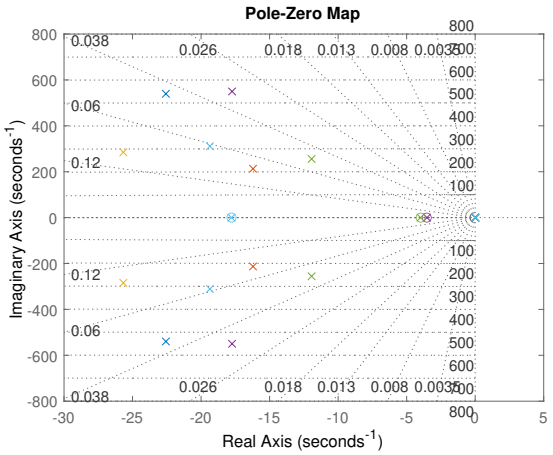

Figure 4.4. Pole-zero map of the system at different linearization points. Each color represents a separate linearization point.

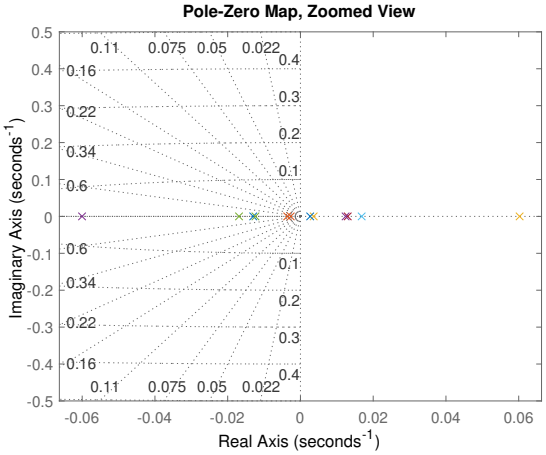

Figure 4.5. Zoomed view of the pole-zero map shown in Figure 4.4.

From Figure 4.5 the 1^{st} order pole can be observed moving to the right hand plane for some linearization points. Since Bode plots cannot always correctly interpret closed loop stability of non-minimum phase systems, care should be taken to verify stability of the closed loop system once control has been developed. From this point forward a pole starting with a phase of $-180°$ that breaks upward at the pole, while the magnitude breaks downward, will be interpreted as a pole in the right hand plane for this system.
Figure 4.4 also shows that the system has a pole-zero pair, that moves together in the different linearization point, which is not visible in the bode plot of Figure 4.3. This indicates that the pole-zero pair is placed so close together that they have no effect on the frequency response, and can therefore be neglected.

To gain a better understanding of how the system is affected by different linearization points, Bode plots are made where pitch angle and velocity are varied separately, and only in one direction at a time. These plots are shown in Figures 4.6 through 4.9.

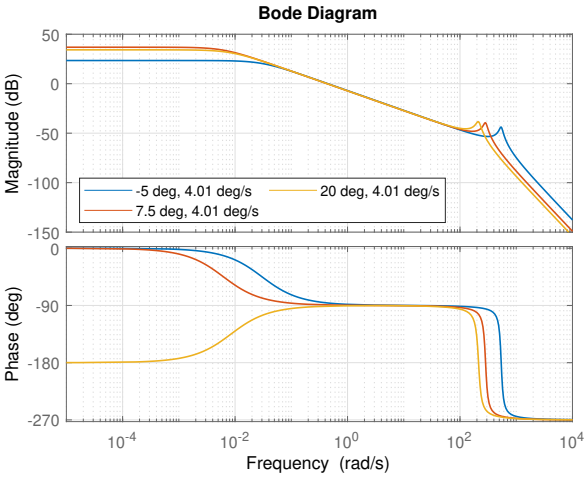

Figure 4.6. Bode plot of varying pitch angle in the positive direction.

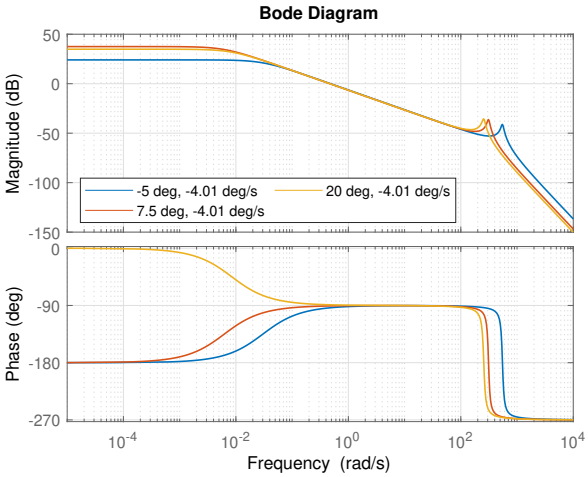

Figure 4.7. Bode plot of varying pitch angle in the negative direction.

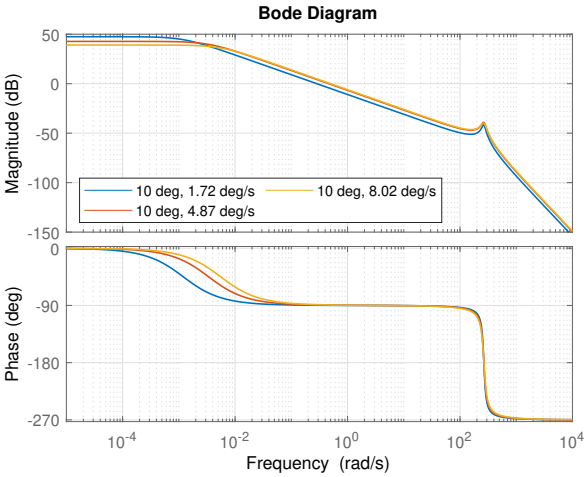

Figure 4.8. Bode plot of varying pitch velocity in the positive direction.

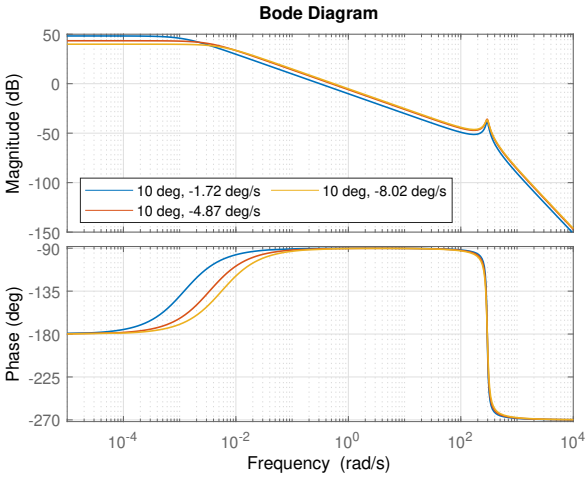

Figure 4.9. Bode plot of varying pitch velocity in the negative direction.

Here it can be seen that pitch angle affects the location of the resonance peak and the location of the 1^{st} order pole, while pitch velocity mostly affects the location of the 1^{st} order pole, with only minor changes to the damping of the resonance peak and a slight change in location based on direction. From Figure 4.8 and 4.9 it can also be seen that at a pitch angle of 10° the 1^{st} order is placed in the left hand plane for positive pitch velocities and placed in the right hand plane for negative velocities. However from Figure 4.6 and 4.7 it can be seen that somewhere between 7.5° and 20° the pitch angle trend reverses. It is found that this reverse in trend occurs at 12.2° pitch angle, which corresponds to the point where the gradient of the Drive Jacobian changes sign, as shown in Figure 4.10

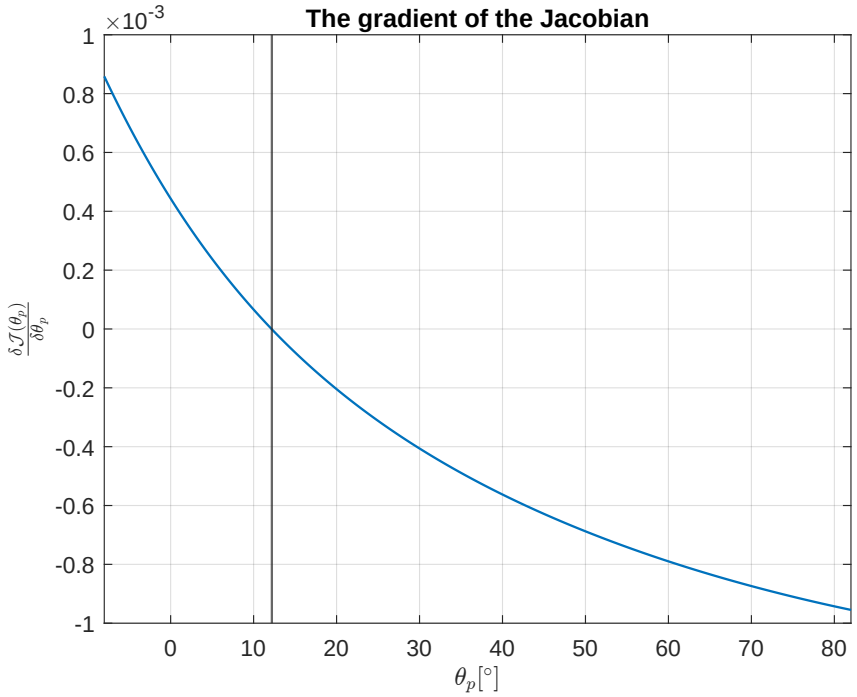

Figure 4.10. Gradient of the drive jacobian, with the zero-crossing angle marked.

Based on this it is determined that the shape of the bode plot for this system is both direction and position dependent.

4.2.1 Parameter Variation

Since some of the system parameters might vary or are hard to estimate accurately, variations of certain parameters are analysed in the frequency domain. These parameters include; Leakage coefficient, bulk modulus, oil density ρ and supply pressure. The variation range chosen for this analysis is shown in Table 4.3:

	C_{le}	β_r	β_p	p_S
Min	1 L/min/hbar	6000 bar	4000 bar	180 bar
Max	50 L/min/hbar	15 000 bar	12 000 bar	210 bar
	ρ	B_v	$\tau_{coulomb}$	τ_{load}
Min	850 kg/L	0 Nm s/°	0 kNm	−100 kNm
Max	900 kg/L	2000 Nm s/°	6 kNm	100 kNm

Table 4.3. Variation ranges.

For some of the parameters this range is beyond what would be considered probable. This is done to also gain an understanding of how the system behaves under extreme circumstances. First looking at the leakage coefficient, in Figure 4.11 it can be seen that leakage has a significant impact on the placement of the 1^{st} order pole, even in the range 1 to 5 L/min/hbar. The leakage coefficient is also seen to have a slight impact on the damping of the 2^{nd} order pole. It is also noted that, all though not shown here, regardless of direction, increasing the leakage will move

the 1^{st} order pole to the left hand plane.
In Figure 4.12 it can be seen that ρ has a significant impact on the DC gain and the location of the 1^{st} order pole. p_s on the other hand has little to no effect on the system, when within the variation range, except for a 0.5 dB change in DC gain, as shown in Figure 4.13.
Figure 4.14 shows the damping effect of viscous friction coefficient. The plot shows that a viscous friction coefficient of 2000 Nm s/° results in the system being close to critically damped.

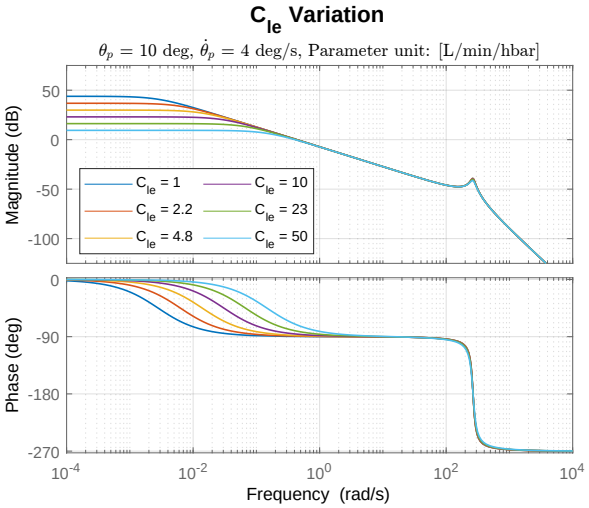

Figure 4.11. Bode plot of varying leakage.

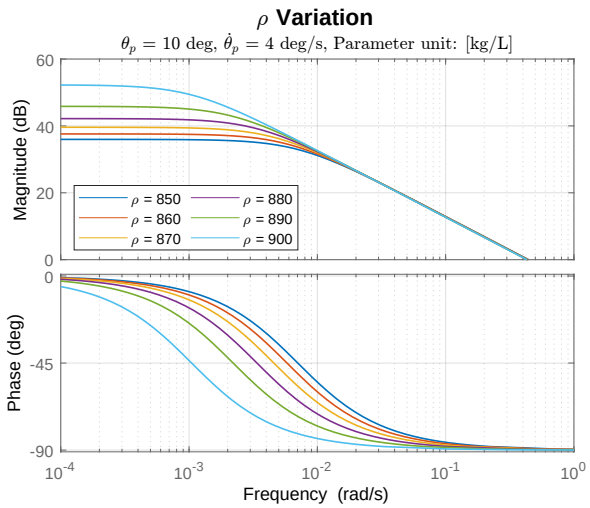

Figure 4.12. Bode plot of varying oil density.

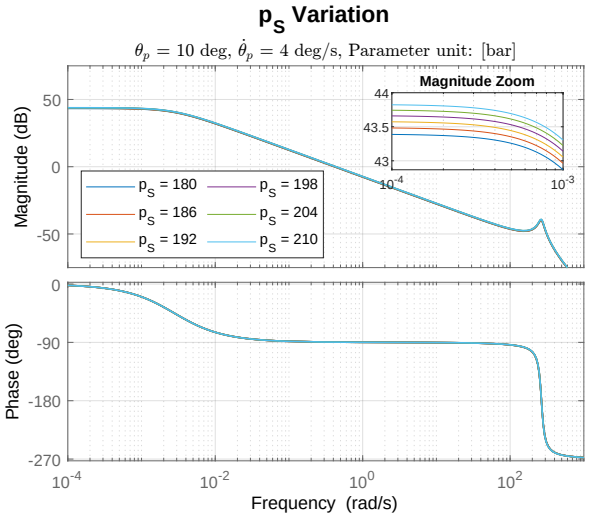

Figure 4.13. Bode plot of varying supply pressure.

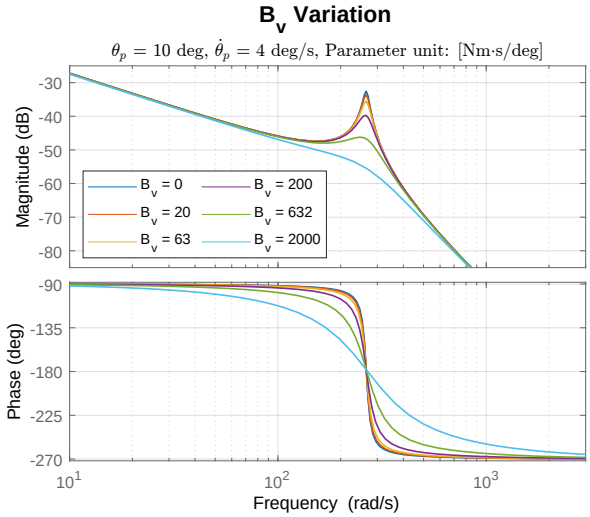

Figure 4.14. Bode plot of varying viscous friction.

The impact of Coulomb friction and load torque is shown in Figure 4.15 and 4.16 respectively. Here it can be seen that the variation range of Coulomb friction has little to no effect on the linearized system, while the load torque gives a variation of a few dB in the DC gain.

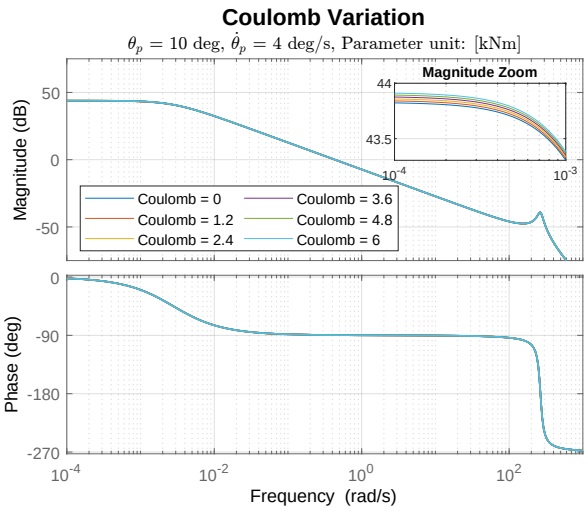

Figure 4.15. Bode plot of varying coulomb friction constant.

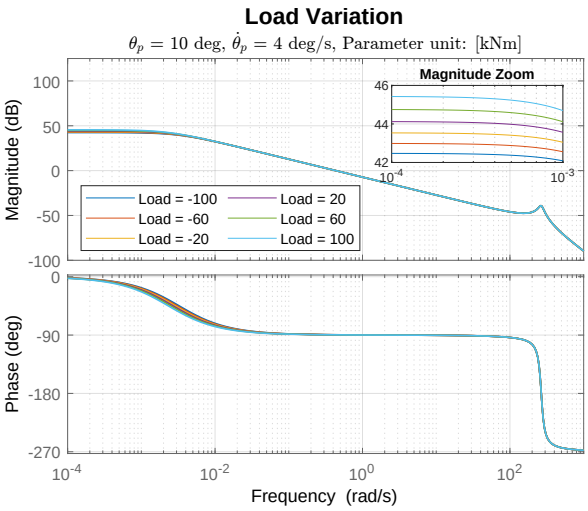

Figure 4.16. Bode plot of varying load torque.

Finally, variations in bulk modulus is tested. Here it is found that the bulk modulus of the piston side chamber moves the 2^{nd} pole a not insignificant amount, without affecting the damping, as shown in Figure 4.17. This should be taken into account during control design, especially when modifying the dynamics around the 2^{nd} order pole. The bulk modulus of the rod side chamber is found to have a small impact on the system in the negative direction, as can be seen in Figure 4.18. In the position direction rod side bulk modulus is found to have no impact on dynamics. This makes sense as the rod side chamber operates close to supply pressure in the positive direction, due to the actuator valve configuration.

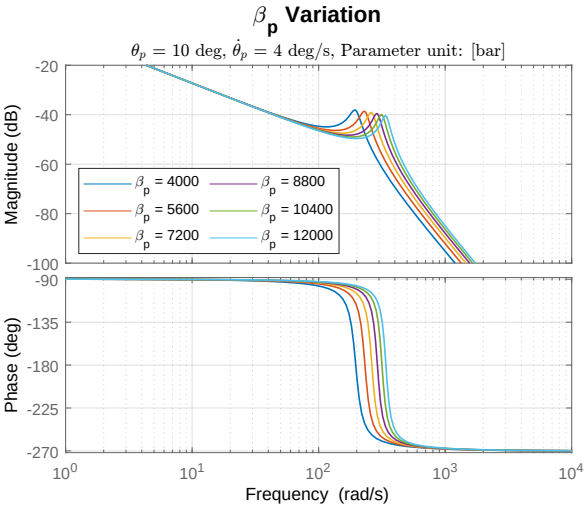

Figure 4.17. Bode plot of varying piston side bulk modulus.

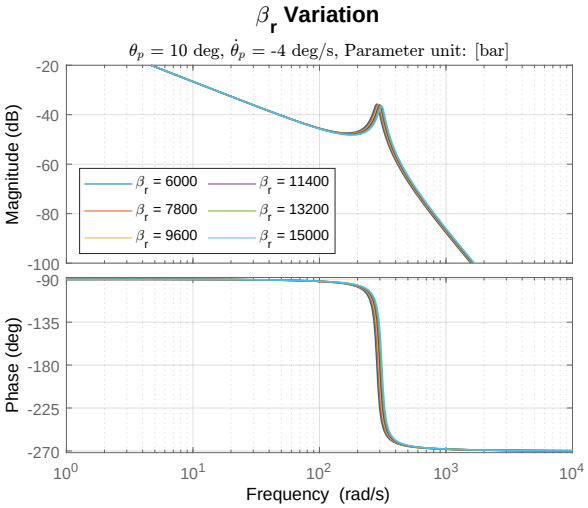

Figure 4.18. Bode plot of varying rod side bulk modulus.

From the analysis performed in this Chapter it can be concluded that, when linearized, the hydraulic pitch system acts as a 3^{rd} order system with;

a low frequency 1^{st} order pole that varies in location by up to 1 decade, based on position, velocity, leakage and oil density.
a high frequency underdamped 2^{nd} order pole varies in location by up to half a decade, based on position and piston side bulk modulus.

Control Design 5

This chapter presents the control design for the pitch angle position controller. Here a control structure is designed based on considerations from Chapter 2 and 4. The performance of the controller is tested in a simulation on both a healthy system and a system where an internal leakage fault is introduced.

5.1 Control Design Considerations

Before designing a position controller for the pitch system, some considerations towards the control problem must be made. The pitch controller should be able to follow a known reference given in Chapter 2 on page 3, while also rejecting the disturbance load torque. The pitch angle reference and load torque disturbance is therefore analyzed by taking the Fast Fourier Transform (FFT), which is seen in Figures 5.1 and 5.2.

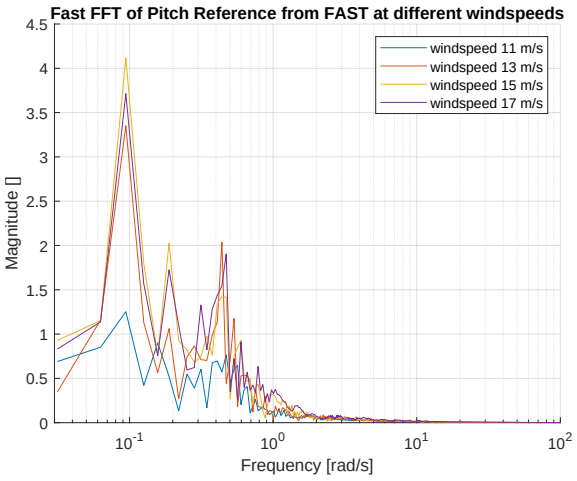

Figure 5.1. Fast Fourier Transform of the pitch angle reference at different wind speeds.

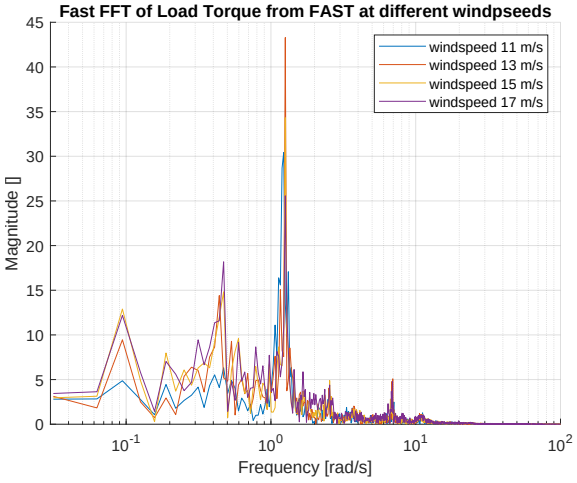

Figure 5.2. Fast Fourier Transform of the load torque acting on the pitch bearing disk at different wind speeds.

The figures show that the frequency content in the pitch angle reference ranges up to 2 rad/s, whereas the load torque frequency content ranges up to 10 rad/s. The highest peak in the load torque FFT is seen at approximately 1.2 rad/s, also the same as approximately 12 RPM, which is the wind turbine rotor speed. Hence, the load torque content at this frequency corresponds to the instants, when the wing of the turbine passes the tower of the wind turbine. This is known as the 1P frequency. As the performance of the controller is mostly evaluated by its tracking abilities, the controller should have good disturbance rejection and good tracking capabilities.

The frequency content of both pitch reference and load torque is negligible above 10 rad/s, therefore the bandwidth of the pitch angle position controller should be approximately 10 rad/s, such that the controller is able to track the reference and reject the load torque disturbance. To further aid the controllers tracking capabilities, a feed forward algorithm is also designed in this chapter, as it has been shown in literature that a feed forward algorithm can provide a better tracking performance [11].
The pitch angle reference also shows that at some times the pitch controller should be able to hold a constant pitch angle, which also demands that the controller has a good steady state performance.

5.2 Control Design

5.2.1 Passive Flow Feed forward

As the pitch reference is known, a passive flow feed forward (FFW) algorithm is added to the control structure. The algorithm is designed according to [7]. As the pitch reference, and hence the velocity reference for the pitch system is known, the Q_p flow reference when leakage flow is neglected is given as:

$$Q_{p_{ref}} = \dot{\theta}_{p_{ref}} \mathcal{J}(\theta_{p_{ref}}) A_p \tag{5.1}$$

Isolating for the opening area in the flow Equation describing Q_p, Equation (3.1) on page 10, and inserting the flow reference for Q_p yields an opening area reference:

$$A_{ref} = \begin{cases} \dfrac{\dot{\theta}_{p_{ref}} \mathcal{J}(\theta_{p_{ref}}) A_p}{C_d \sqrt{\frac{2}{\rho}} \sqrt{p_S - p_{p_{con}}}}, & \dot{\theta}_p > 0 \\ \dfrac{\dot{\theta}_{p_{ref}} \mathcal{J}(\theta_{p_{ref}}) A_p}{C_d \sqrt{\frac{2}{\rho}} \sqrt{p_{p_{con}} - p_T}}, & \dot{\theta}_p < 0 \end{cases} \tag{5.2}$$

Where, $p_S - p_{p_{con}} = \Delta p_{valve}$, and $p_{p_{con}} - p_T = \Delta p_{valve}$, with Δp_{valve} being the pressure drop across the proportional valve and $p_{p_{con}}$ being a constant value chosen to best estimate the piston side chamber pressure. As the velocity reference changes sign the average piston side pressure changes, where it is found that the best estimate of the piston side pressure dependent on flow direction is:

$$p_{p_{con}} = \begin{cases} 112\,\text{bar} & \dot{\theta}_p > 0 \\ 80\,\text{bar} & \dot{\theta}_p < 0 \end{cases} \tag{5.3}$$

When using a passive FFW algorithm, no pressure or position feedback is introduced in the system, which means the system dynamics remain unchanged, hence no system analysis of the introduced control algorithm is needed. To determine the spool position reference from the area reference a seventh order polynomial is fitted to the area characteristic in Subsection 3.1.2 on page 12. The transformation from area reference to spool position reference is given in Equation (5.4):

$$x_v(A_{ref}) = a_7 A_{ref}^7 + a_6 A_{ref}^6 + a_5 A_{ref}^5 + a_4 A_{ref}^4 + a_3 A_{ref}^3 + a_2 A_{ref}^2 + a_1 A_{ref} + a_0 \tag{5.4}$$

Area Polynomial Coefficients				
Coefficient	a_7	a_6	a_5	a_4
Value	$3.849 \cdot 10^{31}$	$-8.765 \cdot 10^{27}$	$8.017 \cdot 10^{23}$	$-3.766 \cdot 10^{19}$
	a_3	a_2	a_1	a_0
	$9.637 \cdot 10^{14}$	$-1.314 \cdot 10^{10}$	$9.786 \cdot 10^{4}$	0.05919

Table 5.1. The polynomial coefficients for the approximated valve area characteristic.

The passive FFW algorithm is tested in the non-linear simulation model, where the spool position reference, $x_{v_{ref}}$, is given from the feed forward control. Furthermore, the load torque disturbance is removed from the non-linear model such that the control algorithm tracking performance is tested without any disturbances to interfere with the tracking performance. Figures 5.3 and 5.4 shows the tracking performance and the spool position reference:

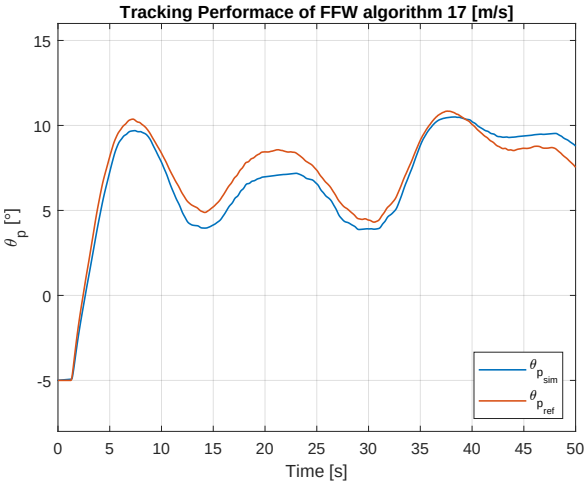

Figure 5.3. Position tracking with only passive FFW algorithm implemented and no disturbance torque introduced to the system.

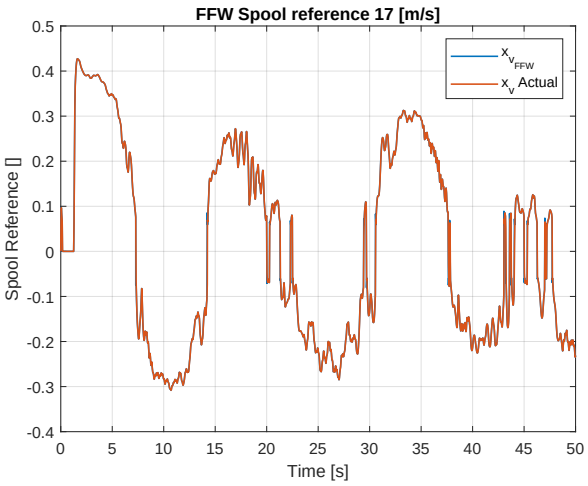

Figure 5.4. Spool position reference from passive FFW algorithm.

In Figure 5.3 it is seen that the FFW control follows the dominant dynamics of the pitch reference, however the position of the bearing disk has a offset relative to the reference, most likely due to neglecting the leakage flow in the flow reference as well as having no pressure feedback. Nevertheless, the FFW algorithm shows good promise in tracking the most dominant dynamics in the pitch reference. The linear controller designed in the following sections only needs to compensate for the drift and the load torque disturbance.

5.2.2 Linear Position Controller

As shown in Figure 5.3, the implemented FFW results in a good tracking of the dynamics of the reference trajectory, however with an offset. To remove this offset a linear position controller is designed. To ease referencing the system dynamics Figure 4.3 on page 22 is shown again in Figure 5.5, here with the valve dynamics added. As mentioned in Section 4.2 on page 22 the open loop system has unstable poles in some linearization points. For the controller design, bode

plots will be used as if there are no unstable poles, and then when a controller is designed the closed loop stability of this controller will be checked using the Nyquist criterion.

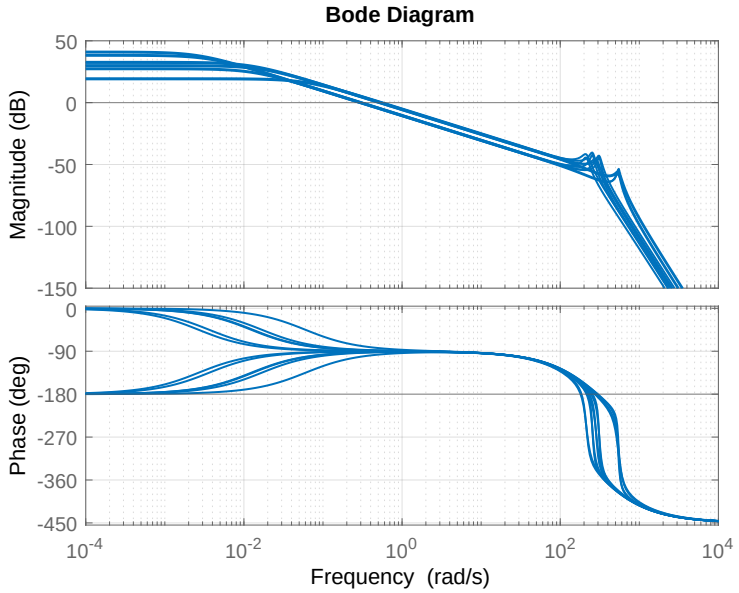

Figure 5.5. System Bode plots for different linearization points, with valve dinamics added.

Since the error in the FFW tracking is small, does not change abruptly and has no ability to handle disturbances, the controller should give a good steady state response with good disturbance rejection. Also, overshoot in the control should have little impact, as the error will be small and smooth, therefore the controller could perhaps be tuned with more focus on response time. As mentioned in Section 4.2 on page 22 the system is of type 0, therefore the linear position controller design takes offset in a PI controller, to increase low frequency gain and remove steady state error. The location of the zero determines the integral action of the PI controller, the higher the frequency, the higher the integral action. It is therefore desired to place this zero at a higher frequency to improve disturbance rejection. However, to avoid losing too much phase from the 1^{st} order pole, the zero is placed around this pole. Here parameter variation should also be taken into account. From the analysis in Chapter 4, increasing leakage will increase the pole frequency, allowing for more integral action. This also means that a higher integral action will help the position controller handle leakage faults. Oil density ρ also affects the placement of the 1^{st} pole. However, in the normal operating range of ρ its effect is small. Based on these considerations the zero is placed at $5 \cdot 10^{-3}$ rad/s. This gives a mostly conservative integral action, but tuned a bit higher then the lowest frequency of the 1^{st} order pole to give a bit better disturbance rejection. Figure 5.6 shows the system response with the PI controller added along with a 30 dB gain to give a bandwidth of around 10 rad/s. Figure 5.7 shows the step response for this controller.

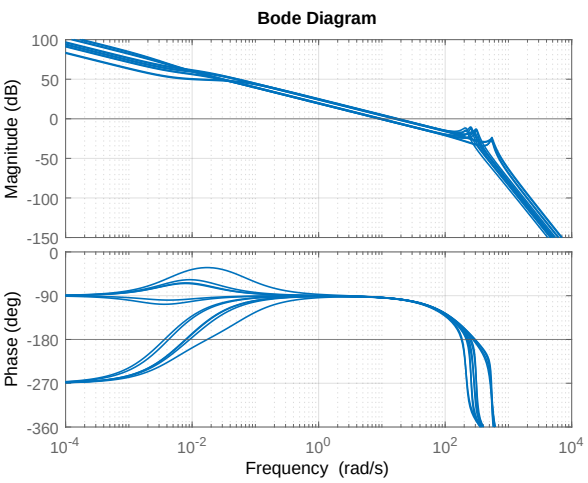

Figure 5.6. Open loop bode plot of system response with added PI control.

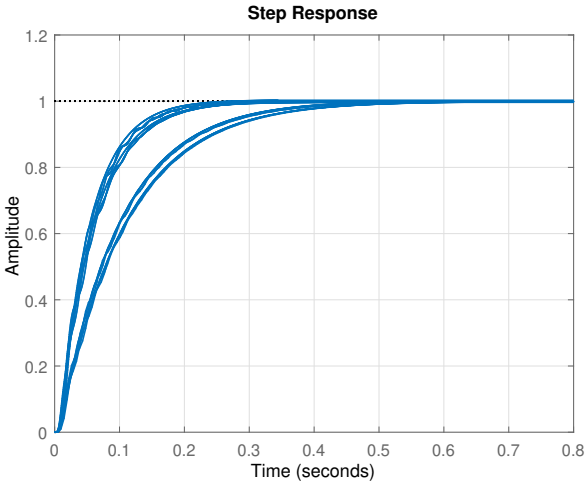

Figure 5.7. Step response of system with added PI control.

As can be seen in Figure 5.7 the output oscillates during the rise of the step response. This seems to be caused by the resonance peaks being gained close to 0 dB. It should also be noted that the system bandwidth with this PI controller is below 10 rad/s for some of the linearization points. To alleviate the output oscillations, and allow for improved bandwidth, a pole is added just before the resonance frequency band, at 75 rad/s. This will reduce the gain of the resonance peaks, increasing the gain margin. It will however also reduce the phase around the 0 dB crossover frequency, which will result in overshoot. This pole is placed at 75 rad/s, to account for variation in $2^n d$ order pole location from variations in piston side bulk modulus, as described in Section 4.2.1 on page 25.

With the pole added, the gain can be increased by an additional 2.5 dB, ensuring a bandwidth over 10 rad/s, with the lowest bandwidth being 14 rad/s. Figure 5.8 and 5.9 shows the open loop and the step response of the PI-pole controller.

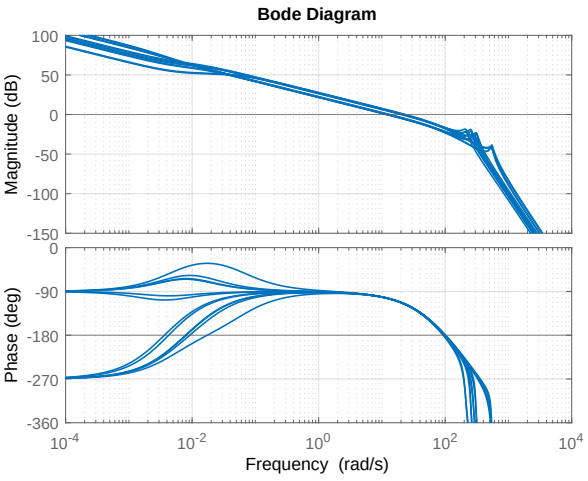

Figure 5.8. Open loop bode plot of system response with the PI-pole controller.

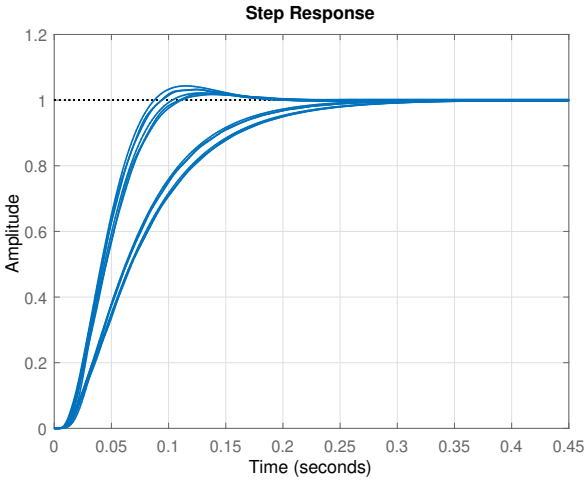

Figure 5.9. Step response of system with the PI-pole controller.

This gives the following controller transfer function:

$$G_c(s) = 3162.7\,\frac{s + 0.005}{s\,(s + 75)} \tag{5.5}$$

The closed loop stability of the system using this controller is checked using the Nyquist criterion, as previously mentioned. The Nyquist criterion is stated as [12]:

$$Z = N + P \tag{5.6}$$

Where Z is the number of closed loop poles in the right hand plane, N is the number of clockwise encirclements of -1 point in Nyquist diagram, and P is the number of open loop poles in the right hand plane. Note that for the system to be stable in closed loop, Z must be zero.

Figure 5.10 shows a logarithmic Nyquist diagram of one of the linearization point with an open loop pole in the right hand plane.

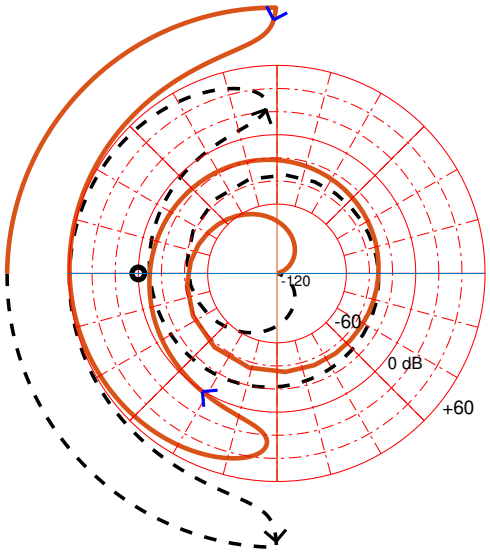

Figure 5.10. Logarithmic Nyquist diagram for the system with the PI-pole controller at one of the linearization points. The small black circle on the real axis represents the -1 point.

From Figure 5.10 it can be seen that the linearization point with an open loop pole in the right hand plan has $N = -1$, therefore the closed loop system is stable. This is found to be the case for all linearization points with right hand plane poles.

5.3 Control Performance

To evaluate the performance of the controller, a series of simulation studies are performed testing the tracking capabilities of the controller at different wind speeds. Section 5.3.1 evaluates the control performance on a healthy pitch system where no faults have happened. The results are then used in the rest of the project as a baseline performance of a pitch system with implemented position control. Section 5.3.2 evaluates the developed pitch control when a leakage fault is introduced to the system.

5.3.1 Healthy System

Figures 5.11 and 5.12 shows the tracking performance of the 17 m/s pitch trajectory. Furthermore, the FFW and position controller output is displayed as well as the valve response to the valve reference.

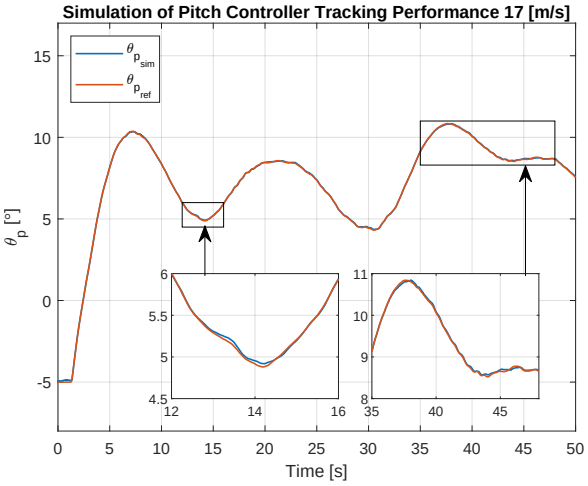

Figure 5.11. Tracking Performance of pitch system with a mean wind speed of 17 m/s.

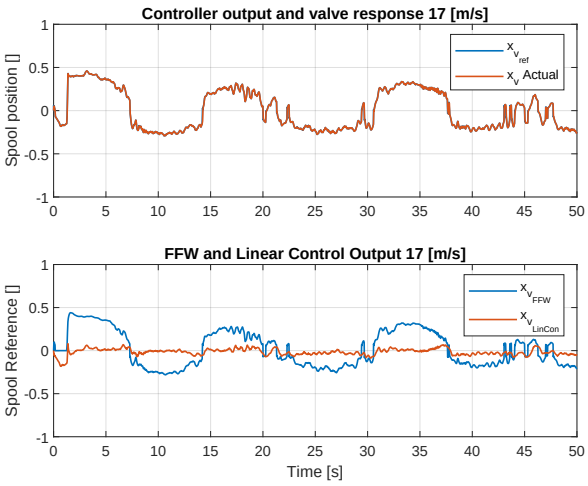

Figure 5.12. The spool position reference given from the controller.

Figure 5.11 shows that the pitch angle follows the trajectory. The control signals in Figure 5.12 behaves as expected, where it seen that the FFW control signal dominates the valve reference and the position controller output only compensates for FFW tracking errors and system disturbances. Furthermore, it is seen that the actual valve spool position tracks the valve spool reference. Hence, the controller is not tuned too aggressively and the control output dynamics are within the bandwidth of the valve response. To further test the performance of the controller it is tested using different trajectories from different mean wind speeds. Figure 5.13 shows the absolute value of the tracking performance error for the different pitch references. It is seen the minimum mean error is 0.017° for the 15 m/s wind speed reference and the maximum mean error is 0.067° for the 11 m/s wind speed reference. However, it is notable that the absolute errors increase significantly when the pitch reference is constant. This is consistent for all wind speed tests, where a varying pitch reference yields a good tracking performance and a constant pitch reference yields a steady state error. To demonstrate this, Figure 5.14 shows the tracking performance of the 11 m/s wind speed reference and the control output divided into the FFW and position controller outputs. Given a constant pitch reference, only the linear position controller outputs a control signal. As the linear position controller is designed assuming a linear area characteristic of the proportional valve it has difficulties compensating for the deadband in the valve of approximately ±10 % command signal. To help the controller better compensate for the nonlinear valve area characteristics, the following section expands the control structure with a deadband compensation.

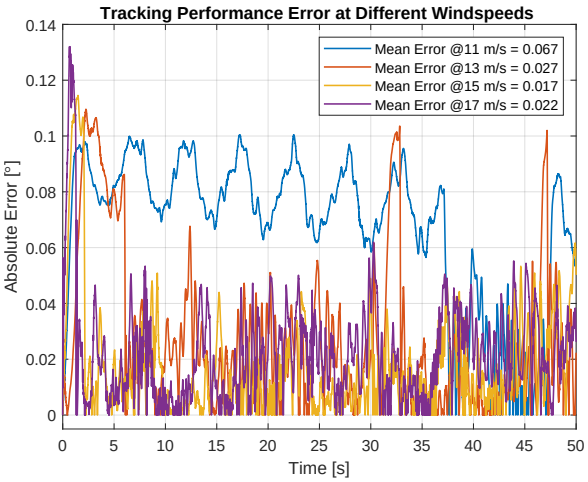

Figure 5.13. Absolute value of the tracking performance error using different mean windspeeds ranging from 11 to 17 m/s.

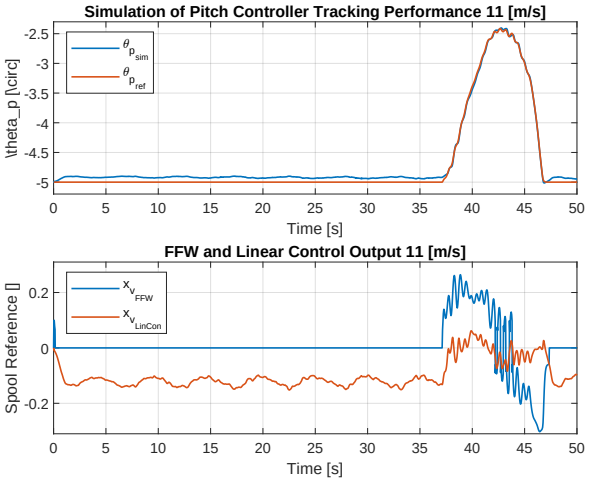

Figure 5.14. An isolated view of the tracking performance and valve reference with a mean wind speed of 11 m/s.

Deadband Compensation

Due to the deadband in the proportional valve, the developed controller was not able to track a constant pitch reference without having steady state error. Therefore, a deadband compensation is designed to compensate for the nonlinear area characteristic of the proportional valve seen in Figure 5.15:

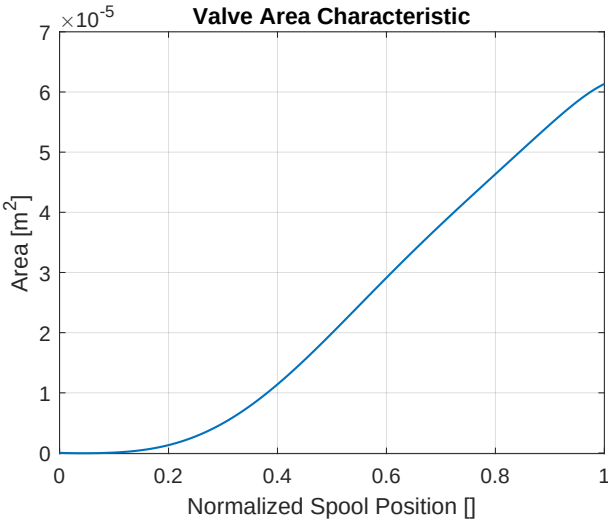

Figure 5.15. Area characteristic of the proportional valve. For spool position references between [-1 0] the figure should be mirrored to the second quadrant.

As seen in Figure 5.15 the proportional valve has a deadband of approximately 10 % command signal. This means a controller output between ±0.1 results in no flow through the valve, hence the linear position controller cannot compensate for small error signals. A deadband compensation is therefore designed, such that the linear position controller and the passive FFW outputs an area reference instead of a normalized spool position. The position control output is

transformed into an area reference by multiplying with the maximum valve opening area, which is seen in Equation (5.7):

$$A_{ref_{lin}} = G_c(s) \cdot E(s) \cdot A_{max} \tag{5.7}$$

Where $E(s)$ is the error signal input to the controller and $G_c(s)$ is the linear controller. This transformation of the control output is seen in Figure 5.16 where the blue line is equal to the linear area reference, $A_{ref_{lin}}$. Furthermore, only applying Equation (5.2) on page 30 in the passive FFW algorithm yields a FFW area reference instead of a spool position. Summation of the passive FFW area reference and the position controller reference yields the area reference that should be transformed into a normalized spool position:

$$A_{ref} = A_{ref_{lin}} + A_{ref_{ffw}} \tag{5.8}$$

Using Equation (5.4) on page 30, which is the relation between valve opening area and spool position, the area reference is transformed into a non linear normalized spool position reference, which is plotted in Figure 5.17. To check that the deadband in the valve is compensated, the non linear spool reference is transformed back to an opening area, which is plotted as the red line in Figure 5.16. It is seen that the area characteristic follows the linear area reference, hence the deadband of the valve is compensated for. Here it should be noted that the ripples in the red line on Figure 5.16 is due to the polynomial approximation of the valve opening area.

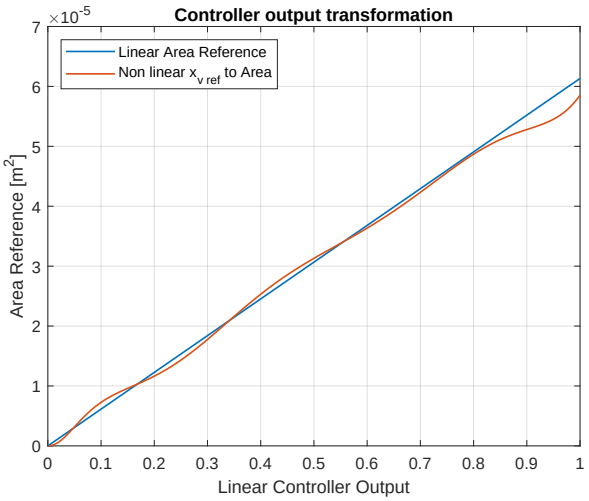

Figure 5.16. The linear position controller output is transformed into a linear area reference seen plotted as the blue line. The red line is the non linear valve spool reference transformed back to an opening area and plotted as a function of the linear controller output.

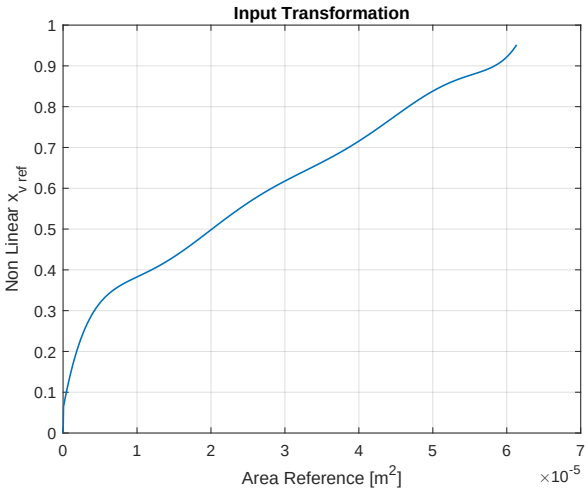

Figure 5.17. The opening area reference in Equation (5.8) is transformed into a non linear valve spool position reference.

Figure 5.18 is a block diagram showing how the deadband compensation is implemented in the control structure:

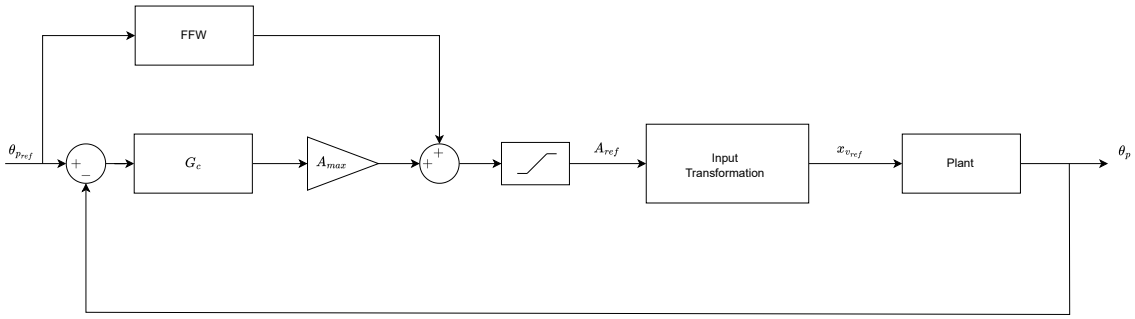

Figure 5.18. Block diagram of Deadband Compensation implemented in the control structure.

The implemented deadband compensation is tested through simulations at different wind speed trajectories seen in Figure 5.19. The maximum mean error is 0.01° and the minimum mean error is 0.007°, hence the controller performs equally well on the different pitch reference trajectories. It is further seen in Figure 5.20 that the steady state performance is significantly increased, as the linear controller is able to compensate for small errors.

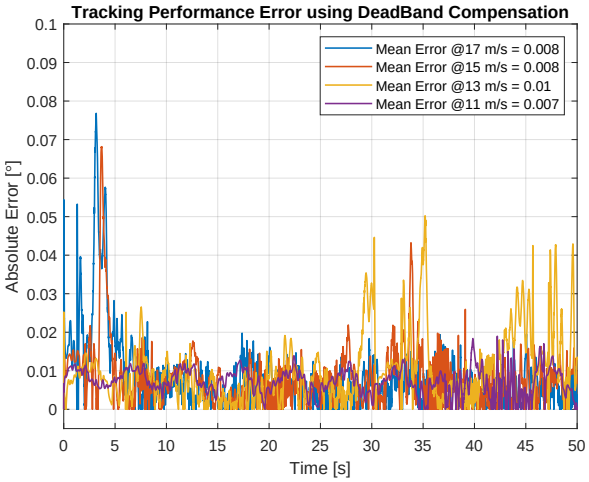

Figure 5.19. Absolute value of the tracking performance error at different wind speeds with deadband compensation implemented.

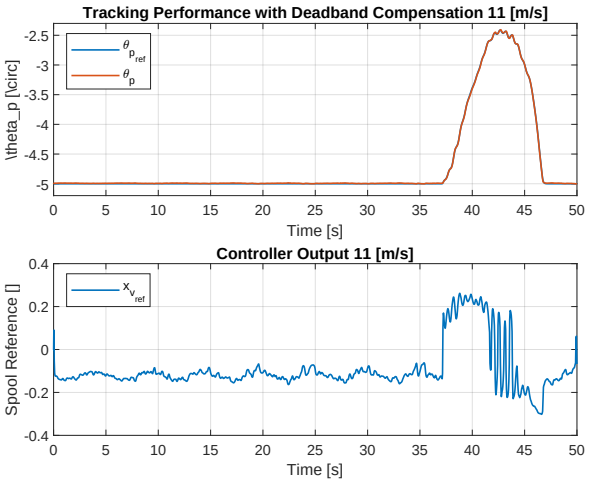

Figure 5.20. Tracking performance and control output of a simulation using 11 m/s mean wind speed.

5.3.2 Faulty System

As described in the system description (Chapter 2 on page 3) the scope of this project is to investigate how a leakage fault impacts a pitch system and how it affects the control performance.

Through different simulation studies it is analyzed how an increase in leakage affects the control performance, by increasing the leakage coefficient, C_{le}, in the system model.

The controller design takes offset in a system where the leakage coefficient is 1 L/min/hbar. Table 5.2 is an overview over the different leakage coefficients used to test how the control performance is impacted by an increase in leakage.

$C_{le}\left[\frac{L/min}{hbar}\right]$	5	10	15	20	25

Table 5.2. Different leakage coefficients used in simulations to simulate an increase in leakage in a pitch system.

Simulating the pitch system model with the different leakage coefficients in Table 5.2 on the 17 m/s mean wind speed trajectory results in an overall worsened tracking performance, which is seen in Figure 5.21. Comparing with the 17 m/s wind speed simulation of the healthy pitch system it is seen that the control performance is impacted for leakage coefficients of 10 L/min/hbar and above.

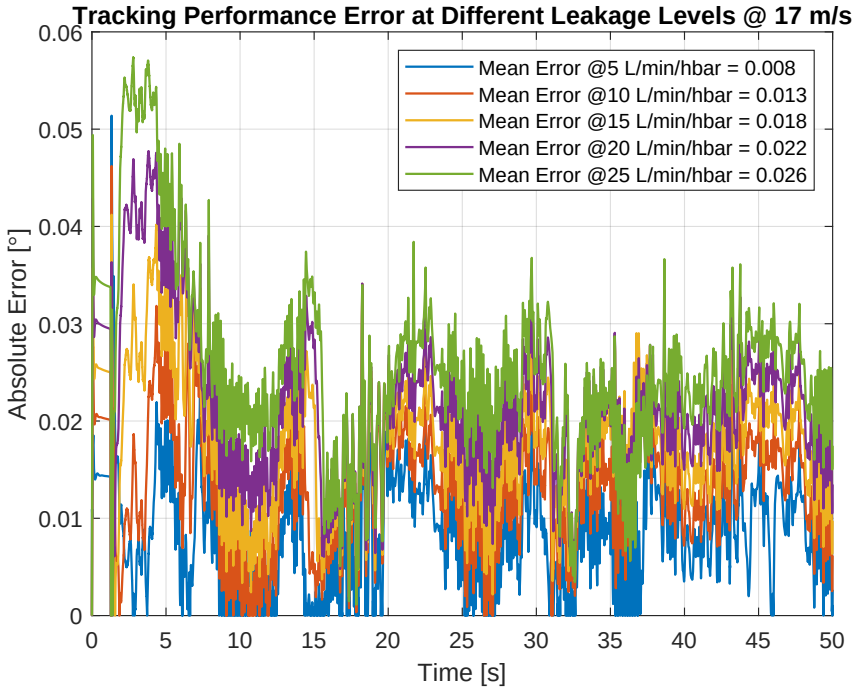

Figure 5.21. Absolute value of the tracking performance error simulated using the 17 m/s mean wind speed trajectory when the systems leakage coefficient is increased to simulate a leakage fault.

It should however be noted that the mean error for the faulty system is still below 0.1 % of the 25° working range defined as −5° to 20°.

5.4 Summary

In this chapter a control structure incorporating a linear controller and a passive flow feed forward term has been designed and tested in simulations. A performance comparison has been made between a healthy system and a system subjected to an internal leakage fault, where the leakage coefficient has been varied between 5 L/min/hbar to 25 L/min/hbar. Here it has been found that for leakages at 10 L/min/hbar and above the performance of the developed controller starts to decrease. Though the decrease in performance is relatively small, this project aims to develop a control algorithm that is robust towards an internal leakage fault, such that performance is maintained.

Problem Statement 6

A hydraulic wind turbine pitch system has been modelled and a control structure has been designed. This control structure has been simulated on both a healthy and a faulty system subject to a leakage fault. It is here shown that controller performance is reduced in case of a leakage fault. This leads to the following problem statement:

Problem Statement

How can the control structure of a wind turbine pitch system be redesigned such that it is fault tolerant towards an internal leakage fault?

Secondary Question

- *How can leakage flow be estimated and implemented into a fault tolerant control structure for a hydraulic wind turbine pitch system?*

Method

In the need for a control design that is fault tolerant towards an internal leakage fault, it is analysed how an internal leakage fault affects a pitch system under normal operating conditions. Furthermore, it is investigated how a Kalman Filter can be used to estimate the internal leakage flow as well as the load torque disturbance introduced by the wind load. The results of the leakage and load estimation capabilities is then used to design a fault tolerant control strategy that can handle an internal leakage fault in the pitch system.

Project Limitations

Due to technical issues with the Hydraulic Pitch System test setup at AAU, it will not be possible to perform any physical test of the pitch system or control structure. Therefore this project will be purely a simulation based study.

Leakage Estimation 7

To make a control system that is actively tolerant towards internal leakage faults, knowledge of the internal leakage is needed. Kalman filters are a well documented approach to estimating states and parameters of dynamic systems. If a Kalman filter can be set up to estimate the internal leakage online, then this estimate can be used directly in the control structure.

Generally a Kalman Filter works by comparing mean and covariance of predicted state and parameter distribution functions with that of measured state and parameter distribution function in the state space, to give an estimate of the true position in the state space. Hydraulic systems actuated by servo valves are known for their non-linear behavior, where especially the orifice equation contributes to non-linearities. Therefore, the standard Kalman will not be a good fit as this algorithm is purely linear as it uses the linear state equation for prediction. The Extended Kalman Filter builds on the Kalman Filter by linearizing the state equations online through the Jacobian of the state eqtuations [13]. However, this is quite computationally demanding if the Jacobian cannot be found analytically, and will only result in first order accuracy [13]. Extended Kalman Filters are also ill suited to handle hard non-linearities like the change in valve characteristic seen in the pitch system.

Another non-linear Kalman Filter exists, called the Unscented Kalman Filter. Instead of linearizing the state equation, the Unscented Kalman Filter captures the mean and covariance of the state distribution with a set of chosen points and then propagating these points through the non-linear state equations [13]. This gives at least second order accuracy and is also easier to implement than the Extended Kalman Filter, as the Jacobian of the state equations is not needed. Based on this, the Unscented Kalman Filter is investigated for leakage estimation on the pitch system.

7.1 The Unscented Kalman Filter

The Unscented Kalman Filter (UKF) differs from the Extended Kalman Filter in the way the mean and covariance of the predicted state distribution function is calculated. Here the UKF uses the so called Unscented Transform.

The Unscented Transform is a way of estimating the statistical properties of a random variable $\mathbf{x}$, with mean $\bar{x}$, covariance $\mathbf{P_x}$ and dimension M, that transforms through the non-linear function $\mathbf{f}(\mathbf{x})$:

$$\mathbf{y} = \mathbf{f}(\mathbf{x}) \tag{7.1}$$

This is done by calculating a spread of $2M+1$ sigma points, $\mathcal{X}$, around the mean of the $\mathbf{x}$ and transforming them through the non-linear function [13].

$$\begin{aligned} \mathcal{X}^{(0)} &= \bar{\mathbf{x}} \\ \mathcal{X}^{(i)} &= \bar{\mathbf{x}} + \Delta\mathbf{x}^{(i)} \ , \ \begin{cases} \Delta\mathbf{x}^{(i)} & = \left(\sqrt{c\mathbf{P}_{\mathbf{x}}}\right)_i \ , \ i = 1, 2, ..., M \\ \Delta\mathbf{x}^{(M+i)} & = -1 \cdot \left(\sqrt{c\mathbf{P}_{\mathbf{x}}}\right)_i \ , \ i = 1, 2, ..., M \end{cases} \end{aligned} \tag{7.2}$$

$$\mathcal{Y}^{(i)} = \mathbf{f}(\mathcal{X}^{(i)}), \quad i = 0, \ldots, 2M \tag{7.3}$$

Where $c = \alpha^2 (M + \kappa)$ is a scaling factor that adjusts the spread of $\mathcal{X}$ based on constant parameters α and κ. The mean and covariance of $\mathbf{y}$ can then be approximated by a weighted sample mean and covariance of the transformed sigma points $\mathcal{Y}$ [13]:

$$\bar{\mathbf{y}} \approx \sum_{i=0}^{2M} \left(W_M^{(i)} \cdot \mathcal{Y}^{(i)} \right) \quad , \begin{cases} W_M^{(0)} & = 1 - \dfrac{M}{\alpha^2 (M + \kappa)} \\ W_M^{(i)} & = \dfrac{1}{2\alpha^2 (M + \kappa)} \ , \ i = 1, 2, ..., 2M \end{cases} \tag{7.4}$$

$$\mathbf{P}_Y \approx \sum_{i=0}^{2M} W_C^{(i)} \left(\mathcal{Y}^{(i)} - \bar{\mathbf{y}} \right) \left(\mathcal{Y}^{(i)} - \bar{\mathbf{y}} \right)^T \quad , \begin{cases} W_C^{(0)} & = \left(2 - \alpha^2 + \beta\right) - \dfrac{M}{\alpha^2 (M + \kappa)} \\ W_C^{(i)} & = \dfrac{1}{2\alpha^2 (M + \kappa)} \ , \ i = 1, 2, ..., 2M \end{cases} \tag{7.5}$$

Where W_M and W_C are weights and β is a constant parameter used to incorporate knowledge about the distribution of $\mathbf{y}$. [13]

7.1.1 UKF Algorithm

The following is algorithm used to implement the UKF. It is based on implementation described by MathWorks in [14].

Notation

To guide the reader through the UKF algorithm, this subsection goes through the notation used.

The notation, $\hat{\mathbf{x}}$, $\hat{\mathbf{y}}$ and $\mathbf{y}$ refers to vectors which respectively are the estimated state vector, the estimated output vector and the measurement vector, which is the measured outputs from the pitch system.

Furthermore, the notation, $\mathbf{P}$, $\mathbf{C}$ and $\mathbf{K}$ refers to matrices, which respectively are the state error covariance matrix, the linear system output matrix and the kalman gain matrix.

The vectors and matrices described with the subscript, $(k|k-1)$ or $(k+1|k)$. The subscript indicates at which time step the calculation is performed and at which time step it estimates the variable. Hence, $\hat{\mathbf{x}}_{k|k-1}$, means the estimated state vector at the current time step is calculated at the previous time step.

Additionally, the superscript, (i), is also used, which means the variable is a matrix, where the superscript indicates which column is used for the calculation.

Initialization

Initialize the state vector:

$$\hat{\mathbf{x}}_0 = E\left(\mathbf{x}_0\right) = E\left(\left[\theta_p \ \dot{\theta}_p \ p_p \ p_r\right]^T\right) \tag{7.6}$$

Where E denotes the expected value of the state, which in this case is the initial value of the state.

Initialize the state estimation error covariance matrix:

$$\mathbf{P}_0 = \mathbf{P}_0 = E\left(\left(\mathbf{x}_0 - \hat{\mathbf{x}}_0\right)\left(\mathbf{x}_0 - \hat{\mathbf{x}}_0\right)^T\right) \tag{7.7}$$

Here assuming that all states are known at initialization. If this is not the case a best guess is used.

Prediction Step

Determine the sigma points $\hat{\mathbf{x}}_{k|k-1}^{(i)}$ at time step k where $\hat{\mathbf{x}}_{k|k-1}^{(i)}$ is a matrix which has as many rows as states and $(2M+1)$ columns, where M is the number of states.

$$\begin{aligned}
\hat{\mathbf{x}}_{k|k-1}^{(0)} =& \hat{\mathbf{x}}_{k|k-1} \\
\hat{\mathbf{x}}_{k|k-1}^{(i)} =& \hat{\mathbf{x}}_{k|k-1} + \Delta\mathbf{x}^{(i)} \ , \ \begin{cases} \Delta\mathbf{x}^{(i)} & = \left(\sqrt{c\mathbf{P}_{k|k-1}}\right)_i \ , \ i = 1,2,...,M \\ \Delta\mathbf{x}^{(M+i)} & = -1 \cdot \left(\sqrt{c\mathbf{P}_{k|k-1}}\right)_i \ , \ i = 1,2,...,M \end{cases}
\end{aligned} \tag{7.8}$$

Where $c = \alpha^2\left(M + \kappa\right)$, with α and κ being tuning parameters. Each column of the sigma point matrix, $\hat{\mathbf{x}}_{k|k-1}^{(i)}$, is a vector describing a point in the state space of the system.

The next step is to use the system output matrix, $\mathbf{C}$, to determine the predicted measurements from each of the sigma points:

$$\hat{\mathbf{y}}_{k|k-1}^{(i)} = \mathbf{C} \cdot \hat{\mathbf{x}}_{k|k-1}^{(i)} \ , \ i = 0,1,2,...,M \tag{7.9}$$

The predicted measurements from the sigma points are combined to predict the measurement at time step k:

$$\hat{\mathbf{y}}_k = \sum_{i=0}^{2M}\left(W_M^{(i)} \cdot \hat{\mathbf{y}}_{k|k-1}^{(i)}\right) \ , \ \begin{cases} W_M^{(0)} & = 1 - \dfrac{M}{\alpha^2\left(M+\kappa\right)} \\ W_M^{(i)} & = \dfrac{1}{2\alpha^2\left(M+\kappa\right)} \ , \ i = 1,2,...,2M \end{cases} \tag{7.10}$$

The next step is to estimate the covariance of the weighted predicted measurement (Equation (7.10)) and the predicted measurements from the sigma points (Equation (7.9)). The matrix R_k is added after the sum to account for measurement noise:

$$\mathbf{P}_Y = \sum_{i=0}^{2M} W_C^{(i)} \left(\hat{\mathbf{y}}_{k|k-1}^{(i)} - \hat{\mathbf{y}}_k\right)\left(\hat{\mathbf{y}}_{k|k-1}^{(i)} - \hat{\mathbf{y}}_k\right)^T + R_k \ , \ \begin{cases} W_C^{(0)} & = \left(2 - \alpha^2 + \beta\right) - \dfrac{M}{\alpha^2\left(M+\kappa\right)} \\ W_C^{(i)} & = \dfrac{1}{2\alpha^2\left(M+\kappa\right)} \ , \ i = 1, 2, ..., 2M \end{cases} \tag{7.11}$$

Hereafter, the cross covariance is estimated.

$$\mathbf{P}_{XY} = \frac{1}{2\alpha^2\left(M+\kappa\right)} \cdot \sum_{i=1}^{2M} \left(\hat{\mathbf{x}}_{k|k-1}^{(i)} - \hat{\mathbf{x}}_{k|k-1}\right)\left(\hat{\mathbf{y}}_{k|k-1}^{(i)} - \hat{\mathbf{y}}_k\right)^T \tag{7.12}$$

The last step of the prediction is to determine the Kalman gain, state estimates and the state estimation error covariance matrix:

$$\mathbf{K} = \mathbf{P}_{XY} \cdot \mathbf{P}_Y^{-1} \tag{7.13}$$

$$\hat{\mathbf{x}}_{k|k} = \hat{\mathbf{x}}_{k|k-1} + K\left(\mathbf{y}_k - \hat{\mathbf{y}}_k\right) \tag{7.14}$$

$$\mathbf{P}_{k|k} = \mathbf{P}_{k|k-1} - \mathbf{K} \cdot \mathbf{P}_Y \cdot \mathbf{K}^T \tag{7.15}$$

Where $\mathbf{K}$ is the Kalman gain.

Correction step

The purpose of the correction step is to estimate the state vector at the next time step as well as updating the state estimate error covariance matrix at the next time step.

The first step of the correction is to determine new sigma points using the state estimation and state estimation error covariance matrix from the current time step:

$$\begin{aligned} \hat{\mathbf{x}}_{k|k}^{(0)} &= \hat{\mathbf{x}}_{k|k} \\ \hat{\mathbf{x}}_{k|k}^{(i)} &= \hat{\mathbf{x}}_{k|k} + \Delta\mathbf{x}^{(i)} \ , \ \begin{cases} \Delta\mathbf{x}^{(i)} & = \left(\sqrt{c\mathbf{P}_{k|k}}\right)_i \ , \ i = 1, 2, ..., M \\ \Delta\mathbf{x}^{(M+i)} & = -1 \cdot \left(\sqrt{c\mathbf{P}_{k|k}}\right)_i \ , \ i = 1, 2, ..., M \end{cases} \end{aligned} \tag{7.16}$$

For each of the determined sigma points, the non-linear model is used to predict the state vector. Here the Forward Euler method is used:

$$\hat{\mathbf{x}}_{k+1|k}^{(i)} = \mathbf{F}\left(\hat{\mathbf{x}}_{k|k}^{(i)}, u_k\right) \tag{7.17}$$

Where u_k is the input to the system at the current time step, and $\mathbf{F}$ is the non-linear state transition function used to predict the state vector for each of the sigma points at the next time step.

$$\mathbf{F}\left(\hat{\mathbf{x}}_{k|k}^{(i)}, u_k\right) = \mathbf{f}\left(\hat{\mathbf{x}}_{k|k}^{(i)}, u_k\right) \cdot T_s + \hat{\mathbf{x}}_{k|k}^{(i)} \tag{7.18}$$

A weighted average is found to predict the state vector at the next time step from the sigma points:

$$\hat{\mathbf{x}}_{k+1|k} = \sum_{i=0}^{2M} W_M^{(i)} \hat{\mathbf{x}}_{k+1|k}^{(i)} \ , \quad \begin{cases} W_M^{(0)} & = 1 - \dfrac{M}{\alpha^2 (M+\kappa)} \\ W_M^{(i)} & = \dfrac{1}{2\alpha^2 (M+\kappa)} \ , \ i = 1, 2, ..., 2M \end{cases} \tag{7.19}$$

The state estimation error covariance at the next time step is determined from $\hat{\mathbf{x}}_{k+1|k}$ and $\hat{\mathbf{x}}_{k+1|k}^{(i)}$. Here Q_k is added to account for additive process noise:

$$\mathbf{P}_{k+1|k} = \sum_{i=0}^{2M} W_C^{(i)} \left(\hat{\mathbf{x}}_{k+1|k}^{(i)} - \hat{\mathbf{x}}_{k+1|k}\right) \left(\hat{\mathbf{x}}_{k+1|k}^{(i)} - \hat{\mathbf{x}}_{k+1|k}\right)^T + Q_k \ ,$$
$$\begin{cases} W_C^{(0)} & = \left(2 - \alpha^2 + \beta\right) - \dfrac{M}{\alpha^2 (M+\kappa)} \\ W_C^{(i)} & = \dfrac{1}{2\alpha^2 (M+\kappa)} \ , \ i = 1, 2, ..., 2M \end{cases} \tag{7.20}$$

7.1.2 Parameter Estimation

To estimate a parameter it has to be included in the non-linear state transition function, however there typically is not a model for the dynamics of the parameter in question, therefore an estimate of the dynamics of the parameter will have to be made. This is typically done by simply assuming that the parameter is slowly varying, meaning that the rate of change of the parameter is zero. This is shown in Equation (7.21) for the case where the leakage coefficient is estimated [15]:

$$\begin{bmatrix} \dot{\hat{\mathbf{x}}} \\ \dot{\hat{C}}_{le} \end{bmatrix} = \begin{bmatrix} \mathbf{f}\left(\hat{\mathbf{x}}, u\right) \\ 0 \end{bmatrix}, \qquad \begin{bmatrix} \hat{\mathbf{x}}_{k+1|k} \\ \hat{C}_{le_{k+1|k}} \end{bmatrix} = \begin{bmatrix} \mathbf{f}\left(\hat{\mathbf{x}}_{k|k}, u_k\right) \\ 0 \end{bmatrix} \cdot T_s + \begin{bmatrix} \hat{\mathbf{x}}_{k|k} \\ \hat{C}_{le_{k|k}} \end{bmatrix} \tag{7.21}$$

The result of this is that the parameter estimate is only changed through the Kalman gain.

7.1.3 Scaling

Since sigma points are spread in state space then if there is a large difference in scaling between the states, e.g. pressure in the range of $210 \cdot 10^5\,\mathrm{Pa}$ and a leakage coefficient in the range of $2 \cdot 10^{-12}\,\mathrm{m^3/s/Pa}$ (since the model is made using SI units), the Unscented Transform can become inaccurate. Therefore, the states and parameters in the UKF are scaled. Pressures are scaled by a factor of $2 \cdot 10^{-7}$ and the leakage coefficient is scaled by a factor of $1 \cdot 10^{12}$. Pitch position and velocity are not scaled, as their nominal values are within a range that does not need scaling for the UKF to handle.

7.1.4 Tuning

An Unscented Kalman Filter is tuned through three tunable parameters (α, β and κ), and a system specific process noise (Q_k) and measurement noise (R_k) covariance matrices.
The α parameter adjusts the spread of the sigma points and is usually chosen between 1 and 0. The β parameter adjusts the assumed distribution. If the distribution is Gaussian $\beta = 2$ is optimal. κ is an additional parameter to adjust sigma point spread. [13]
In [14] it is described that the kappa value is normally set to zero. This project also found that only using the alpha parameter to adjust the spread of sigma points gave good results, and the kappa parameter is therefore not investigated further.
The process noise covariance matrix Q_k describes how much the model from the state transition function is trusted, how much inaccuracy there is in the model and how much external disturbance there is. If a value in Q_k is decreased then the Kalman filter will rely more on the model and less on measurements for the given state, and vice versa. The measurement noise covariance matrix R_k describes how much noise there is in the measured signals. In this project Q_k and R_k are assumed to be diagonal matrices, meaning that process and measurement noise is not correlated between states.
Tuning is mainly achieved through adjusting Q_k. It is initially tuned based on analysis of system sensitivity to noise and the amplitude of the load, however it is found that this did not result in stable estimation. Instead a trial and error approach is used.

7.2 Leakage Estimation Results

To evaluate the viability of leakage estimation on the pitch system using an Unscented Kalman Filter, the filter will be tested in simulation with all available information, including full state feedback. Testing will then progressively be moved closer to real conditions. Tests are conducted by subjecting the pitch simulation model to a gradually increasing leakage. The leakage coefficient is increased from 1 to 50 L/min/hbar. Unless otherwise specified all tests are conducted at 17 m/s wind speed, with a default sampling frequency of 100 kHz which is the same as the simulation frequency, and a constant supply pressure. Throughout this section the terms ‘no load’ and ‘unknown load’ are used, which respectively means that a test have been simulated without or with the load torque connected in the simulation model. The following tests are conducted:

- Leakage estimation with full state feedback and no load
- Leakage estimation with full state feedback and an unknown load
- Leakage estimation with velocity estimation using joint state and parameter estimation and unknown load
- Leakage estimation with velocity estimation using dual state and parameter estimation and unknown load
- Leakage estimation with velocity estimation using Super Twisting Sliding Mode (STSM) observation and unknown load
- Load estimation using UKF

- Leakage estimation with added load estimation
- Leakage estimation with added noise
- Leakage estimation with a sampling frequency of 1 kHz

For the first estimation test initial tunings for the UKF parameters are made. Through this tuning it is found that at β value of 1.2 gives a good result. This suggests that the state covariance distribution of the pitch system is not Gaussian. The rest of the UKF parameters are tuned as follows:

$$\alpha = 1e\text{-}4, \qquad \beta = 1.2$$

$$Q_k = \begin{bmatrix} 1e\text{-}8 & 0 & 0 & 0 & 0 \\ 0 & 1e\text{-}8 & 0 & 0 & 0 \\ 0 & 0 & 1e\text{-}6 & 0 & 0 \\ 0 & 0 & 0 & 1e\text{-}5 & 0 \\ 0 & 0 & 0 & 0 & 1e\text{-}1 \end{bmatrix}, \qquad R_k = \begin{bmatrix} 0.1 & 0 & 0 & 0 \\ 0 & 0.1 & 0 & 0 \\ 0 & 0 & 0.1 & 0 \\ 0 & 0 & 0 & 0.1 \end{bmatrix} \tag{7.22}$$

The simulation results are shown in Figure 7.1. As for the rest of this Section the tuning parameters can be found in Appendix C.

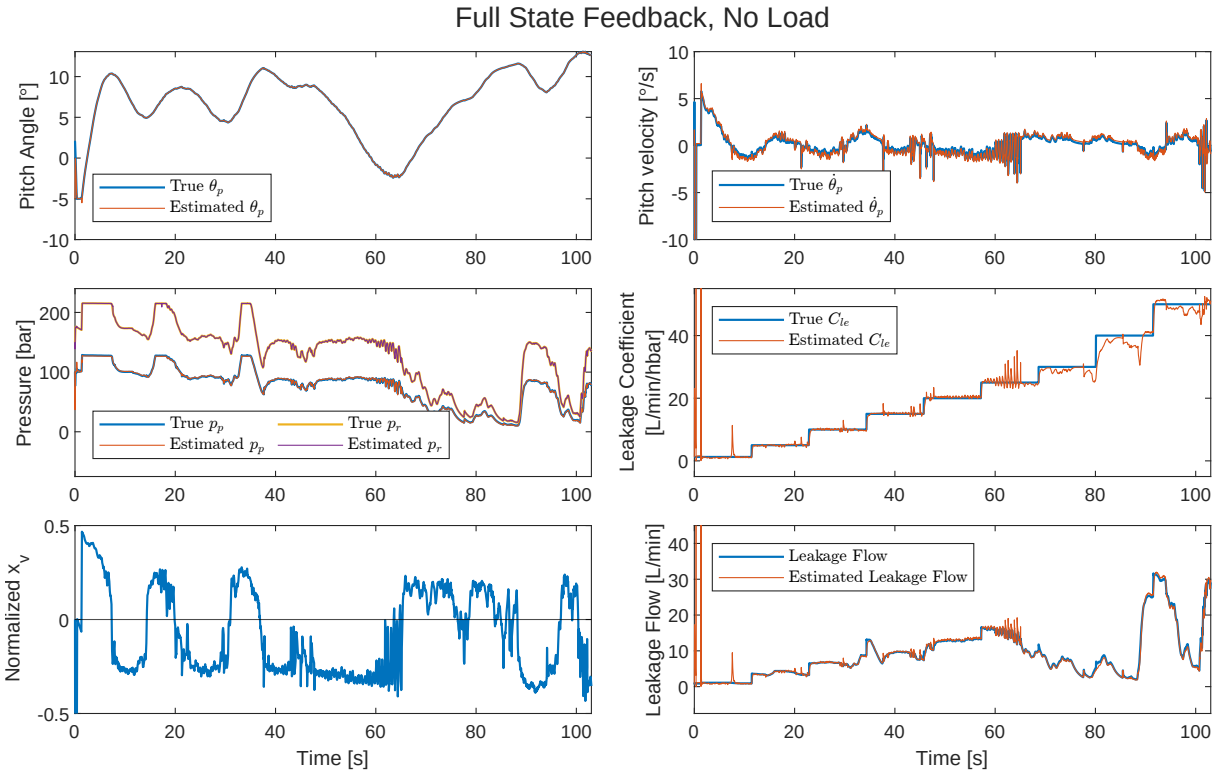

Figure 7.1. Results of leakages estimation with full state feedback and no load torque. The figure shows the true value of the states and leakage coefficient, as well as their estimated values from the Kalman Filter. Valve position and leakage flow is also shown.

This result shows that Leakage flow can be estimated quite accurately using a UKF. Looking at the leakage flow estimate and the leakage coefficient estimate it can be seen that the leakage

flow estimate is accurate, with the exception of a few spikes, throughout the whole simulation, while the leakage coefficient becomes less accurate at the end of the simulation. This decrease in accuracy could be caused by the lower pressures at the end of the simulation. This is emphasized in Figure 7.2, where it can be seen that when the load pressure drops below approximately 40 bar the leakage estimation has more oscillations, however it is still accurate at estimating the leakage. The load pressure, p_L, is in this Section defined as $p_L = p_r - p_p$.

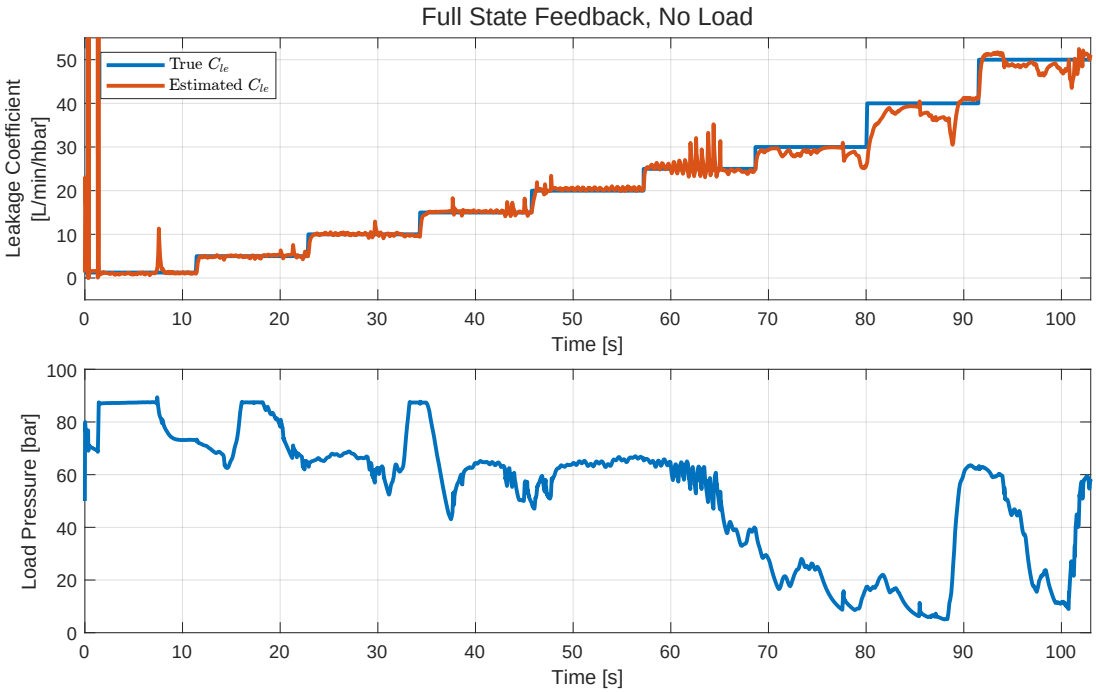

Figure 7.2. Comparison of leakage estimation and load pressure with full state feedback and no load torque.

If the UKF is primarily estimating the leakage flow and then calculating the coefficient based on the pressures, then a lower load pressure might make it more difficult to accurately estimate the coefficient. It is found that the previously mentioned spikes in leakage estimate cannot be tuned away without losing estimation performance. Therefore a rate limiter of 3 L/min/hbar/s is instead added to the leakage coefficient estimation output, since the leakage coefficient can be assumed to be slow varying. The reason a rate limiter is used, and not a filter, is the magnitude of the spikes. When subjected to a large spikes, the output of the filter would still move far of the actual value of C_{le} quite quickly. This is shown in Figure 7.3.

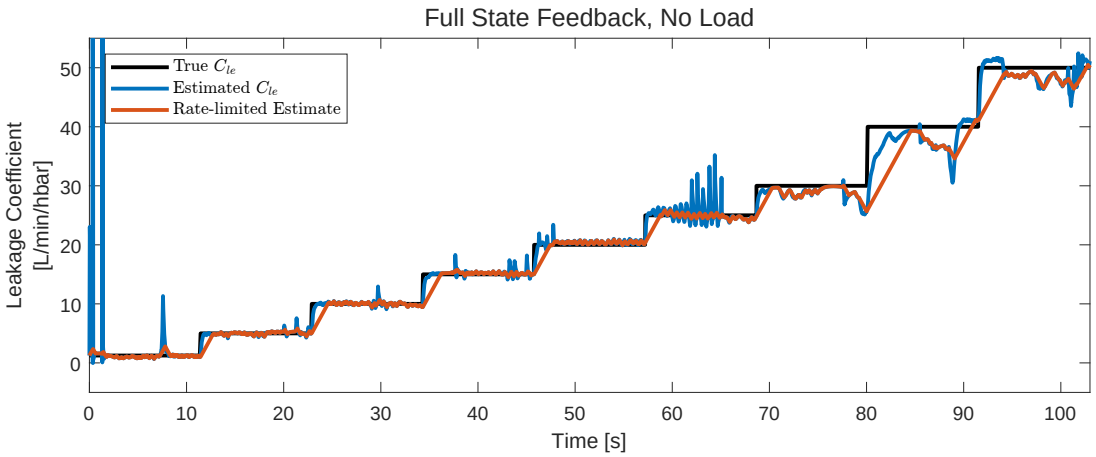

Figure 7.3. Results of rate limiting the leakage estimate. The graph shows the true leakage coefficient, the leakage coefficient estimate and the rate limited leakage coefficient estimate.

Here it can be seen that with the rate limit the spikes are suppressed while the estimate is still accurate.

7.2.1 Unknown Load

The UKF leakage estimator is now tested with the load torque from the wind connected to the simulation model. In the UKF state transition functions τ_{load} is still assumed to be zero. After a retuning of the process noise matrix using trial and error the results shown in Figure 7.4 are achieved.

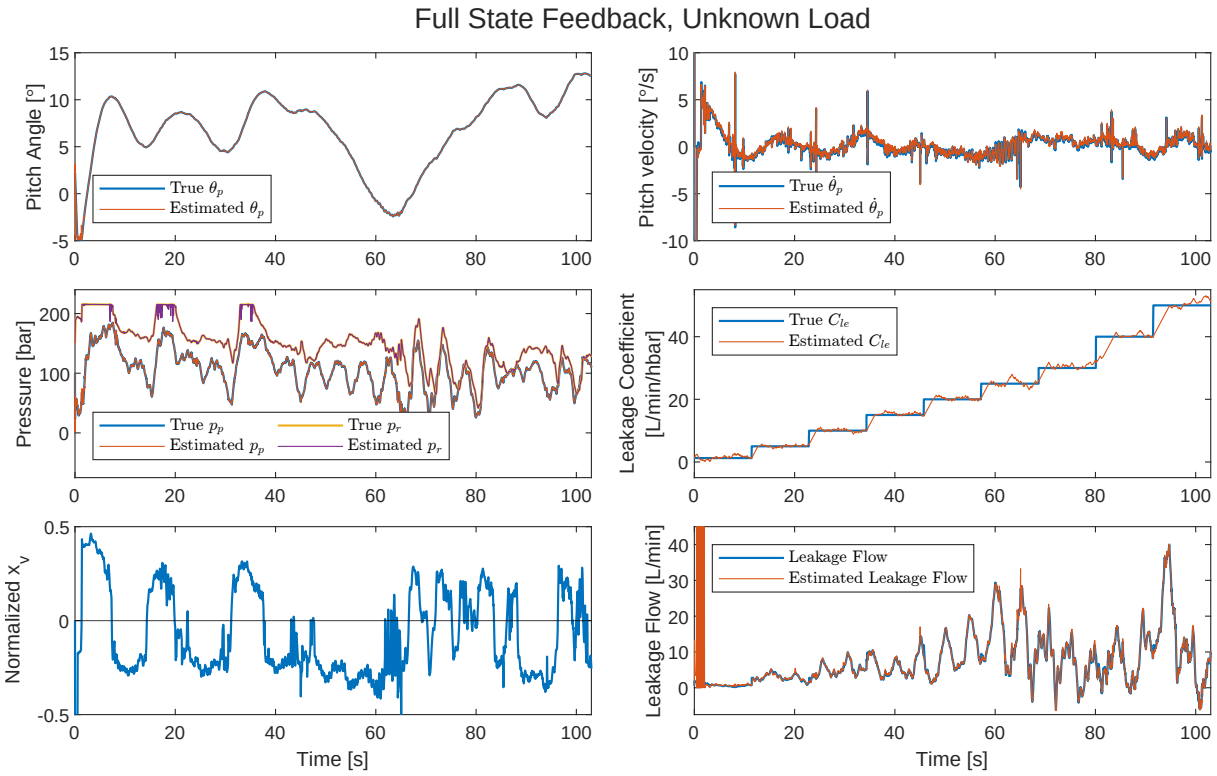

Figure 7.4. Results of leakages estimation with full state feedback and the load torque from the wind connected. The figure shows the true value of the states and leakage coefficient, as well as their estimated values from the Kalman Filter. Valve position and leakage flow is also shown.

Here it can be seen that the leakage coefficient can be estimated with an unknown load.

When comparing the results in Figure 7.3 and 7.4 it can be seen that the accuracy of the leakage flow estimate seems the be the same for the two tests. However, looking at the coefficient estimate it is more stable in the no load simulation, with the exception of the higher values, where the load simulation seems to be better. Figure 7.5 shows the leakage coefficient estimate in relation to the load pressure.

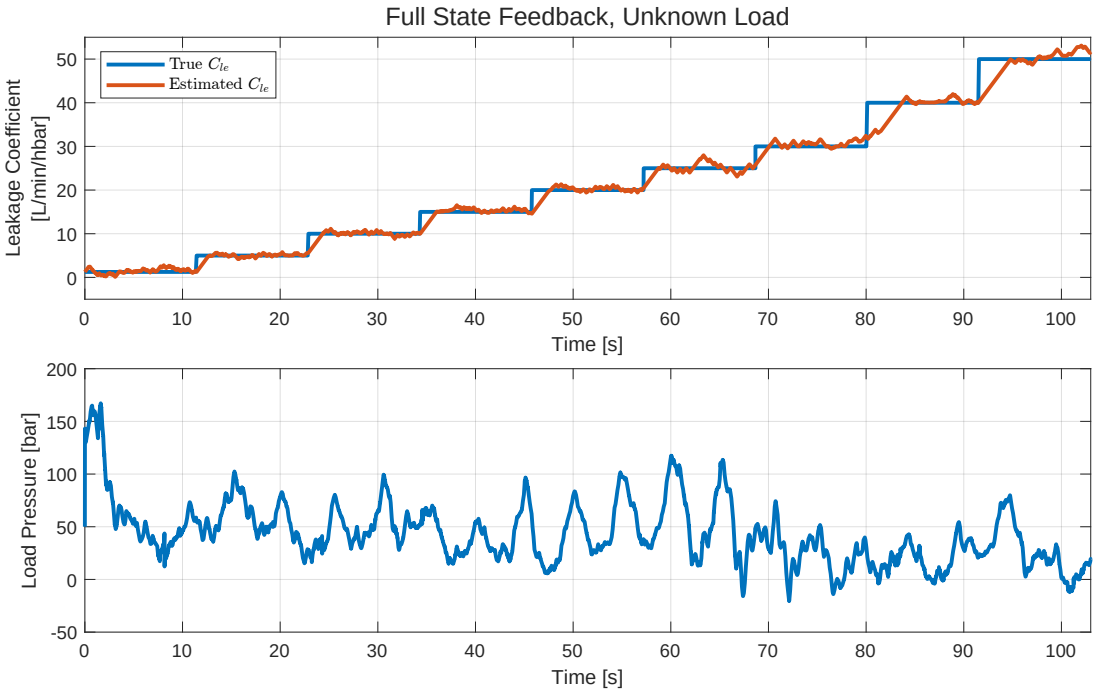

Figure 7.5. Comparison of leakage estimation and load pressure with full state feedback and the load torque from the wind connected.

Here it can be seen that the load pressure becomes very erratic when the wind load is added. A hypothesis is that the dips and spikes in the load pressure is what is causing the unknown load leakage estimate to become more erratic, but also what is causing the unknown load leakage estimate to be more accurate at the end of the simulation, as the load pressure spikes higher here. Based on this it seems that the leakage coefficient estimate accuracy is load dependent.

7.2.2 Pitch Velocity Estimation

With the UKF leakage coefficient estimator shown to work with full state feedback, tests are now conducted without velocity feedback, as would be the case for the pitch system.

This approach is known as joint estimation [13], where the UKF is set up to estimate both the velocity and the leakage coefficient of the pitch system. However, it was not possible to find a tuning for this approach, as the UKF became unstable. Therefore, a different approach is tested. As shown in the previous section, the UKF estimation was accurate using full state feedback. Hence, the idea is to design a velocity estimator that can accurately estimate the velocity which can then be used as a feedback to the leakage estimating UKF. This approach is called dual estimation [13] and is shown in Figure 7.6.

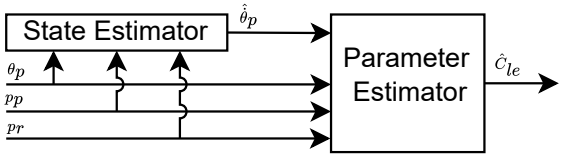

Figure 7.6. Dual estimation approach, where a state estimator is used to estimate the velocity to use as feedback to the UKF.

First a second UKF is used as the state estimator. This resulted in a good estimate of the dynamics of the velocity, however, with an offset between the estimate and the true velocity as is shown in the right graph of Figure 7.7. Though the velocity estimate is seen to be accurate in dynamics, the leakage estimation does not converge, which is shown in the left graph of Figure 7.7.

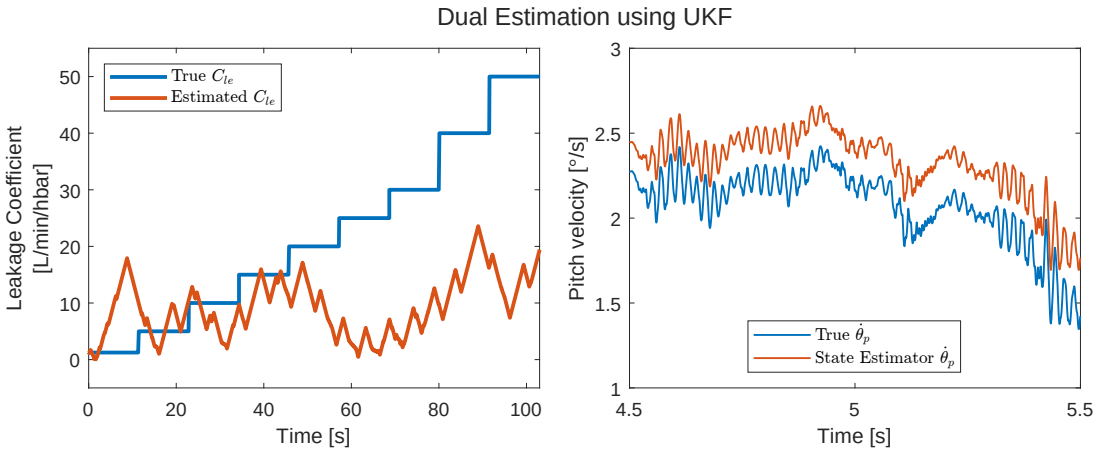

Figure 7.7. Results of dual estimation using two UKF's. The left graph shows the leakage estimate from the parameter estimating UKF compared to the true leakage. The right figure shows the velocity estimate from the state estimating UKF compared to the true velocity.

As the velocity estimation is accurate in its estimation of the velocity dynamics, it is concluded that the reason the leakage estimate did not converge, is due to the offset in the UKF velocity estimation. Therefore, a Super Twisting Sliding Mode (STSM) observer is tested for velocity estimation, as an STSM observer acts as a differentiator instead of estimation based on models and statistic properties. The idea is that this will eliminate the offset in the velocity estimate. The STSM observer is implemented based on [16]. The equations and parameters used are described in Appendix B. The simulation results when using the STSM velocity estimate as feedback to the Kalman Filter to obtain full state feedback is seen in Figure 7.8:

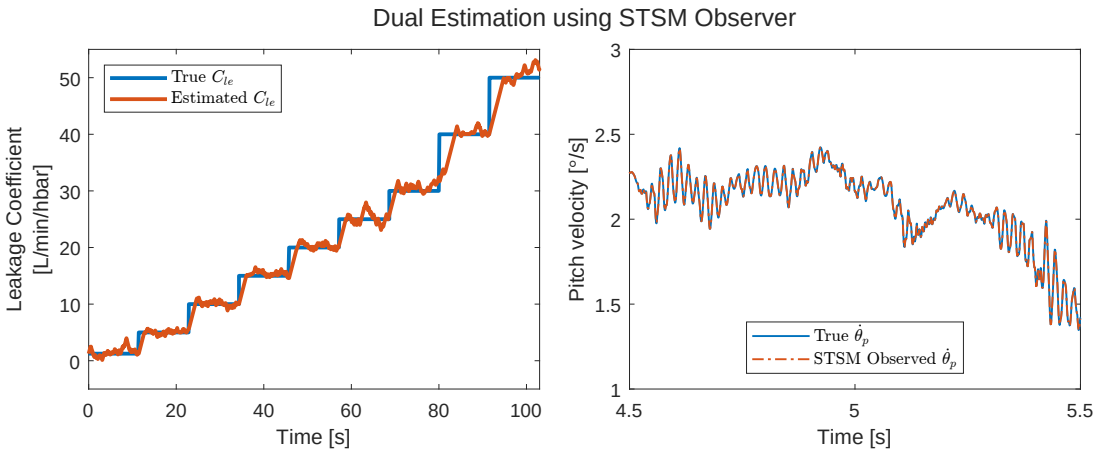

Figure 7.8. Results of dual estimation using a STSM observer to estimate pitch velocity. The left graph shows the leakage estimate from the parameter estimating UKF compared to the true leakage. The right figure shows the velocity estimate from the STSM observer compared to the true velocity.

Here it can be seen that when using an STSM to estimate the pitch velocity, the offset in the estimate is removed, and the leakage estimate now converges. This supports the conclusion that the offset in the velocity estimate was the reason the leakage estimate did not converge. As the STSM works as a differentiator it will however be quite sensitive to noise. This will be discussed later.

7.2.3 Load Estimation

In Section 7.2.1 it is shown that the load pressure and thereby the load torque affects the leakage estimation. A hypothesis is that the leakage estimate can be improved if the load torque is known. Based on this an additional UKF is set up to estimate the wind load. Here a model for the dynamics of the wind load is needed. In Chapter 5 it is shown that the dominant frequency of the wind load is at 1.2 rad/s, which corresponds to the wind turbine rotor speed. Furthermore, it is shown in the system description that the average load torque amplitude can be approximated at around 65 kNm. Therefore, the dynamics of the load torque is approximated as a sine wave with an amplitude of 65 kNm and a frequency of 1.2 rad/s. The expansion of the state transition function is shown in Equation (7.23).

$$\begin{bmatrix} \dot{\hat{\mathbf{x}}} \\ \dot{\hat{\tau}}_{load} \end{bmatrix} = \begin{bmatrix} \mathbf{f}\left(\hat{\mathbf{x}}, u\right) \\ 65\,\text{kNm} \cdot \cos\left(1.2\frac{\text{rad}}{\text{s}} \cdot t\right) \end{bmatrix} \tag{7.23}$$

Where t is the simulation time. τ_{load} is also scaled in the UKF, by a factor of $120 \cdot 10^{-3}$, similarly to the pressures and the leakage coefficient as described in Section 7.1.3. The UKF estimating the load torque is also tuned by an trial and error approach.
Figure 7.9 shows load estimation results with full state feedback, where the velocity is estimated by the STSM algorithm. Load estimation is also tested without velocity feedback, this is found to give very similar results. This result is shown in Appendix F.

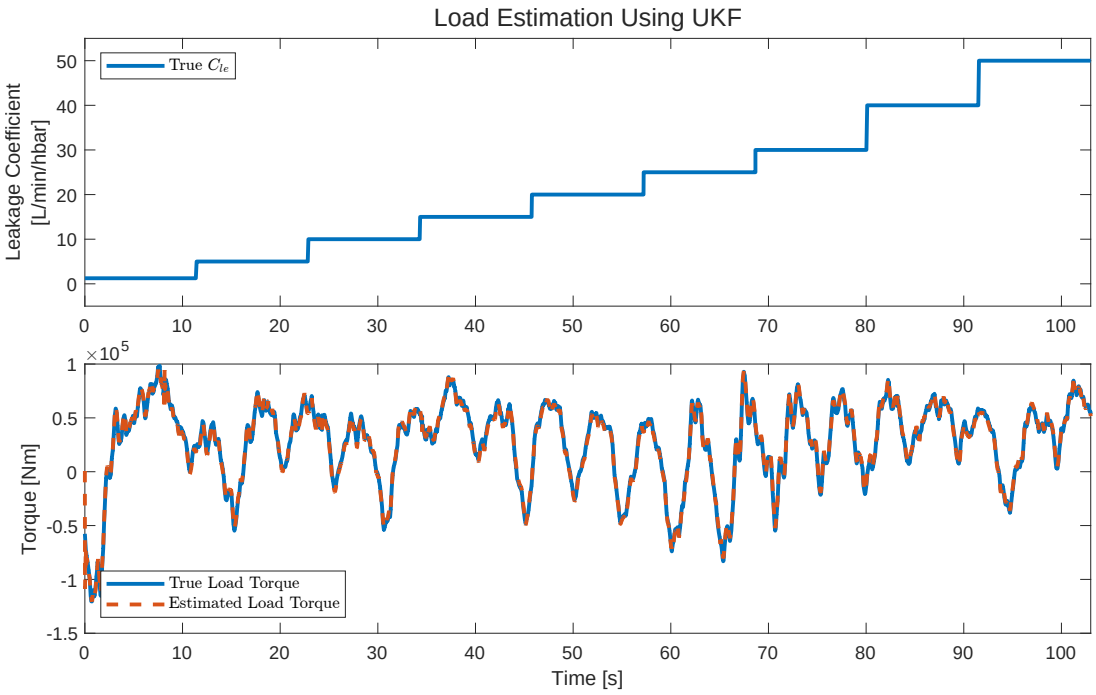

Figure 7.9. Results of load estimation at different leakages.

It is also found that the same result can be achieved by modelling the load as slow varying, just as the leakage coefficient, with the state transition function expansion shown in Equation (7.24):

$$\begin{bmatrix} \dot{\hat{\mathbf{x}}} \\ \dot{\hat{\tau}}_{load} \end{bmatrix} = \begin{bmatrix} \mathbf{f}\left(\hat{\mathbf{x}}, u\right) \\ 0 \end{bmatrix} \tag{7.24}$$

Since this load model is simpler to implement, this model is used going forward. Figure 7.9 shows that not only is the Unscented Kalman Filter able to estimate the wind load on the cylinder, it is also robust against leakage faults, even without full state feedback.

As the load estimation is seen to accurately estimate the load torque, Figure 7.10 shows an approach to estimate the leakage coefficient, by feeding the load estimation into the UKF that estimates the leakage. The load torque estimate is simply inputted to the leakage estimating UKF as a parameter and is not included in the state vector.

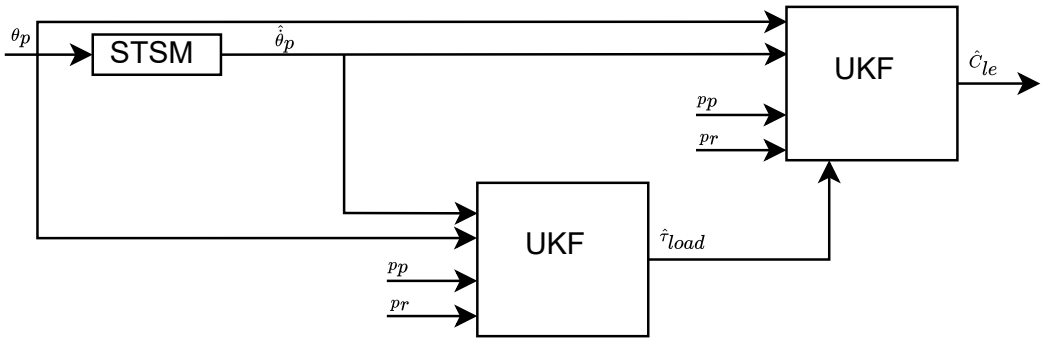

Figure 7.10. Block diagram of the leakage estimation structure using a UKF to estimate the load torque and feeding it to the leakage estimator.

This setup gives the results shown in Figure 7.11. Comparing to the results shown in Figure 7.8, adding load estimation to the leakage estimation structure seems to give little improvement. However, the load estimate might help make the leakage estimator more robust against parameter variations. Therefore the load estimator will be included going forward.

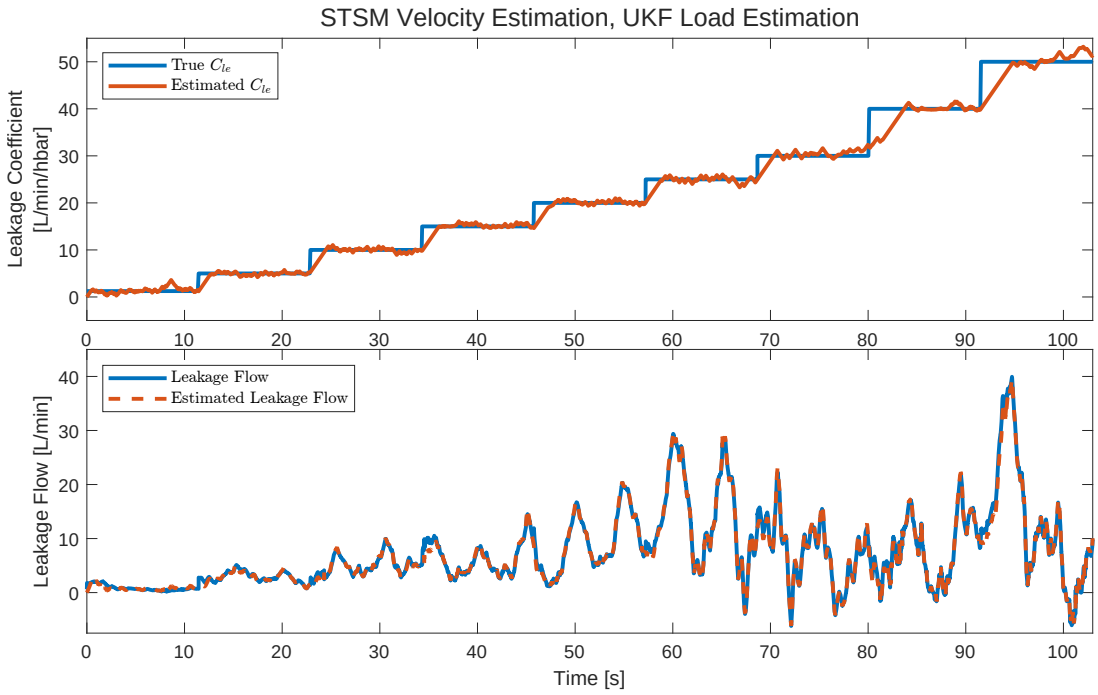

Figure 7.11. Results of leakage estimation with STSM velocity estimation and UKF load estimation. The top graph shows the true and estimated leakage coefficient, the bottom graph shows the true and estimated leakages flow.

7.2.4 Noise

Noise is now added to the measurement signals. This is done by adding Gaussian noise with 0 mean to measurements, with 0.2 bar standard deviation for the pressure sensors and 0.5 cm standard deviation for the position sensor corresponding to 0.005° when converting using the higher value of the Drive Jacobian. For the UKF to handle the noise, the noise covariance matrix R_k is tuned. The noise covariance matrix is here assumed to be diagonal. R_k is tuned by first setting the diagonals of R_k to the corresponding state sensor noise variance. As the noise variance from the STSM observer is not known, the $\dot{\theta}_p$ state being given the same variance as the position sensor. From here R_k is adjusted using trial and error. It is here found that the position and velocity, noise variance had to be increased to give a good result. For the velocity this makes sense as the STSM amplifies the noise in the position measurement. This can be seen in the right graph in Figure 7.12. The left graph of Figure 7.12 shows the leakage estimation performance.

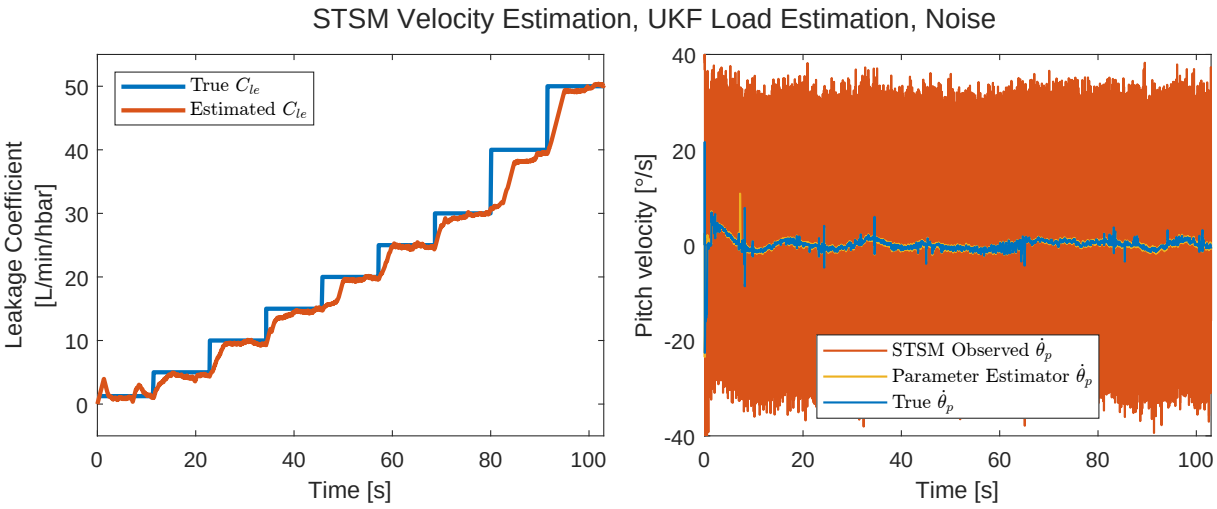

Figure 7.12. Results of leakage estimation with STSM velocity estimation and UKF load estimation with noise added to the feedbacks. The left graph shows the leakage estimate from the parameter estimating UKF compared to the true leakage. The right figure shows the velocity estimate from the STSM observer, the velocity estimated by the parameter estimator from the STSM estimate and the true velocity.

The results shown in Figure 7.12 are achieved after retuning both the measurement noise and process noise covariance matrices of both the leakage and load estimating UKF's. Figure 7.12 shows that even with very noisy velocity inputs from the unfiltered STSM, the UKF is still able to give a good estimate of velocity and through this a good estimate of the leakage, although the C_{le} estimate is slower reacting after the noise retuning. Tunings for higher pressure measurement noise, at a standard deviation of 1 bar, is shown in Appendix D.

7.2.5 Sampling Frequency

In the previous simulations the UKF's and STSM observers have been running at the same sampling frequency as the fixed step solver of the model, that being 100 kHz. The sampling frequency of the UKF's and the STSM is now reduced to 1 kHz. This required some retuning of the process noise matrix to get a stable estimation. Figure 7.13 shows the results of estimation at this sampling frequency.

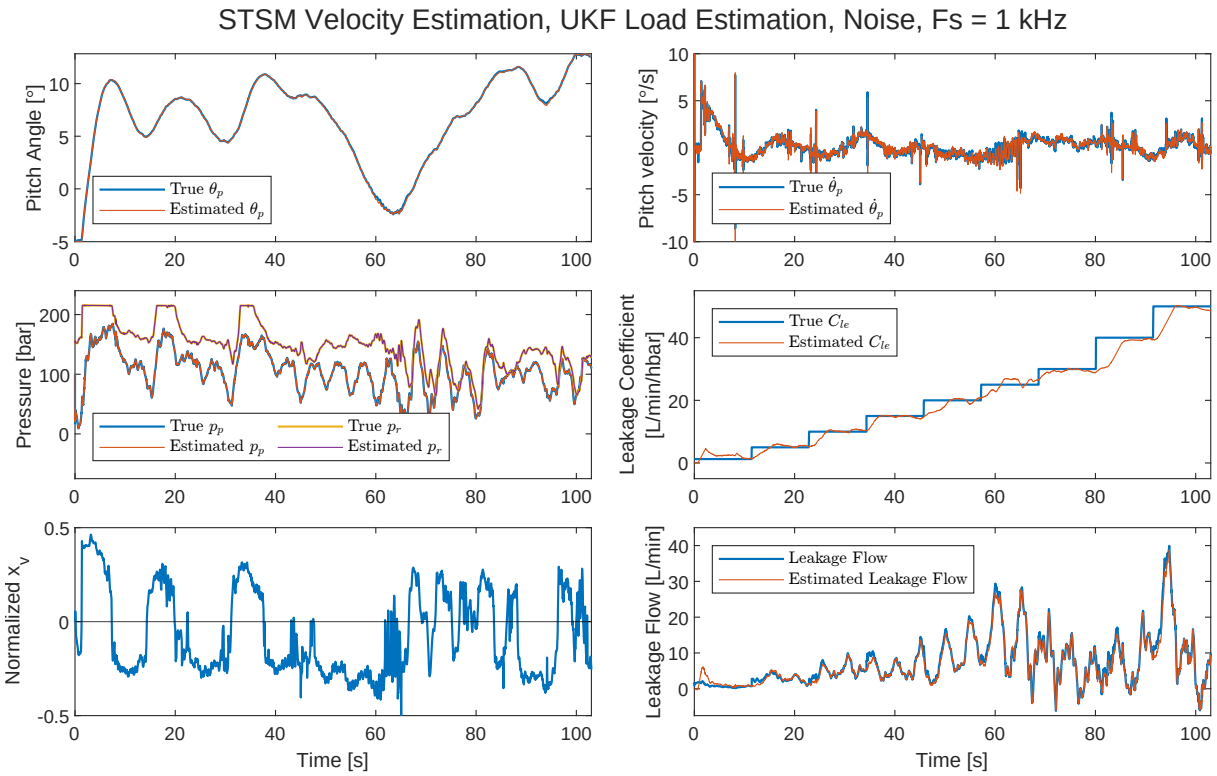

Figure 7.13. Results of leakage estimation with STSM velocity estimation and UKF load estimation, at a 1 kHz sampling frequency with noise added to the feedbacks. The figure shows the true value of the states and leakage coefficient, as well as their estimated values from the Kalman Filter. Valve position and leakage flow is also shown.

As can be seen leakage can still be estimated at this sampling frequency. The load estimation at this sampling frequency also tracks the load torque accurately, which is seen in figure 7.14

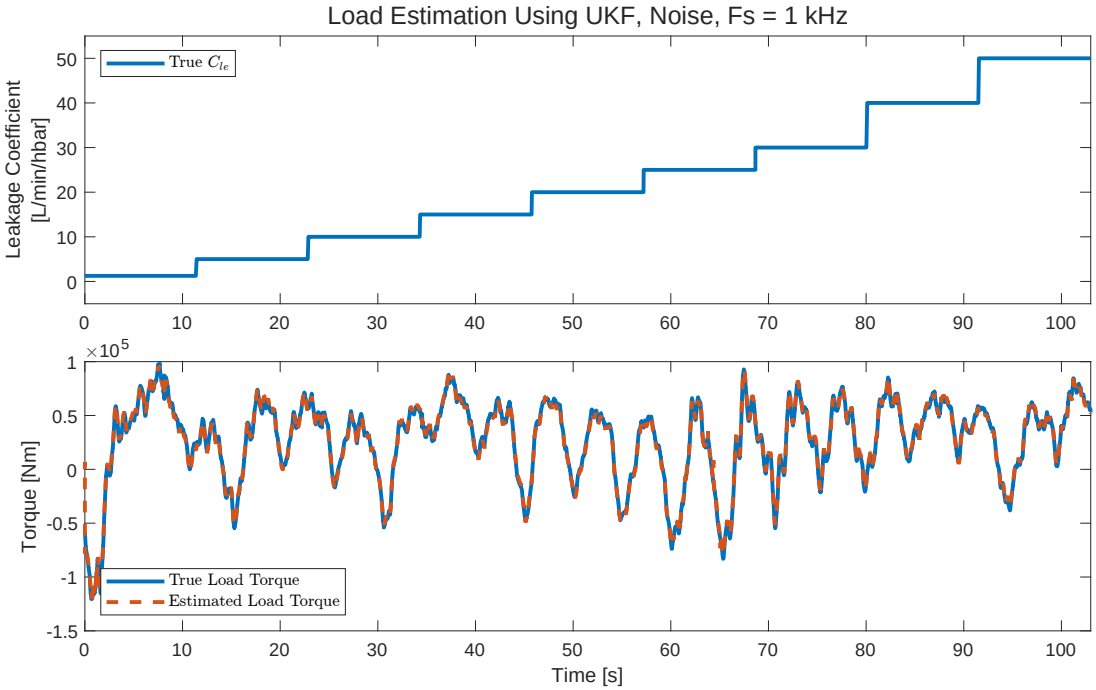

Figure 7.14. Results of load estimation at different leakages, at a 1 kHz sampling frequency with noise added to the feedbacks.

Finally the varying supply pressure from the accumulator is in included in the model. Measurements of the accumulator pressure is low pass filtered by a 25 Hz first order filter and then fed into the UKF's in the same way as the load estimate is fed to the UKF leakage estimator. The low pass filter is added to remove noise in the measurement signal and is place at 25 Hz as it is assumed that the dominating dynamics of the accumulator pressure are significantly slower than this frequency.
It is found that varying supply pressure has little effect on the leakage estimate. Results of varying supply pressure, along with additional figures for the other tests, can be found in Appendix F.

7.2.6 Robustness Tests

To ensure that leakage estimation structure is robust against system variation, test simulations are conducted where model parameters are varied in the simulation model but not the state transition functions of the UKF's. This is done to emulate the variations that occur in production or during operation. Tests are conduced by changing one model parameter and keeping it constant for a full simulation. The parameters being varied can be seen in Table 7.1. For ρ, β, B_v and $\tau_{coulomb}$ the variation range used is the same as described in Section 4.2.1. The piston mass m_p is varied by $\pm 5\,\%$ while the bearing inertia is varied by $\pm 50\,\%$. The variation bearing inertia is chosen to be this high as the inertia of the turbine blade is expected to vary significantly when deflecting due to wind loading. Table 7.1 shows the base value and variation range of the parameters being varied.

Parameter:	ρ	$\beta_{0_{pp}}$	$\beta_{0_{pr}}$	B_v
Base Value:	885 kg/m^3	10 000 bar	10 000 bar	175 Nm/(°/s)
Variation:	850-900 kg/m^3	6-10 kbar	8-12 kbar	50-2000 Nm/(°/s)

Parameter:	$\tau_{coulomb}$	m_p	J_b
Base Value:	2000 Nm	104 kg	380 kgm^2
Variation:	0-10000 Nm	99-109 kg	190-570 kgm^2

Table 7.1. Parameter variation range for the leakage estimation robustness tests.

All tests are conducted with a constant leakage at 20 L/min/hbar. Through this robustness testing it is found that the only parameters that affected leakage estimation performance was ρ and $\beta_{0_{pp}}$ variation. Specifically it is the lower value of the parameter variations that have the largest effect, though this is probably just caused by the variation being larger in this direction for both these variation ranges. The two results are shown in Figure 7.15 and 7.16. The rest of the robustness test results are shown in Appendix E.

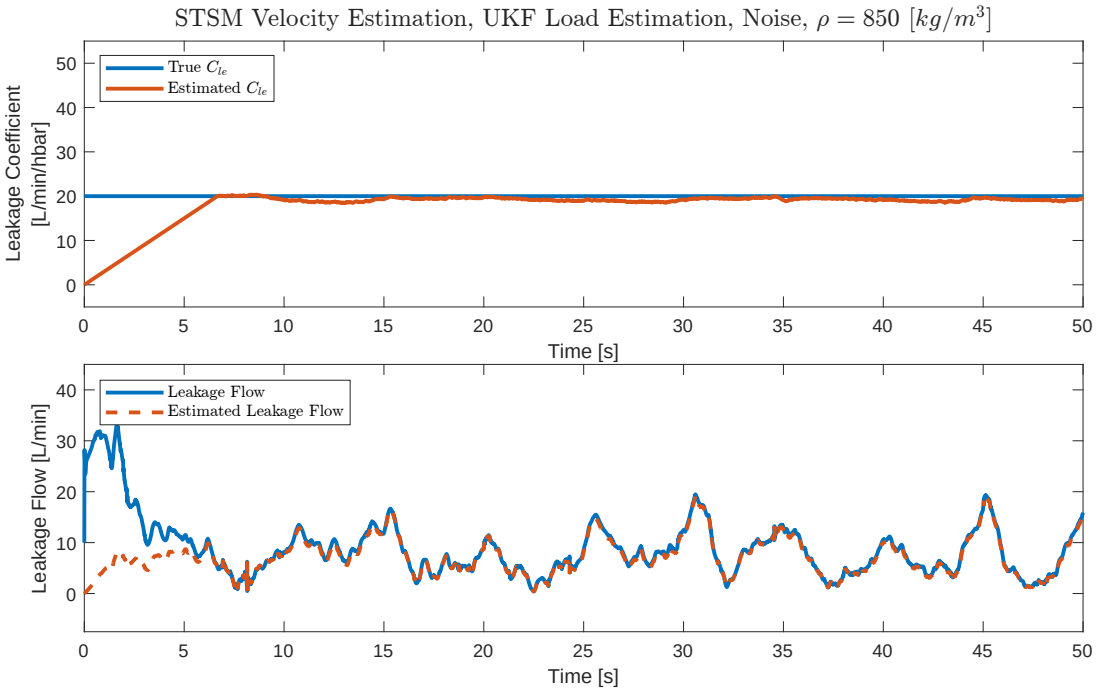

Figure 7.15. Results of leakage estimation with simulation model ρ reduced to 850 kg/m^3.

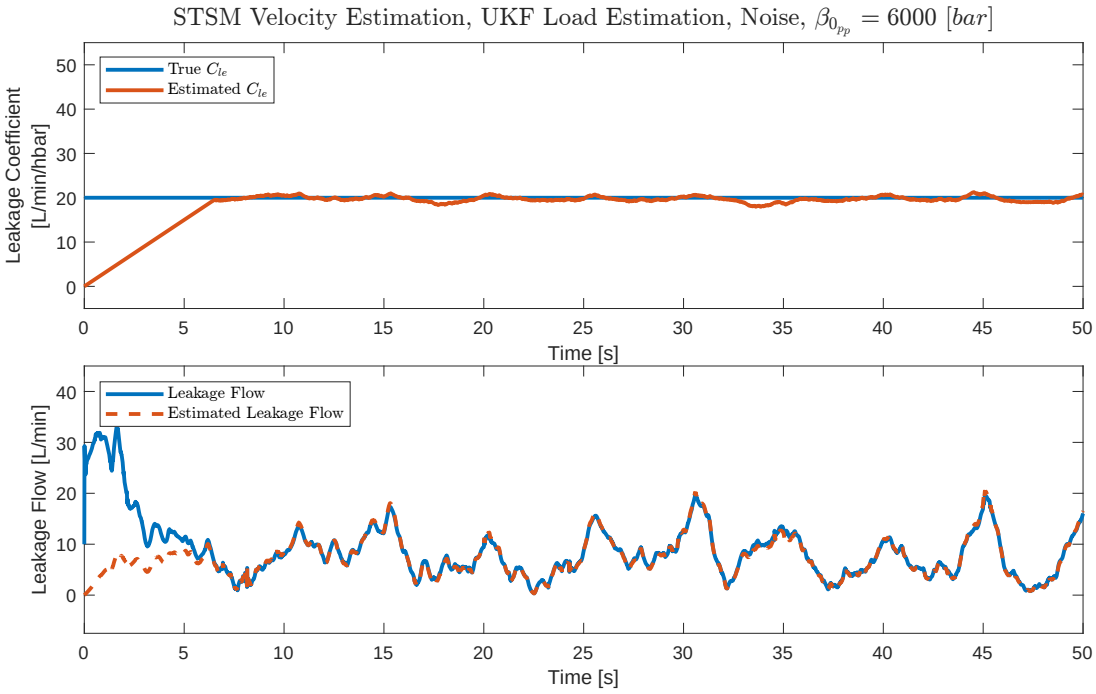

Figure 7.16. Results of leakage estimation with simulation model $\beta_{0_{pp}}$ reduced to 6000 bar.

Here it can be seen that even the parameters with the most effect on the leakage estimation have little effect. As shown in Section 4.2.1 the parameters with the most effect on the system dynamics are ρ, β_p and B_v, therefore it makes sense that variations in ρ and $\beta_{0_{pp}}$ have the most effect on the leakage estimation. The reason B_v does not effect the leakage estimate is because variations in the friction are included in the load estimate and are therefore mitigated. This is also the case for the variations in piston mass and bearing inertia. As the inertia of the

turbine blades are known to vary significantly during operation due to blade deflection, the load estimator could be pivotal in achieving accurate leakage estimation in practise.

7.3 Summary

In this chapter an estimation structure has been set up to estimate internal leakage in the cylinder of the pitch system. It has here been shown that internal leakage can be estimated using an Unscented Kalman Filter. It is shown to work with noise at a sampling frequency of 1 kHz, using an STSM observer to estimate the pitch velocity state, and a secondary Unscented Kalman Filter to estimate the load torque. This estimation method is also shown to be robust against large parameter variations.

Fault Tolerant Control Strategy 8

This chapter introduces the designed control structure that is developed to be fault tolerant towards an internal leakage fault in the wind turbine pitch system. This includes analysing the impact that an internal leakage fault has on the system. Additionally, the designed Fault Tolerant Controller is tested at different wind speeds and leakage levels, using the leakage estimation developed in Chapter 7.

8.1 Analysis of leakage fault

As seen in the end of Chapter 5, introducing a leakage fault to the pitch system has a negative impact on the tracking performance of the developed controller. Therefore, this section aims to understand how introducing a leakage fault impacts the dynamics of the pitch system. In Chapter 4 a system analysis was performed where different system parameters were varied including the leakage coefficient. Here it was found that a change of leakage influences the pole location of the dominant first order dynamic of the system as well as increasing the system damping, however, it does not change the location of the resonance peak. As the most notable effect is the change of the first order pole location, a relation is found between the varying leakage coefficient and the location of the first order pole. This relation can be seen in Figures 8.1 and 8.2. The left figure is a bode plot of the pitch system when varying the leakage coefficient with a zoom on the first order pole and how it is affected and the right figure is the pole location plotted as a function of the leakage coefficient C_{le}.

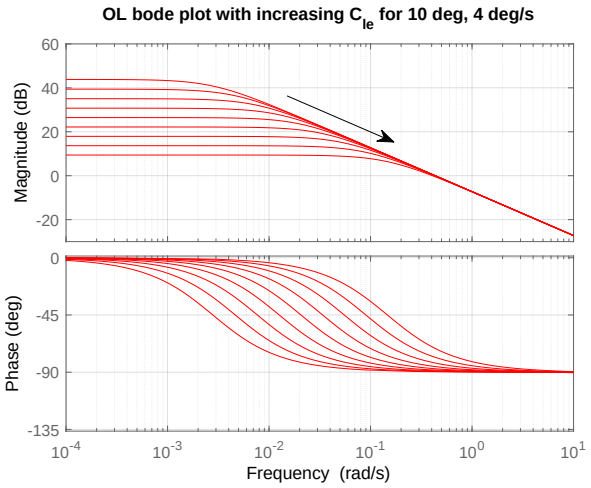

Figure 8.1. Varying the leakage coefficient is seen changing the location of the first order pole in the direction of the arrow.

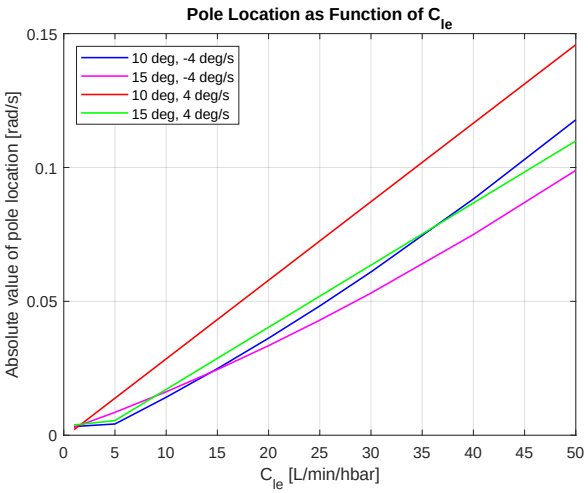

Figure 8.2. The location of the first order pole is plotted as a function of the leakage coefficient for different linearization points.

As was found in the system analysis, the system dynamics change dependent on the pitch angle and velocity. Therefore, in Figure 8.2 four different plots of the relation between the pole location and C_{le} are seen to determine if the relation change when changing the linearization points. The figure shows that in the low frequency region for leakage coefficients below 5 L/min/hbar a small deviation occurs. However, for leakage coefficients above 5 L/min/hbar the relation is seen to follow an almost straight line. Hence, if the low frequency region is neglected the relation between the pole location and the leakage coefficient can be approximated as a linear function:

$$\omega_{pole} = a \cdot C_{le} \tag{8.1}$$

In Table 8.1 the slope, a, of each of the approximated linear relations for each of the linearization points is seen as well as the mean slope.

Linearization Point	10°, $-4\,\frac{\text{rad}}{\text{s}}$	15°, $-4\,\frac{\text{rad}}{\text{s}}$	10°, $4\,\frac{\text{rad}}{\text{s}}$	15°, $4\,\frac{\text{rad}}{\text{s}}$	Mean Slope
Slope, $a\ \left[\frac{rad/s}{L/min/hbar}\right]$	0.0023	0.0018	0.0029	0.0023	0.0023

Table 8.1. The slope of the linear approximation between pole location and leakage coefficient.

From Table 8.1 it is noted that the slope of each of the different linear approximations are close to being equal. This means that the same change in the leakage coefficient for two different linearization points with a different pole location will change the location of the pole by the same distance. This is expressed in Equation (8.2):

$$\Delta\omega_{pole} = a \cdot \Delta C_{le} \tag{8.2}$$

To further investigate the impact of a leakage fault on the developed controller, Figure 8.3 shows open loop bode plots with the PI-pole controller and varying leakage coefficients:

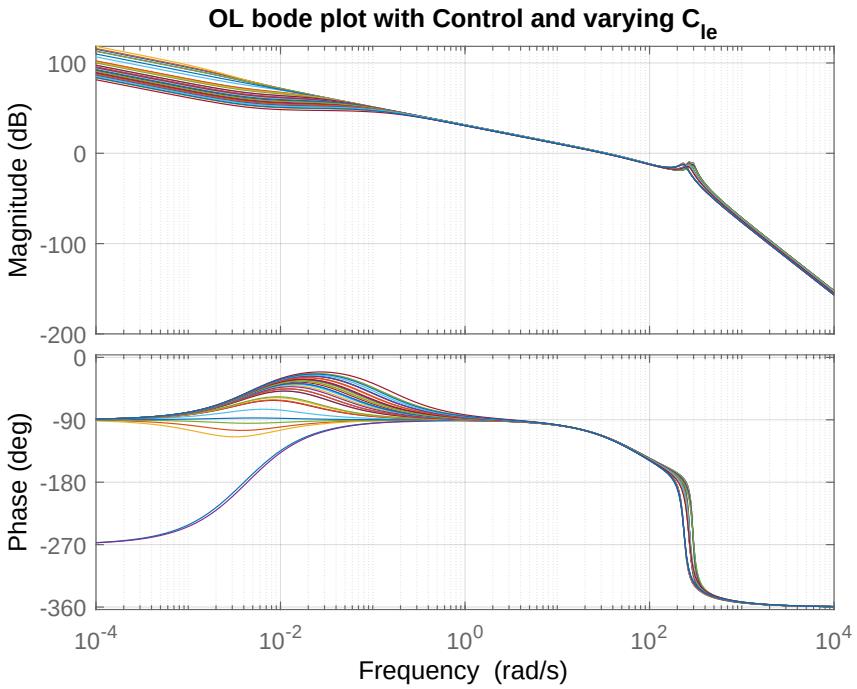

Figure 8.3. OL bode plot with PI-pole controller in four different linearization points with varying leakage coefficients.

This shows that an increase in leakage results in an increase in the phase characteristics, as the first order pole dynamic becomes faster, however the zero of the PI-pole controller remains stationary. The next section therefore investigates the possibility of redesigning the PI-pole controller such that it can adapt to different leakage coefficients in the system.

The developed nominal control structure also included a passive flow feed forward term. Figure 8.4 shows how the passive FFW follows the trajectory when the system is introduced to a series of increasing leakage faults.

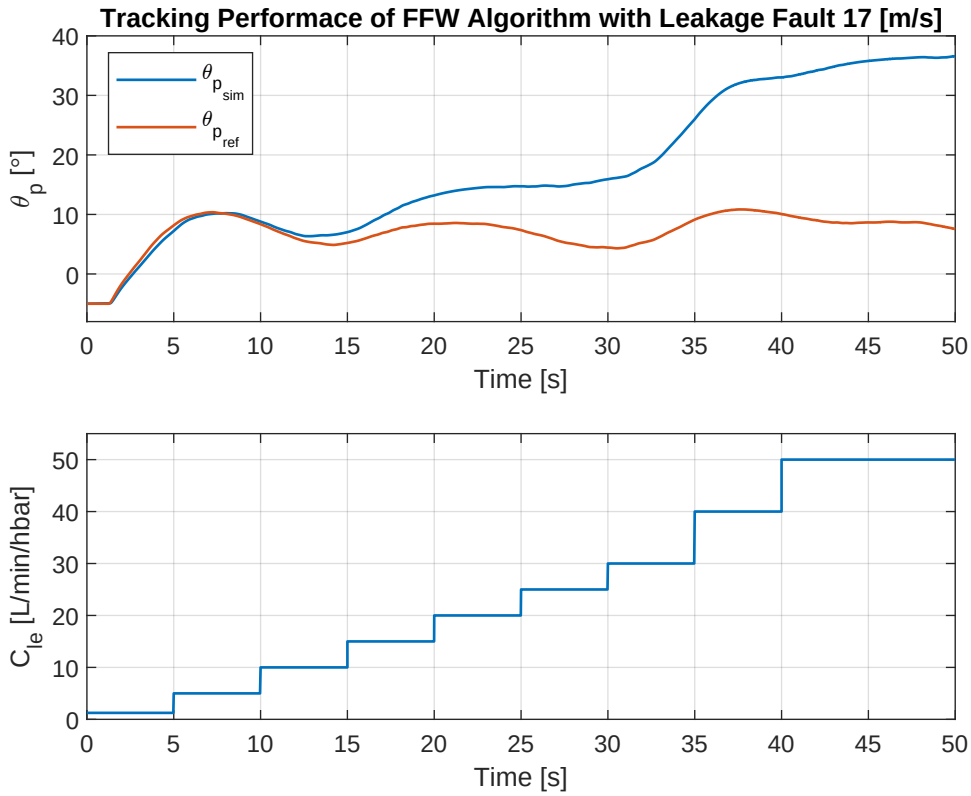

Figure 8.4. Tracking performance of the passive flow feed forward control with different leakage fault levels.

The figure shows that an increase in leakage results in a worsened tracking performance, as the pitch angle drifts further away from the reference when leakage is increased and no position controller is implemented. This decreased performance of the passive FFW increases the control effort required from the nominal controller, G_c, which is not desired. Therefore, an active FFW with leakage compensation is designed later in this chapter such that the FFW is tolerant towards a leakage fault.

8.2 Adaptive Zero Placing PI Controller

Throughout this section and Section 8.3 it is assumed that the leakage coefficient is known accurately in the FTC designs and can be used as a feedback. This implies that the analyses presented in these sections are with a known leakage. Therefore, the performance of the FTC designs can first be determined when the actual leakage estimation presented in Chapter 7 is incorporated in the feedback.

In Equation (8.3) the nominal PI-pole controller designed in Chapter 5 on page 29 is seen:

$$G_c(s) = K\frac{K_P s + K_I}{s}\frac{1}{s+\omega_{pole}} \tag{8.3}$$

Where the controller gains were chosen as, $K = 3162.7$, $K_P = 1$, $K_I = 0.005$ and $\omega_{pole} = 75$. As the proportional gain is chosen to be, $K_P = 1$, the zero of the PI-pole controller is located at $K_I[rad/s]$. Remembering that a change in leakage results in a change in pole location for the

first order pole dynamics, the idea of the Adaptive Zero Placing (AZP) PI Controller is to change the location of the controller zero by the same distance the pole has moved. This is possible if the leakage coefficient is used as a feedback to the controller which is described in Equation (8.4):

$$\begin{aligned} \Delta\omega_{zero} &= \Delta\omega_{pole} \\ &\Updownarrow \\ \Delta\omega_{zero} &= a \cdot \Delta C_{le} \end{aligned} \tag{8.4}$$

The equation above describes how a change in leakage should change the zero location. The actual zero location is then given as:

$$\omega_{zero} = K_I + a \cdot \Delta C_{le} \tag{8.5}$$

Where, K_I is the value from the nominal controller designed for the healthy system. Here it should be noted that the choise of the slope, a, determines how aggressive the controller is. As the linear model and the relation between the leakage coefficient and the first order pole location are approximations, the slope, a, should be chosen rather conservatively, such that the zero does not move further to the right of the pole. Therefore the slope is chosen as, $a = 0.0017$. Inserting Equation (8.5) into the controller transfer function yields:

$$G_c(s) = K\frac{K_P s + (K_I + a \cdot \Delta C_{le})}{s}\frac{1}{s + \omega_{pole}} \tag{8.6}$$

Figure 8.5 shows a block diagram, visualizing how the designed adaptive zero placing PI-pole controller is implemented in SimuLink.

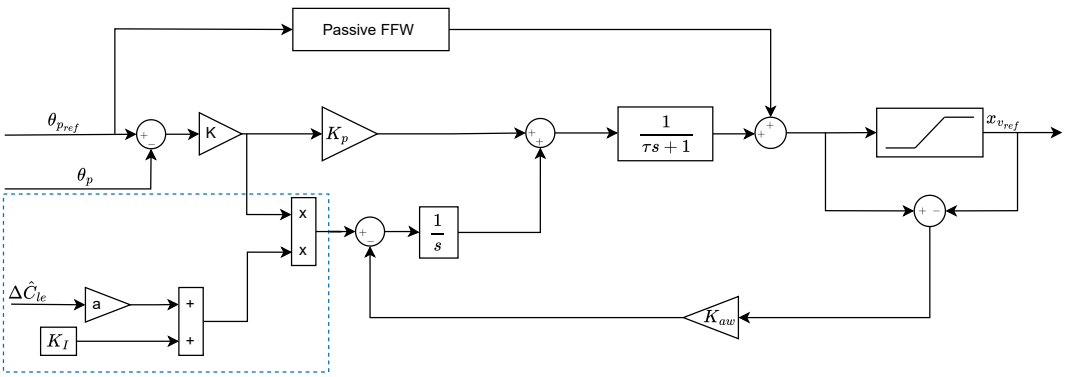

Figure 8.5. Block diagram of the designed adaptive zero placing PI-pole controller

Figure 8.6 shows the bode plot of the AZP PI controller at different leakages with perfect leakage coefficient estimation. Figure 8.7 shows the AZP PI controller at different leakages with a 100 % positive offset in the leakage coefficient estimate.

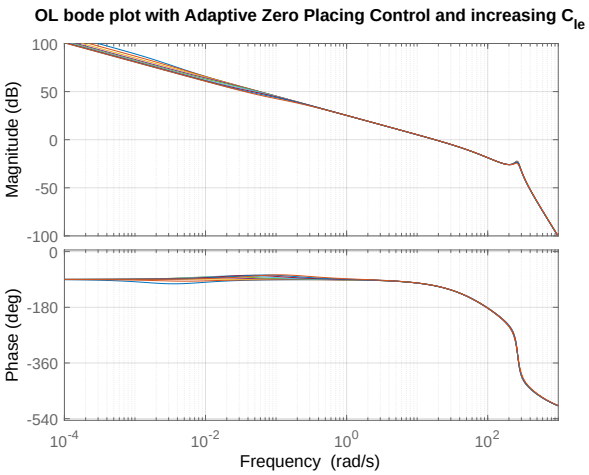

Figure 8.6. Open loop bode plot with the Adaptive Zero Placing Controller implemented.

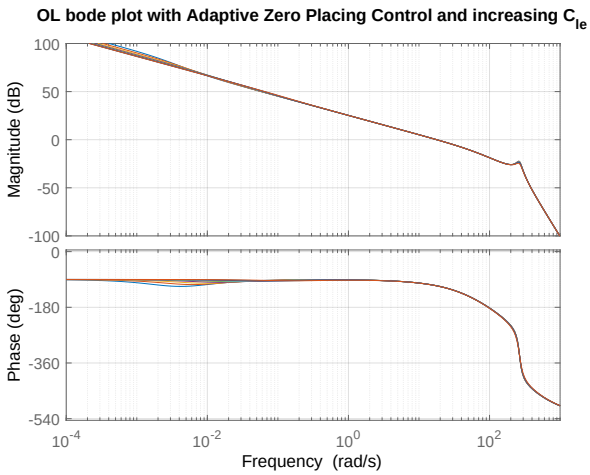

Figure 8.7. Open loop bode plot with the Adaptive Zero Placing Controller implemented with a 100 % offset in the leakage estimation.

In Figure 8.7 it can be seen that even with a 100 % offset in $\hat{C}_{le}$ the controller is not significantly affected. There are however further stability concerns for this type of controller. If the leakage coefficient estimate comes unstable and grows toward infinity then the controller will become unstable. This problem might be alleviated by imposing limits on how large $\Delta\hat{C}_{le}$ can become. This will however also limit the maximum leakage the controller and account for. Additionally a varying estimation error might induce dynamics in the controller that can potentially lead to instability, especially when implemented on a physical setup. Further stability analysis will therefore have to be conducted if this controller is to be implemented.

8.3 Active FFW with Leakage Compensation

As seen in Section 8.1 the tracking performance of the passive FFW is worsened significantly, when leakage faults are introduced to the system. Therefore, this section aim to design an active FFW that includes leakage coefficient feedback to account for leakage flow and therefore different leakage faults. In the passive FFW algorithm only the Q_p orifice equation was used to determine a valve input reference from the pitch velocity reference, however a more precise estimation of the valve input would be to include the leakage flow in the FFW algorithm as well as using pressure feedback to determine the pressure drop across the proportional valve and pressure difference in the cylinder chambers. Equation (8.7) describes the new relation between velocity reference and Q_p flow reference:

$$\begin{aligned} Q_{p_{ref}} + Q_{le} &= \dot{\theta}_{pref}\mathcal{J}(\theta_{p_{ref}})A_p \\ &\Updownarrow \\ Q_{p_{ref}} + C_{le}\,(p_r - p_p) &= \dot{\theta}_{pref}\mathcal{J}(\theta_{p_{ref}})A_p \end{aligned} \tag{8.7}$$

Inserting the orifice equation describing the flow Q_p and isolating for the valve opening area yields Equation (8.8), where the leakage coefficient C_{le} is substituted with the estimated leakage

coefficient $\hat{C_{le}}$. As is described in [7], the open loop velocity control, the active FFW, should compensate the system dynamics within the frequency range of the velocity reference. As the frequency content of the velocity reference is the same as the frequency content of the pitch angle reference it is known that the active FFW should compensate the system dynamics in low frequencies. Therefore, the pressures fed back to the active FFW are low pass filtered:

$$A_{ref} = \begin{cases} \dfrac{\dot{\theta}_{p_{ref}} \mathcal{J}(\theta_{p_{ref}}) A_p - \hat{C}_{le} \left(p_{r_{LPF}} - p_{p_{LPF}}\right)}{C_d \sqrt{\dfrac{2}{\rho}} \sqrt{|p_S - p_{p_{LPF}}|} \text{sign}(p_S - p_{p_{LPF}})} \ , \ \dot{\theta}_{p_{ref}} \geq 0 \\ \dfrac{\dot{\theta}_{p_{ref}} \mathcal{J}(\theta_{p_{ref}}) A_p - \hat{C}_{le} \left(p_{r_{LPF}} - p_{p_{LPF}}\right)}{C_d \sqrt{\dfrac{2}{\rho}} \sqrt{|p_{p_{LPF}} - p_T|} \text{sign}(p_{p_{LPF}} - p_T)} \ , \ \dot{\theta}_{p_{ref}} < 0 \end{cases} \tag{8.8}$$

Where $p_{p_{LPF}}$ and $p_{r_{LPF}}$ are the low pass filtered pressures. The break frequency of the first order low pass filters are chosen to 25 Hz, as this frequency is lower than the eigenfrequency of the system, but faster than the dynamics the Active FFW is compensating for.

The relation between the valve opening area and the normalised spool position is given as a polynomial. Hence the valve spool position reference is determined as in Equation (8.9):

$$x_{v_{ref_{FFW}}} = A_{poly}(A_{ref}) \tag{8.9}$$

Where $x_{v_{ref_{FFW}}}$ is the spool position reference determined from the active FFW and A_{poly} is the polynomial function describing the relation between the opening area reference and the spool position reference. The polynomial is described in Section 5.2.1 on page 30.

To analyse the introduction of pressure feedback to the FFW algorithm, Equation (8.8) and (8.9) are linearized yielding:

$$x_{v_{ref}} = x_{v_{ref_{G_c}}} + x_{v_{ref_{FFW}}} = G_c \cdot E(s) + k_{1_{ffw}} p_{p_{LPF}} + k_{2_{ffw}} p_{r_{LPF}} + k_{3_{ffw}} \dot{\theta}_{p_{ref}} \tag{8.10}$$

Where $E(s)$ is the position error signal and $k_{1_{ffw}}, k_{2_{ffw}}, k_{3_{ffw}}$ are the linearization constants. Furthermore, Equation (8.10) assumes the linear model is a precise description of the system, such that the principle of superposition can be used to combine the Active FFW and linear controller output.

As the pressure feedbacks are low pass filtered, this introduces two new states to the system. The low pass filtered pressure states are described in Equation (8.11):

$$\dot{p}_{p_{LPF}} = \frac{p_p - p_{p_{LPF}}}{\tau_{p_{LPF}}} \qquad \wedge \qquad \dot{p}_{r_{LPF}} = \frac{p_r - p_{p_{LPF}}}{\tau_{r_{LPF}}} \tag{8.11}$$

Where τ is the time constant of the respective first order low pass filter. The augmented pitch system with active FFW and position control implemented is expressed in state space form through Equations (8.12) to (8.14):

$$\mathbf{x} = \begin{bmatrix} \theta_p & \dot{\theta}_p & p_p & p_r & p_{p_{LPF}} & p_{r_{LPF}} \end{bmatrix}^T \qquad \mathbf{u} = \begin{bmatrix} E(s) & \dot{\theta}_{p_{ref}} \end{bmatrix}^T \tag{8.12}$$

$$\mathbf{A} = \begin{bmatrix} 0 & 1 & 0 & 0 & 0 & 0 \\ k_5 & k_3 & k_1 & k_2 & 0 & 0 \\ \beta_{p_0} k_{10} & \beta_{p_0} k_9 & \beta_{p_0} k_7 & \beta_{p_0} k_8 & k_{1_{ffw}} \beta_{p_0} k_6 & k_{2_{ffw}} \beta_{p_0} k_6 \\ \beta_{r_0} k_{15} & \beta_{r_0} k_{14} & \beta_{r_0} k_{13} & \beta_{r_0} k_{12} & k_{1_{ffw}} \beta_{r_0} k_{11} & k_{2_{ffw}} \beta_{r_0} k_{11} \\ 0 & 0 & \frac{1}{\tau_{p_{LPF}}} & 0 & \frac{-1}{\tau_{p_{LPF}}} & 0 \\ 0 & 0 & 0 & \frac{1}{\tau_{r_{LPF}}} & 0 & \frac{-1}{\tau_{r_{LPF}}} \end{bmatrix} \tag{8.13}$$

$$\mathbf{B} = \begin{bmatrix} 0 & 0 \\ 0 & 0 \\ \beta_{p_0} k_6 G_c(s) & \beta_{p_0} k_6 k_{3_{ffw}} \\ \beta_{r_0} k_{11} G_c(s) & \beta_{r_0} k_{11} k_{3_{ffw}} \\ 0 & 0 \\ 0 & 0 \end{bmatrix} \qquad \mathbf{C} = \begin{bmatrix} 1 & 0 & 0 & 0 & 0 & 0 \\ 0 & 1 & 0 & 0 & 0 & 0 \\ 0 & 0 & 1 & 0 & 0 & 0 \\ 0 & 0 & 0 & 1 & 0 & 0 \end{bmatrix} \tag{8.14}$$

The state space model of the augmented system is used in Section 8.3.1 to analyse the impact of adding the Active FFW with leakage compensation to the control structure.

8.3.1 Active FFW analysis

As described the pressure feedbacks to the active FFW with leakage compensation are low pass filtered to minimize the high frequency effect of adding a positive feedback loop to the system. Figure 8.8 displays the open loop bode plot of the pitch system with active FFW implemented with low pass filtered pressure feedback. Figure 8.9 illustrates the effect of adding the active FFW to the control structure without low pass filtering the pressures.

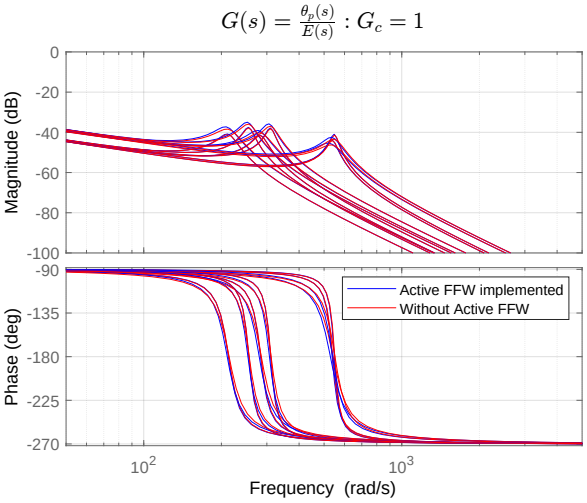

Figure 8.8. Bode plot of active FFW implemented with the pressures being low pass filtered.

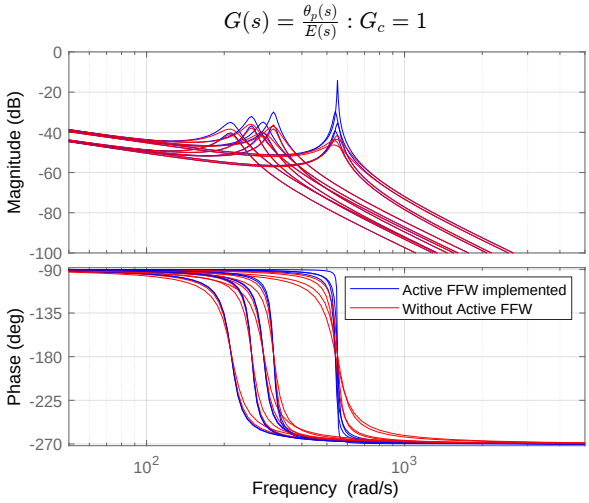

Figure 8.9. Bode plot of active FFW implemented without low pass filter.

As seen in Figure 8.9 the resonance peak magnitude increases, meaning a decrease of system damping. This decrease in damping could lead to an unstable system for some linearization points, which is the reason for low pass filtering the pressures. The linear implementation of the

active FFW is depicted in Figure 8.10, which shows the block diagram of the pitch system with implemented control. To further comment on figures 8.8 and 8.9 the addition of active FFW does not affect any low frequency dynamics of the system.

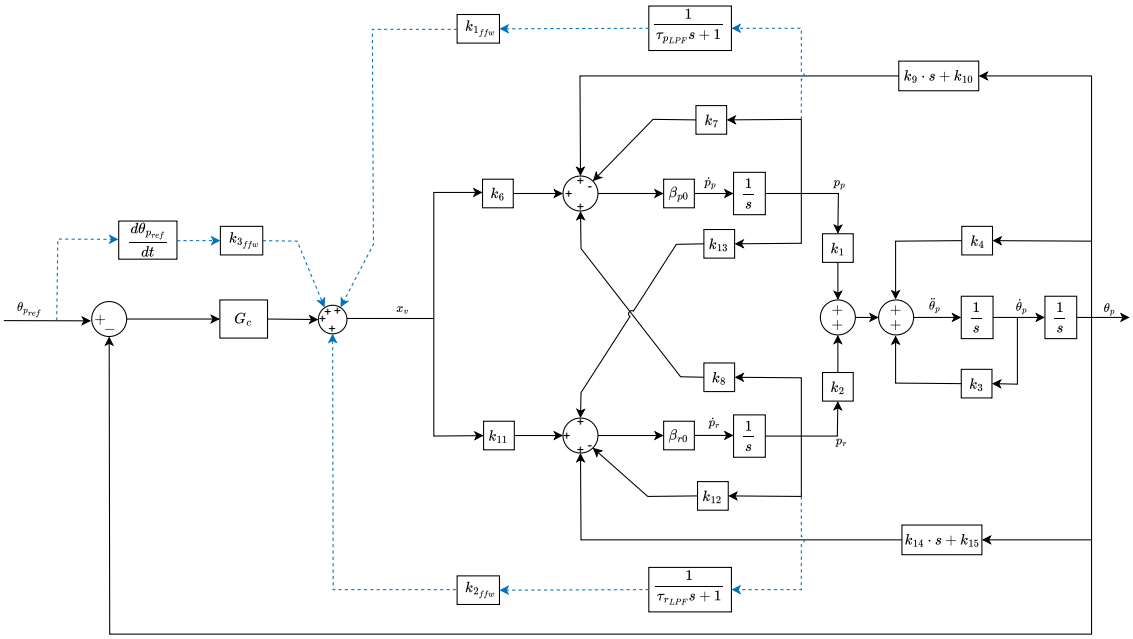

Figure 8.10. Block diagram of the linear system with active FFW implemented. The dotted blue lines indicate the feedbacks are introduced as part of the active flow feed forward.

As shown in Section 8.1, the tracking performance of the passive FFW radically decreased as leakage increased in the system. Figures 8.11 and 8.12 compares the tracking performance of the active and passive FFW when the load torque disturbance is removed from the system, where Figure 8.11 shows the active FFW and Figure 8.12 is the passive FFW. This comparison shows that the active FFW with leakage compensation has increased tracking performance when the system is introduced to different leakage faults.

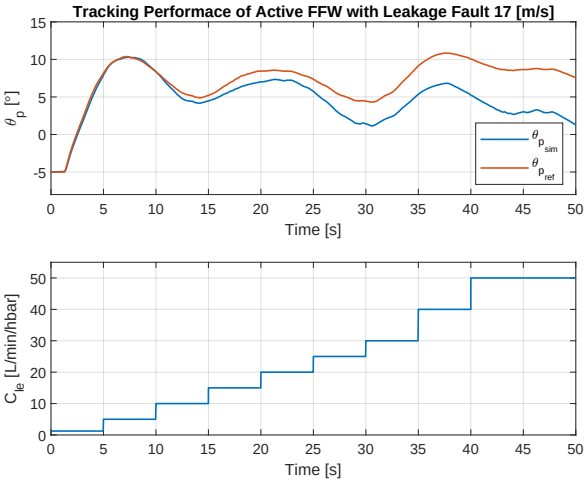

Figure 8.11. Tracking Performance of active FFW with leakage compensation, when the system is introduced to a series of leakage faults.

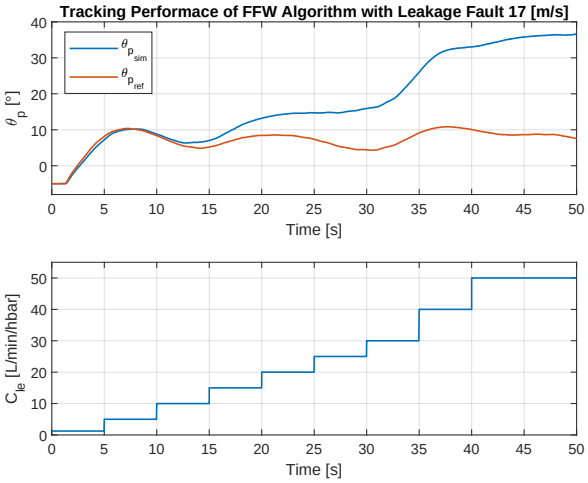

Figure 8.12. The same figure as Figure 8.4. Tracking of Passive FFW with leakage faults introduced.

The implementation of the Active FFW with leakage compensation in SimuLink is seen in Figure 8.13. It is seen that the Active FFW is implemented with two saturation blocks, where the Active FFW has a saturation block implemented to only saturate the FFW output, while a second saturation block is implemented to saturate the output of the FFW added with the linear control output. This configuration makes sure the Active FFW never becomes unstable if leakage is over estimated. However, if the leakage is over estimated the Active FFW becomes a disturbance, which the controller then has to compensate for.

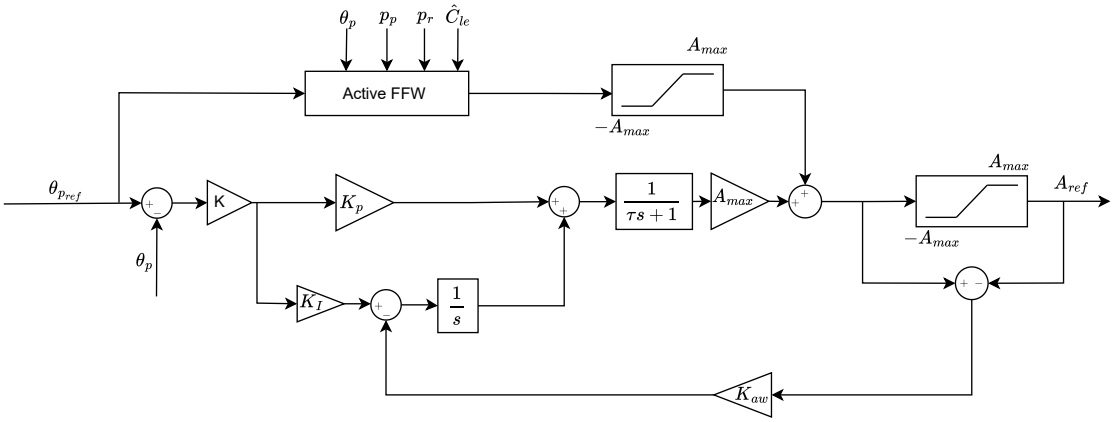

Figure 8.13. Block diagram with active flow feed forward implemented.

8.4 Fault Tolerant Control Implementation

Sections 8.2 and 8.3 presents two different approaches towards a fault tolerant control design. This section reviews the presented control strategies with the purpose of evaluating the performance of each FTC design as well as the possibility of combining the strategies. Below are listed the three different fault tolerant strategies which are considered in this evaluation.

- Passive FFW with AZP PI Controller (PFFW + AZP PI)
- Active FFW with AZP PI controller (AFFW + AZP PI)
- Active FFW with normal PI controller (AFFW)

To test the performance of the strategies, the different FTC controllers are simulated on the 17 m/s pitch trajectory reference, where the system is introduced to a series of different leakage faults that ranges between 5 to 25 L/min/hbar. This is seen in Figure 8.14, where the left side shows the tracking performance of the FTC and the left side shows the different steps in the leakage fault introduced to the system.

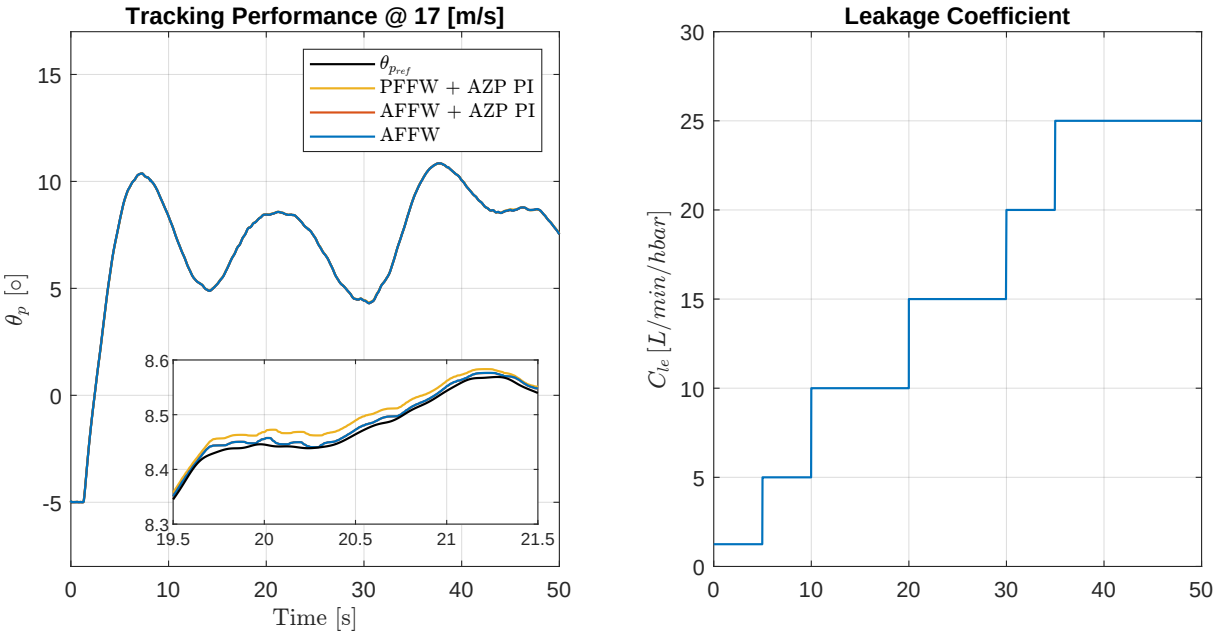

Figure 8.14. Comparing tracking performance of the different FTC designs.

From the zoomed plot in the figure it is seen that the AFFW and the (AFFW + AZP pi) is placed directly on top of each other, where the AZP PI has a decreased tracking performance. Table 8.2 presents the mean tracking error.

Control Structure	AFFW	AFFW + AZP PI	PFFW + AZP PI	Normal PI
Mean Tracking Error [°]	0.006	0.006	0.011	0.015

Table 8.2. The mean tracking error of the different control structures at 17 m/s pitch reference, when the system is introduced to a series of increasing leakage faults.

The table shows that the strategies including the Active FFW tracks the reference better than when it is not used, however all the different FTC approaches performs better than the designed PI pole controller for the nominal control system.

Taking into account, that the performance of the AFFW with AZP PI is the same as the AFFW with normal PI-pole controller, and remembering the possibility of the AZP PI controller becoming unstable as mentioned in Section 8.2, this project chooses to proceed with testing the Active FFW with the normal PI-pole controller.

8.5 Simulation Results using UKF leakage estimation

In the last section is was concluded that the best option of the designed FTC strategies is the Active FFW with leakage compensation and the normal PI-pole controller. The purpose of this section is to compare the FTC strategy to the healthy system control design. In order to evaluate the performance of the developed controller in as real conditions as possible, the Active FFW and the linear position controller are discretized using the Bilinear Transform, which can be seen in Appendix A. Here it should be noted that the gain of the position controller had to be reduced by 2.5 dB, while a low pass filter was added to the controller to have better noise attenuation in the controller. Furthermore, noise is also added to the measured states and the sampling frequency is 1 kHz. The accumulator is connected as supply pressure.

Additionally, the FTC strategy and the healthy system control design is tested on four different wind speed trajectories, 7, 11, 13 and 17 m/s for a period of 120 seconds, however only the last 100 seconds of the simulation is shown, to make sure the UKF has been initialized. During the simulation, the pitch system is introduced to two leakage faults, which is seen in Figure 8.15:

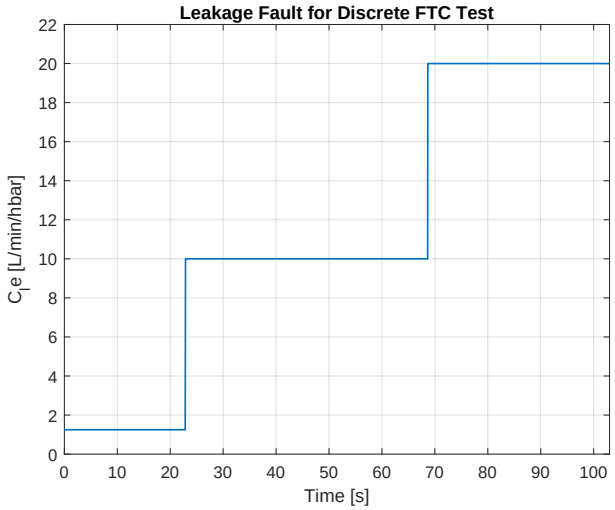

Figure 8.15. The introduced leakage levels for testing of the discrete fault tolerant control method.

Figures 8.16 to 8.19 shows the tracking performance at different wind speeds, where the upper plots shows the pitch reference and the actual pitch position, the middle plots shows the absolute error during tracking and the lower plots shows the leakage coefficient estimation.

Figure 8.16. Tracking Performance of discrete implemented control at 7 m/s using both FTC strategy and normal control strategy.

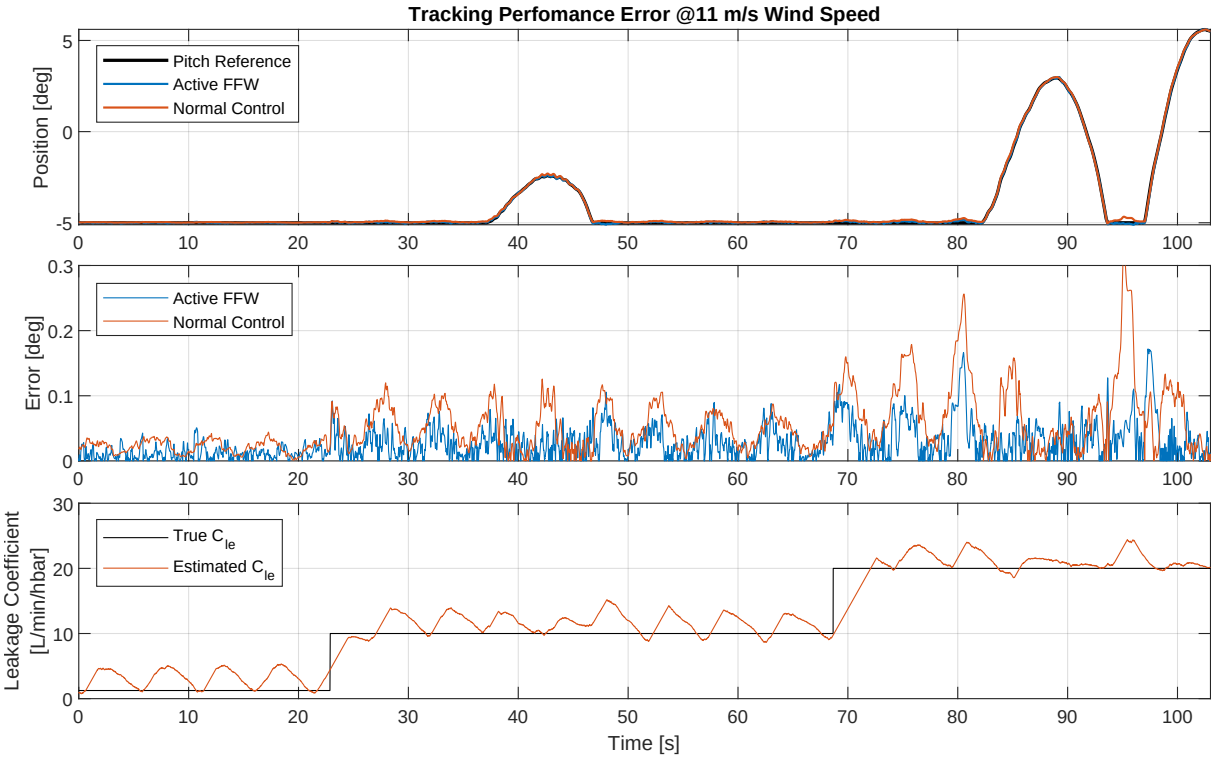

Figure 8.17. Tracking Performance of discrete implemented control at 11 m/s using both FTC strategy and normal control strategy.

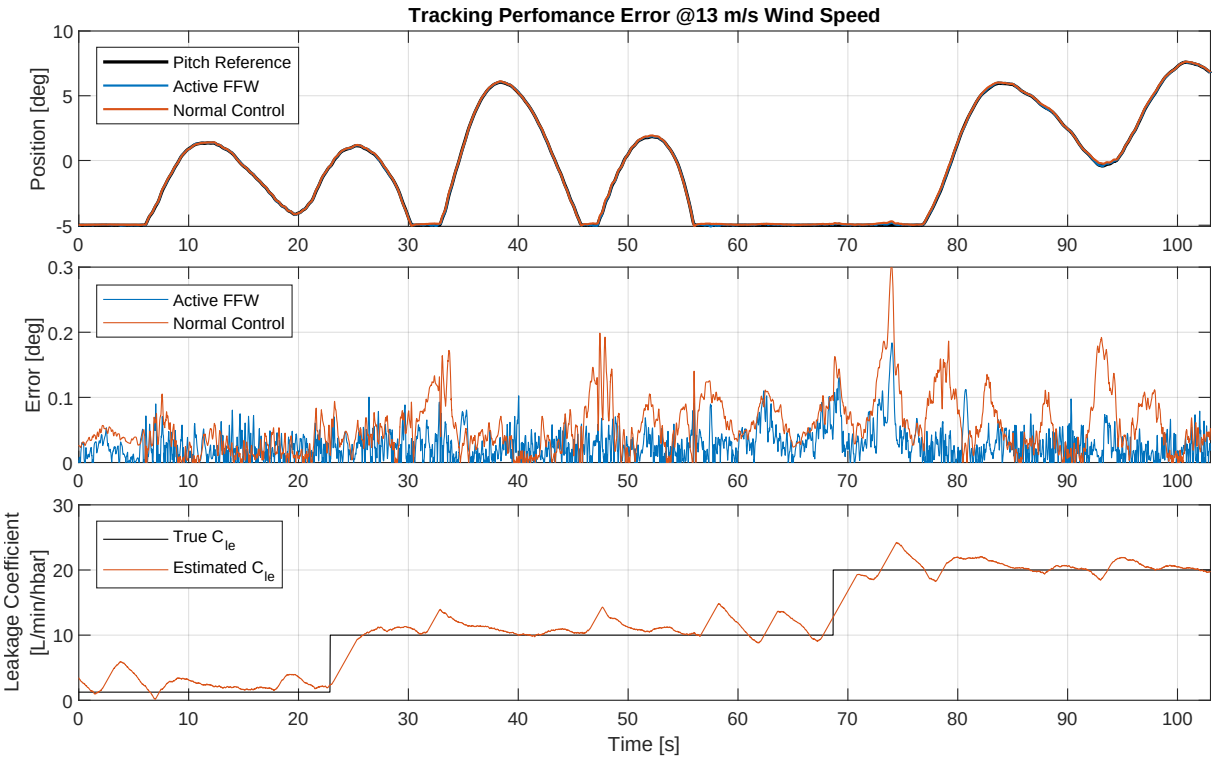

Figure 8.18. Tracking Performance of discrete implemented control at 13 m/s using both FTC strategy and normal control strategy.

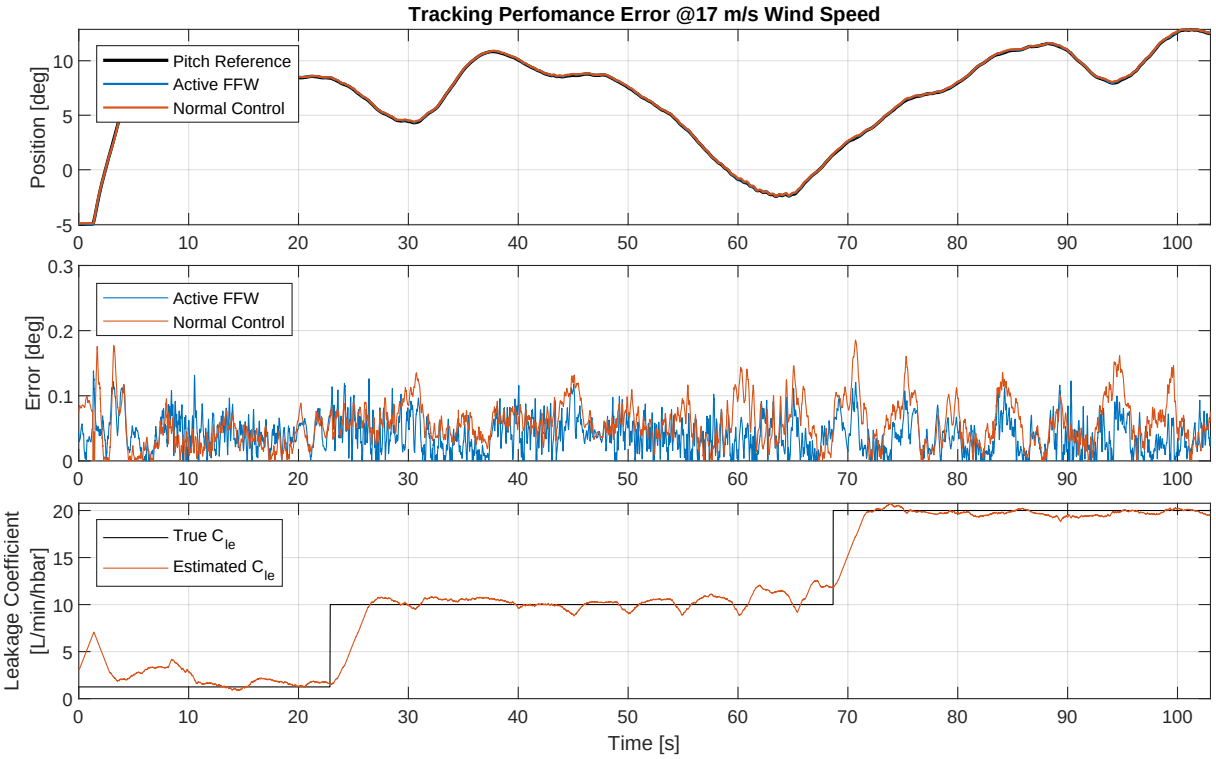

Figure 8.19. Tracking Performance of discrete implemented control at 17 m/s using both FTC strategy and normal control strategy.

Analyzing the data from the four simulations at different wind speeds, the mean and max tracking

error is seen in Table 8.3. Here it is seen that the Active FFW strategy performs better than the normal control for all the different wind speeds. However, it can be seen that the wind speeds of 7, 11 and 13 m/s has a lower mean error than the 17 m/s simulation, but the FTC strategy still performs better than the normal control. Furthermore, it can be seen that the maximum errors are lowered when using the active FFW implying that the Active FFW has better disturbance rejection as well as reacting faster to a sudden change in the reference.

Mean Error

Wind Speed	7 m/s	11 m/s	13 m/s	17 m/s
Active FFW	0.021°	0.027°	0.028°	0.04°
Normal Control	0.048°	0.053°	0.055°	0.057°

Max Error

Wind Speed	7 m/s	11 m/s	13 m/s	17 m/s
Active FFW	0.095°	0.172°	0.184°	0.138°
Normal Control	0.146°	0.331°	0.301°	0.185°

Table 8.3. Mean and max tracking error for Active FFW and Normal Control at different wind speeds.

To further comment on the results from Figures 8.16 to 8.19 it can be seen that lower wind speeds results in more oscillations in the leakage coefficient estimate. The frequency of the oscillations corresponds to the frequency of the load torque disturbance. However, the leakage estimate is still seen to be precise around the actual leakage value. Comparing the four figures it is noted that the leakage estimate has lager oscillations when the pitch angle is constant or below 0 degrees, whereas the precision of the leakage estimation becomes even better when pitching out of the wind at pitch angles larger than 0 degrees. This could be due to the fact that for constant pitch angles the velocity and acceleration is approximately zero, meaning the dynamic model used by the UKF might have a harder time to estimate the dynamic behaviour of these states.

Discussion & Further Work 9

9.1 Performance Testing

Since the AAU test bench was not available for testing, the controller is designed purely for analysis and simulation. This makes it difficult to get a full picture of the performance of the controller, especially when it comes to how aggressively it corrects for small errors. The performance of the controller should therefore be reevaluated after implementing on a physical setup. It seems that the linear controller has poor noise attenuation, despite the filter added during discretization in Appendix A on page 87.

9.2 Implementation Consideration

While the Unscented Kalman Filter is not the most computationally demanding parameter estimation algorithm, it is not a simple algorithm, and this project proposes implementing two separate UKF's. This combined with the 1 kHz sampling frequency could make the use of this control structure impractical. If this is the case it is possible that a tuning of the UKF's at a lower sampling frequency could alleviate this problem, as the controller structure is not dependent on high frequency leakage estimation. That is if such a tuning can be achieved. Additionally it is possible that a more efficient implementation of the UKF algorithm than the one used in this project exists.

Conclusion 10

As one of the most critical systems of a wind turbine is the pitch system, this project looked into the different faults that can happen in a pitch system. Here it was decided to investigate the impact of an internal leakage fault in the hydraulic pitch control system of a wind turbine. In order to investigate the impact an internal leakage fault has on a pitch system, the project developed a lumped parameter model describing the dynamic behaviour of the pitch system. Hereafter, a nominal PI-pole controller with an added passive FFW algorithm was designed and tested on a healthy pitch system, such that when an internal leakage fault was introduced to the system, the performance of the controller was comparable. This showed a decrease in tracking performance when an internal leakage fault was introduced, which led to the problem statement:

How can the control structure of a wind turbine pitch system be redesigned such that it is fault tolerant towards an internal leakage fault?

Secondary Question

- *How can leakage flow be estimated and implemented into a fault tolerant control structure for a hydraulic wind turbine pitch system?*

Using the developed linear model of the pitch system, it was found that introducing an increased internal leakage, the first order pole dynamic of the pitch system changed, as the pole became faster. Furthermore, the non-linear model was used to evaluate the performance of the passive FFW algorithm, which showed that the performance of the passive FFW became increasingly worse as the leakage in the pitch system increased. Based on the leakage fault analysis, two different Fault Tolerant Control methods were proposed to the system, Active FFW with leakage compensation and an Adaptive Zero Placing PI controller. Both the proposed FTC designs requires an estimation of the leakage coefficient. Therefore, the project decided to use an Unscented Kalman Filter to estimate the leakage coefficient, due to the non-linear behavior of a hydraulic pitch system. Here it was found that the UKF was able to estimate the leakage coefficient accurately, with and without knowing the load torque disturbance acting on the system. However, the estimated leakage had an increase in performance when the UKF had knowledge about the load torque disturbance. Therefore, a separate UKF was implemented to estimate the load torque, where it was found that the load torque could be estimated accurately, even without velocity feedback. The UKF designed to estimate the leakage was not able to work without having full state feedback. Therefore, the Super Twisting Sliding Mode algorithm was used as a differentiator to allow full state feedback. Testing the leakage and load UKF

estimators, they were found to be very robust towards parameter changes. Before testing the Fault Tolerant Control designs with the UKF leakage estimator, the proposed FTC designs were tested with an exact leakage feedback. Here it was found that the Active FFW with leakage estimation performed the best, while also being the most robust controller. Therefore, only the Active FFW was tested together with the UKF leakage estimator. The results showed that the Active FFW with leakage estimation performed without a decrease in performance related to the healthy system. The control structure was tested on different pitch reference trajectories and leakage levels, where it was found that the FTC controller performed better than the original controller in all test cases.

Bibliography

[1] Steve Sawyer et al. *Global Wind Energy Outlook 2016*. Tech. rep. GLOBAL WIND ENERGY COUNCIL, Sept. 2016.

[2] James Carrol, Alasdair McDonald and David McMaillan. 'Failure rate, repair time and unscheduled O&M cost analysis of offshore wind turbines'. In: *Wind Energy* (2015).

[3] Henrik C. Pedersen Alessio Dallabona Mogens Blanke and Dimitrios Papageogiou. 'Fault Diagnosis and Prognosis Capabilities for Wind Turbine Hydraulic Pitch Systems: An Overview'. In: (2023).

[4] Jesper Liniger. 'Design of Reliable Fluid Power Pitch Systems for Wind Turbines'. In: (2018). URL: https://doi.org/10.5278/VBN.PHD.ENG.00040.

[5] Marshall L. Buhl Jr. Jason M. Jonkman. *FAST User's Guide*. Tech. rep. National Renewable Energy Laboratory, Aug. 2005.

[6] J. Jonkman et al. *Definition of a 5-MW Reference Wind Turbine for Offshore System Development*. Tech. rep. National Renewable Energy Laboratory, Feb. 2009.

[7] Anders Hedegaard Hansen. *Fluid Power Systems: A Lecture Note in Modelling, Analysis and Control*. English. Fluid Mechanics and Its Applications. Germany: Springer, 2023. ISBN: 978-3-031-15088-3. DOI: 10.1007/978-3-031-15089-0.

[8] Bosch Rexroth. *4/2 and 4/3 proportional directional valves, direct operated, with electrical position feedback, without/with integrated electronics (OBE)*. Bosch Rexroth AG, 2024.

[9] M.W. Spong, S. Hutchinson and M. Vidyasagar. *Robot Dynamics and Control*. JOHN WILEY & SONS, INC., 1989. ISBN: 978-0-471-61243-8.

[10] Aalborg university. *Chapter 13: Non-linear model of pitch test setup*.

[11] Torben O. Andersen et al. 'COMPARISON OF LINEAR CONTROLLERS FOR A HYDRAULIC SERVO SYSTEM'. In: *The Japan Fluid Power System Society* (2005).

[12] C.L. Phillips and J.M. Parr. *Feedback Control Systems*. Prentice Hall, 2011. ISBN: 9780131866140. URL: https://books.google.dk/books?id=8Cy7bwAACAAJ.

[13] Eric A. Wan and Rudolph van der Merwe. 'The Unscented Kalman Filter'. In: *Kalman Filtering and Neural Networks*. John Wiley & Sons, Ltd, 2001. Chap. 7, pp. 221–280. ISBN: 9780471221548. DOI: https://doi.org/10.1002/0471221546.ch7. eprint: https://onlinelibrary.wiley.com/doi/pdf/10.1002/0471221546.ch7. URL: https://onlinelibrary.wiley.com/doi/abs/10.1002/0471221546.ch7.

[14] MathWorks. *Extended and Unscented Kalman Filter Algorithms for Online State Estimation*. MathWorks, 2024.

[15] E.A. Wan and R. Van Der Merwe. 'The unscented Kalman filter for nonlinear estimation'. In: *Proceedings of the IEEE 2000 Adaptive Systems for Signal Processing, Communications, and Control Symposium (Cat. No.00EX373)* (2000), pp. 153–158. DOI: 10.1109/ASSPCC.2000.882463.

[16] C. S. Pedersen, M. Fink and M. S. Jensen. *Modeling and Control of Hydraulic H-Bridge for Off-Highway Power Steering System*. Aalborg University, 2023.

[17] Leonid Fridman Yuri Shtessel Christopher Edwards and Arie Levant. *Sliding Mode Control and Observation*. 978-0-8176-4892-3. Birkhäuser, 2014.

Appendices

Linear Controller Discretization A

The linear controller is discretized using the Bilinear Transform. Through testing with noise on the position feedback it is found that the controller needs more noise attenuation to avoid over-actuation of the valve. This requires a filter to be place between the bandwidth of the controller and the bandwidth of the valve, with enough gain reduction at bandwidth of the valve to avoid noise feeding into the valve input, without reducing the phase margin of the controller too much. To this end a third order low pass filter is added at a frequency of 150 rad/s:

$$G_{filter} = 10^{\left(\frac{-2.5}{20}\right)} \cdot \frac{1}{\left(\frac{1}{150}s + 1\right)^3} \tag{A.1}$$

A -2.5 dB gain is added to maintain controller bandwidth. The result of adding this filter can be seen in the bode plot and step response shown in Figure A.1 and A.2 respectively.

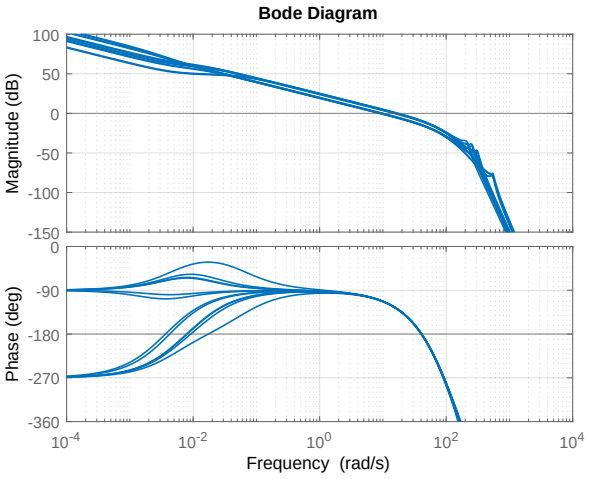

Figure A.1

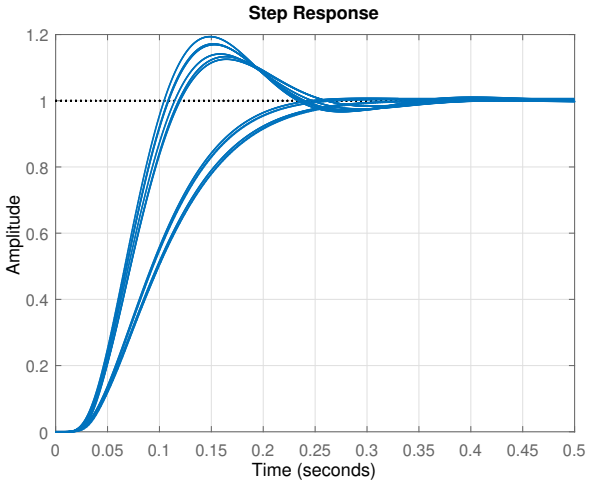

Figure A.2

Here it can be seen that the gain and phase at the valve frequency (314 rad/s) is greatly reduced. Phase margin has been increased resulting in an overshoot of up to 20 %. However, bandwidth remains at around 14 rad/s.

Super Twisting Sliding Mode Algorithm

B

The observer designed is based on [17] and is called a super twisting sliding mode observer. The pitch velocity estimation error is defined as:

$$\dot{\tilde{\theta}}_p = \dot{\hat{\theta}}_p - \dot{\theta}_p \tag{B.1}$$

The super twisting algorithm then determines the velocity estimate as:

$$\dot{\hat{\theta}}_p = -h_1\sqrt{\left|\tilde{\theta}_p\right|}sign(\tilde{\theta}_p) + \overline{w}, \qquad \dot{\overline{w}} = -h_2 sign(\tilde{\theta}_p) \tag{B.2}$$

If then the constants h_1 and h_2 are chosen as:

$$\begin{aligned} h_1 &= 1.5\sqrt{C_1} \\ h_2 &= 1.1C_1 \end{aligned} \tag{B.3}$$

Where C_1 is a bound on the pitch acceleration, stability of the observer is proved and a sliding mode on $(\tilde{\theta}_p, \dot{\tilde{\theta}}_p) = (0, 0)$ exist, hence the estimation error $\tilde{\theta}_p$ should ideally be zero, $\tilde{\theta}_p = 0$. The constant C_1 is found through a trial and error approach, where it is found that a value of $C_1 = 10$ rad/s^2 yields good results.

Kalman Filter Tunings C

This appendix lists the tunings from each test in Chapter 7.

C.1 Full State Feedback

Leakage Estimator

$$\alpha = 1e\text{-}4, \qquad \beta = 1.2$$

$$Q_k = \begin{bmatrix} 1e\text{-}8 & 0 & 0 & 0 & 0 \\ 0 & 1e\text{-}8 & 0 & 0 & 0 \\ 0 & 0 & 1e\text{-}6 & 0 & 0 \\ 0 & 0 & 0 & 1e\text{-}5 & 0 \\ 0 & 0 & 0 & 0 & 1e\text{-}1 \end{bmatrix}, \qquad R_k = \begin{bmatrix} 0.1 & 0 & 0 & 0 \\ 0 & 0.1 & 0 & 0 \\ 0 & 0 & 0.1 & 0 \\ 0 & 0 & 0 & 0.1 \end{bmatrix} \tag{C.1}$$

C.2 Unknown Load

Leakage Estimator

$$\alpha = 1e\text{-}4, \qquad \beta = 1.2$$

$$Q_k = \begin{bmatrix} 1e\text{-}4 & 0 & 0 & 0 & 0 \\ 0 & 1e\text{-}2 & 0 & 0 & 0 \\ 0 & 0 & 1e\text{-}6 & 0 & 0 \\ 0 & 0 & 0 & 1e\text{-}4 & 0 \\ 0 & 0 & 0 & 0 & 1e\text{-}2 \end{bmatrix}, \qquad R_k = \begin{bmatrix} 0.1 & 0 & 0 & 0 \\ 0 & 0.1 & 0 & 0 \\ 0 & 0 & 0.1 & 0 \\ 0 & 0 & 0 & 0.1 \end{bmatrix} \tag{C.2}$$

C.3 Dual Estimation

Leakage Estimator

$$\alpha = 1e\text{-}4, \qquad \beta = 1.2$$

$$Q_k = \begin{bmatrix} 1e\text{-}6 & 0 & 0 & 0 & 0 \\ 0 & 1e0 & 0 & 0 & 0 \\ 0 & 0 & 1e\text{-}6 & 0 & 0 \\ 0 & 0 & 0 & 1e\text{-}3 & 0 \\ 0 & 0 & 0 & 0 & 1e\text{-}1 \end{bmatrix}, \qquad R_k = \begin{bmatrix} 0.1 & 0 & 0 & 0 \\ 0 & 0.1 & 0 & 0 \\ 0 & 0 & 0.1 & 0 \\ 0 & 0 & 0 & 0.1 \end{bmatrix} \tag{C.3}$$

C.4 STSM Velocity Estimation

Leakage Estimator

$$\alpha = 1e\text{-}4, \qquad \beta = 1.2$$

$$Q_k = \begin{bmatrix} 1e\text{-}4 & 0 & 0 & 0 & 0 \\ 0 & 1e\text{-}2 & 0 & 0 & 0 \\ 0 & 0 & 1e\text{-}6 & 0 & 0 \\ 0 & 0 & 0 & 1e\text{-}4 & 0 \\ 0 & 0 & 0 & 0 & 1e\text{-}2 \end{bmatrix}, \qquad R_k = \begin{bmatrix} 0.1 & 0 & 0 & 0 \\ 0 & 0.1 & 0 & 0 \\ 0 & 0 & 0.1 & 0 \\ 0 & 0 & 0 & 0.1 \end{bmatrix} \tag{C.4}$$

C.5 Load Estimation

Leakage Estimator

$$\alpha = 1e\text{-}4, \qquad \beta = 1.2$$

$$Q_k = \begin{bmatrix} 1e\text{-}4 & 0 & 0 & 0 & 0 \\ 0 & 1e\text{-}2 & 0 & 0 & 0 \\ 0 & 0 & 1e\text{-}6 & 0 & 0 \\ 0 & 0 & 0 & 1e\text{-}4 & 0 \\ 0 & 0 & 0 & 0 & 1e\text{-}2 \end{bmatrix}, \qquad R_k = \begin{bmatrix} 0.1 & 0 & 0 & 0 \\ 0 & 0.1 & 0 & 0 \\ 0 & 0 & 0.1 & 0 \\ 0 & 0 & 0 & 0.1 \end{bmatrix} \tag{C.5}$$

Load Estimator

$$\alpha = 1e\text{-}4, \qquad \beta = 2$$

$$Q_k = \begin{bmatrix} 1 & 0 & 0 & 0 & 0 \\ 0 & 30 & 0 & 0 & 0 \\ 0 & 0 & 1 & 0 & 0 \\ 0 & 0 & 0 & 1 & 0 \\ 0 & 0 & 0 & 0 & 100 \end{bmatrix}, \qquad R_k = \begin{bmatrix} 0.01 & 0 & 0 & 0 \\ 0 & 1 & 0 & 0 \\ 0 & 0 & \frac{1e5}{2e7} & 0 \\ 0 & 0 & 0 & \frac{1e5}{2e7} \end{bmatrix} \tag{C.6}$$

C.6 Noise

Leakage Estimator

$$\alpha = 1e\text{-}4, \qquad \beta = 1.2$$

$$Q_k = \begin{bmatrix} 1e\text{-}5 & 0 & 0 & 0 & 0 \\ 0 & 1e\text{-}1 & 0 & 0 & 0 \\ 0 & 0 & 1e\text{-}6 & 0 & 0 \\ 0 & 0 & 0 & 1e\text{-}1 & 0 \\ 0 & 0 & 0 & 0 & 1e\text{-}1 \end{bmatrix}, \qquad R_k = \begin{bmatrix} 100 \cdot \frac{\pi}{180} & 0 & 0 & 0 \\ 0 & 1e4 \cdot \frac{\pi}{180} & 0 & 0 \\ 0 & 0 & \frac{2e5}{2e7} & 0 \\ 0 & 0 & 0 & \frac{2e5}{2e7} \end{bmatrix} \tag{C.7}$$

Load Estimator

$$\alpha = 1e\text{-}4, \qquad \beta = 2$$

$$Q_k = \begin{bmatrix} 1e\text{-}5 & 0 & 0 & 0 & 0 \\ 0 & 1e\text{-}2 & 0 & 0 & 0 \\ 0 & 0 & 1e\text{-}6 & 0 & 0 \\ 0 & 0 & 0 & 1e\text{-}1 & 0 \\ 0 & 0 & 0 & 0 & 1 \end{bmatrix}, \qquad R_k = \begin{bmatrix} 100 \cdot \frac{\pi}{180} & 0 & 0 & 0 \\ 0 & 1e5 \cdot \frac{\pi}{180} & 0 & 0 \\ 0 & 0 & \frac{2e5}{2e7} & 0 \\ 0 & 0 & 0 & \frac{2e5}{2e7} \end{bmatrix} \tag{C.8}$$

C.7 Sampling Frequency

Leakage Estimator

$$\alpha = 1e\text{-}4, \qquad \beta = 1.2$$

$$Q_k = \begin{bmatrix} 1e\text{-}8 & 0 & 0 & 0 & 0 \\ 0 & 1e\text{-}1 & 0 & 0 & 0 \\ 0 & 0 & 1e\text{-}6 & 0 & 0 \\ 0 & 0 & 0 & 1e{+}1 & 0 \\ 0 & 0 & 0 & 0 & 1e{+}1 \end{bmatrix}, \qquad R_k = \begin{bmatrix} 100 \cdot \frac{\pi}{180} & 0 & 0 & 0 \\ 0 & 1e4 \cdot \frac{\pi}{180} & 0 & 0 \\ 0 & 0 & \frac{2e5}{2e7} & 0 \\ 0 & 0 & 0 & \frac{2e5}{2e7} \end{bmatrix} \tag{C.9}$$

Load Estimator

$$\alpha = 1e\text{-}4, \qquad \beta = 2$$

$$Q_k = \begin{bmatrix} 1e\text{-}5 & 0 & 0 & 0 & 0 \\ 0 & 1e\text{-}1 & 0 & 0 & 0 \\ 0 & 0 & 1e\text{-}6 & 0 & 0 \\ 0 & 0 & 0 & 1e\text{-}1 & 0 \\ 0 & 0 & 0 & 0 & 1 \end{bmatrix}, \qquad R_k = \begin{bmatrix} 1e3 \cdot \frac{\pi}{180} & 0 & 0 & 0 \\ 0 & 1e5 \cdot \frac{\pi}{180} & 0 & 0 \\ 0 & 0 & \frac{2e5}{2e7} & 0 \\ 0 & 0 & 0 & \frac{2e5}{2e7} \end{bmatrix} \tag{C.10}$$

Leakage Estimation with Increased Pressure Noise

D

In this appendix the leakage estimation structure is tested at and increased pressure measure standard deviation of 1 bar. Tuning the leakage estimating UKF in the estimation structure is found to be difficult with the higher pressure noise, therefore the pressure measurements are low pass filtered, by a first order filter at a frequency of 500 Hz, to reduce noise in the signals without affecting pressure dynamics too much. In this tuning it is also found that load estimation is needed for the leakage estimate to converge.

Tuning and results for a 100 kHz sampling frequency:

Leakage Estimator

$$\alpha = 1e\text{-}4, \qquad \beta = 1.2$$

$$Q_k = \begin{bmatrix} 1e\text{-}4 & 0 & 0 & 0 & 0 \\ 0 & 1e\text{-}3 & 0 & 0 & 0 \\ 0 & 0 & 1e\text{-}6 & 0 & 0 \\ 0 & 0 & 0 & 1e\text{-}6 & 0 \\ 0 & 0 & 0 & 0 & 1e\text{-}2 \end{bmatrix}, \quad R_k = \begin{bmatrix} 100 \cdot \frac{\pi}{180} & 0 & 0 & 0 \\ 0 & 1e5 \cdot \frac{\pi}{180} & 0 & 0 \\ 0 & 0 & \frac{2e5}{2e7} & 0 \\ 0 & 0 & 0 & \frac{2e5}{2e7} \end{bmatrix} \tag{D.1}$$

Load Estimator

$$\alpha = 1e\text{-}4, \qquad \beta = 2$$

$$Q_k = \begin{bmatrix} 1e\text{-}10 & 0 & 0 & 0 & 0 \\ 0 & 1e\text{-}5 & 0 & 0 & 0 \\ 0 & 0 & 1e{+}10 & 0 & 0 \\ 0 & 0 & 0 & 1e{+}14 & 0 \\ 0 & 0 & 0 & 0 & 1 \end{bmatrix}, \quad R_k = \begin{bmatrix} 10 \cdot \frac{\pi}{180} & 0 & 0 & 0 \\ 0 & 1e5 \cdot \frac{\pi}{180} & 0 & 0 \\ 0 & 0 & \frac{4e10}{2e7} & 0 \\ 0 & 0 & 0 & \frac{4e10}{2e7} \end{bmatrix} \tag{D.2}$$

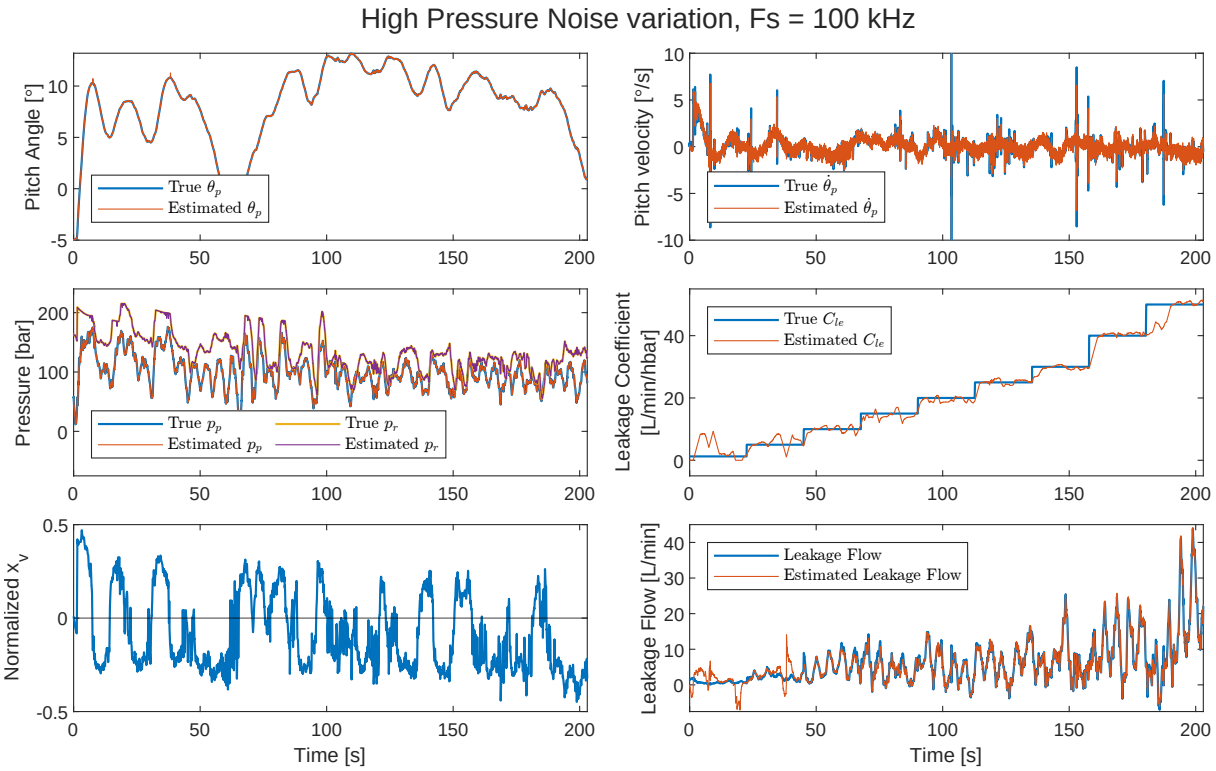

Figure D.1. Results of leakage estimation with increased pressure measurement noise, at a 100 kHz sampling frequency. The figure shows the true value of the states and leakage coefficient, as well as their estimated values from the Kalman Filter. Valve position and leakage flow is also shown.

Tuning and results for a 1 kHz sampling frequency:

Leakage Estimator

$$\alpha = 1e\text{-}4, \qquad \beta = 1.2$$

$$Q_k = \begin{bmatrix} 1e\text{-}6 & 0 & 0 & 0 & 0 \\ 0 & 1e\text{-}3 & 0 & 0 & 0 \\ 0 & 0 & 1e\text{-}6 & 0 & 0 \\ 0 & 0 & 0 & 1e\text{-}6 & 0 \\ 0 & 0 & 0 & 0 & 1e\text{-}1 \end{bmatrix}, \qquad R_k = \begin{bmatrix} 100 \cdot \frac{\pi}{180} & 0 & 0 & 0 \\ 0 & 1e5 \cdot \frac{\pi}{180} & 0 & 0 \\ 0 & 0 & \frac{2e5}{2e7} & 0 \\ 0 & 0 & 0 & \frac{2e5}{2e7} \end{bmatrix} \tag{D.3}$$

Load Estimator

$$\alpha = 1e\text{-}4, \qquad \beta = 2$$

$$Q_k = \begin{bmatrix} 1e\text{-}10 & 0 & 0 & 0 & 0 \\ 0 & 1e{+}2 & 0 & 0 & 0 \\ 0 & 0 & 1e{+}10 & 0 & 0 \\ 0 & 0 & 0 & 1e{+}14 & 0 \\ 0 & 0 & 0 & 0 & 1 \end{bmatrix}, \qquad R_k = \begin{bmatrix} 10 \cdot \frac{\pi}{180} & 0 & 0 & 0 \\ 0 & 1e4 \cdot \frac{\pi}{180} & 0 & 0 \\ 0 & 0 & \frac{4e10}{2e7} & 0 \\ 0 & 0 & 0 & \frac{4e10}{2e7} \end{bmatrix} \tag{D.4}$$

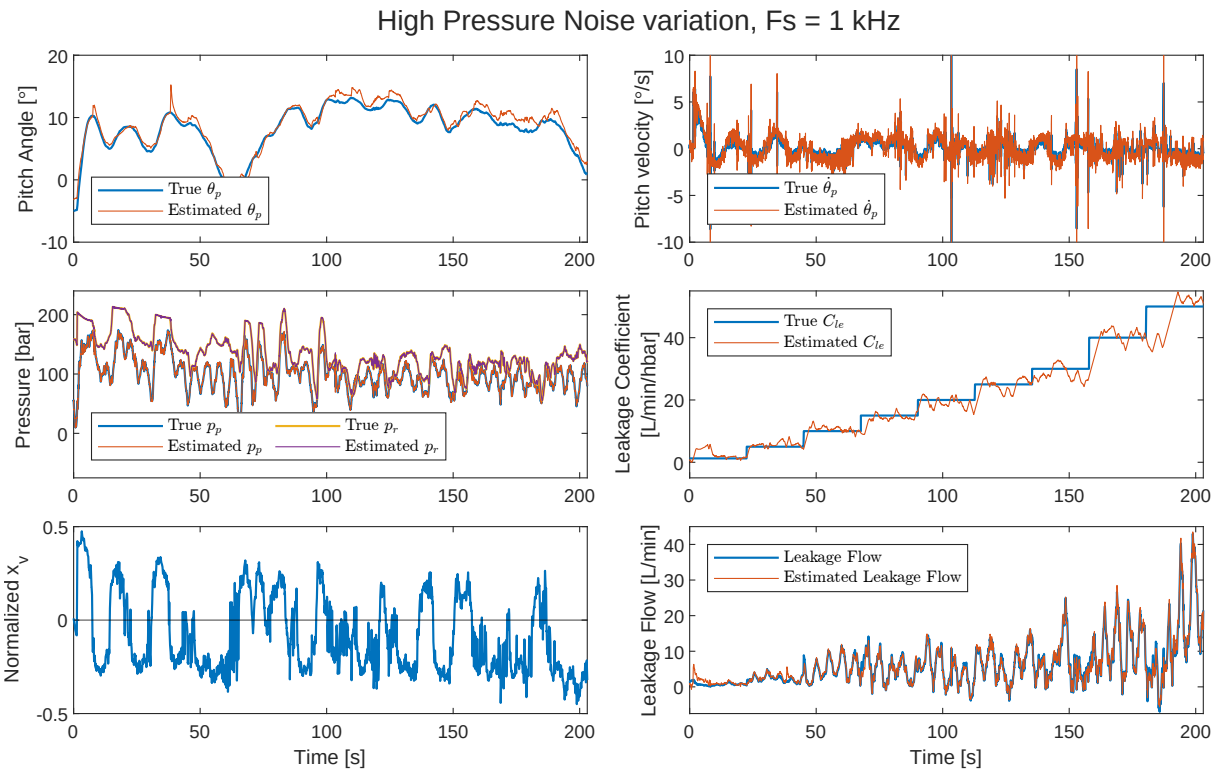

Figure D.2. Results of leakage estimation with increased pressure measurement noise, at a 1 kHz sampling frequency. The figure shows the true value of the states and leakage coefficient, as well as their estimated values from the Kalman Filter. Valve position and leakage flow is also shown.

The tunings and results shown here er not finalized, but they do show that it is possible to estimate leakage at higher levels of measurement noise on the pressure measurements.

Additional Leakage Robustness Results

E

In this appendix additional leakage estimation robustness results are shown

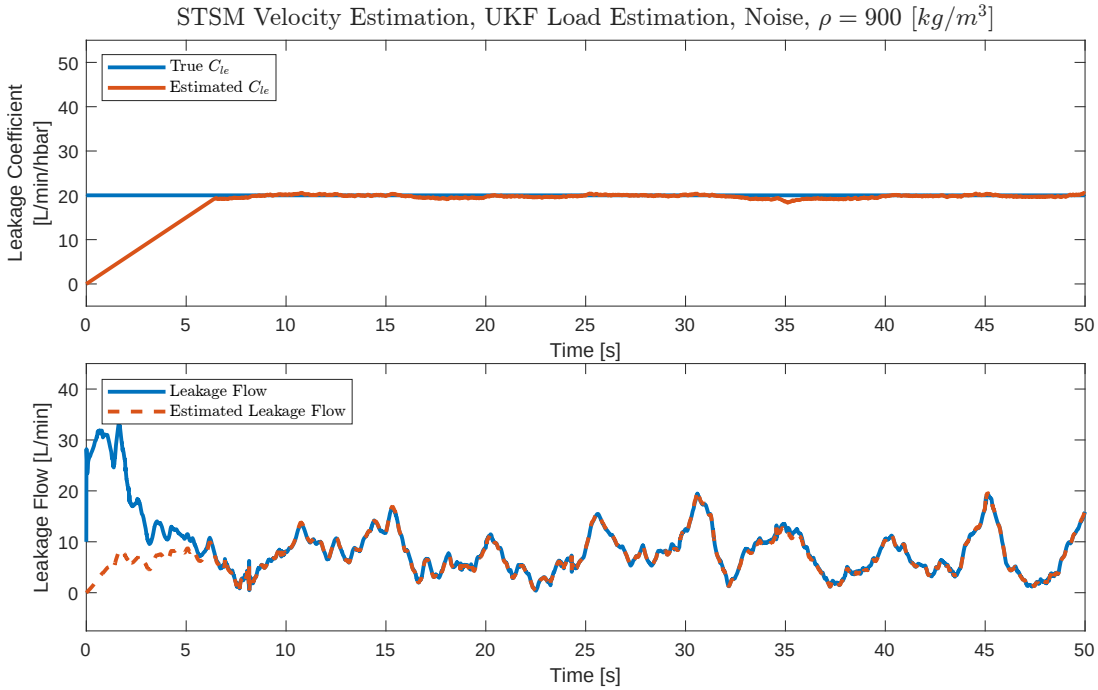

Figure E.1. Results of leakage estimation robustness test.

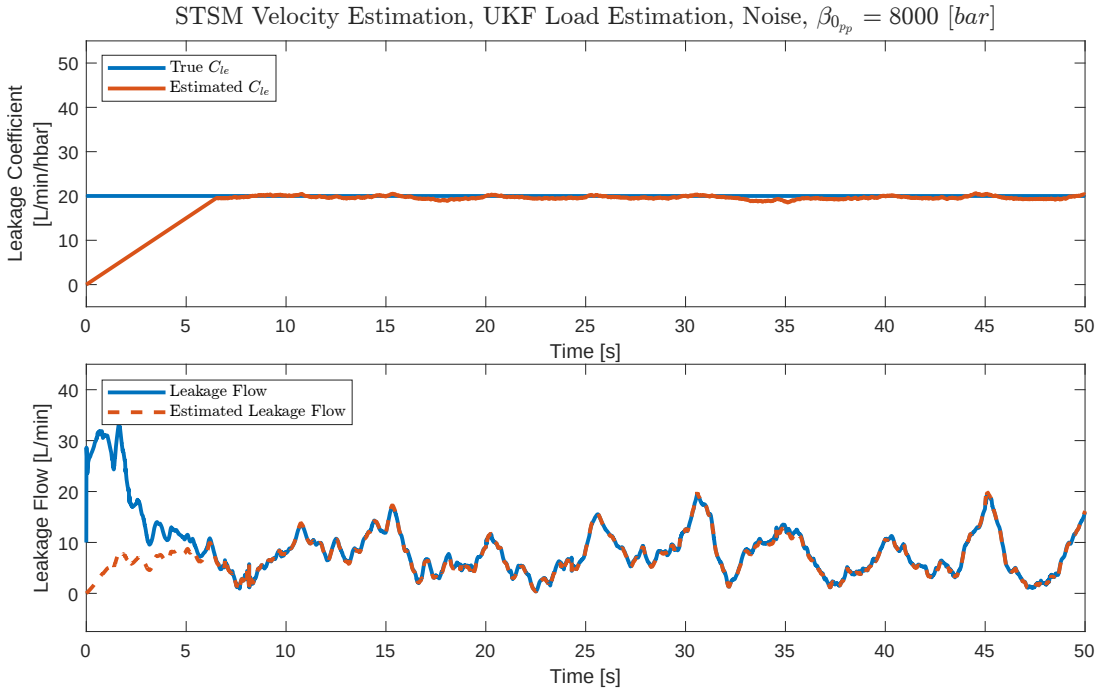

Figure E.2. Results of leakage estimation robustness test.

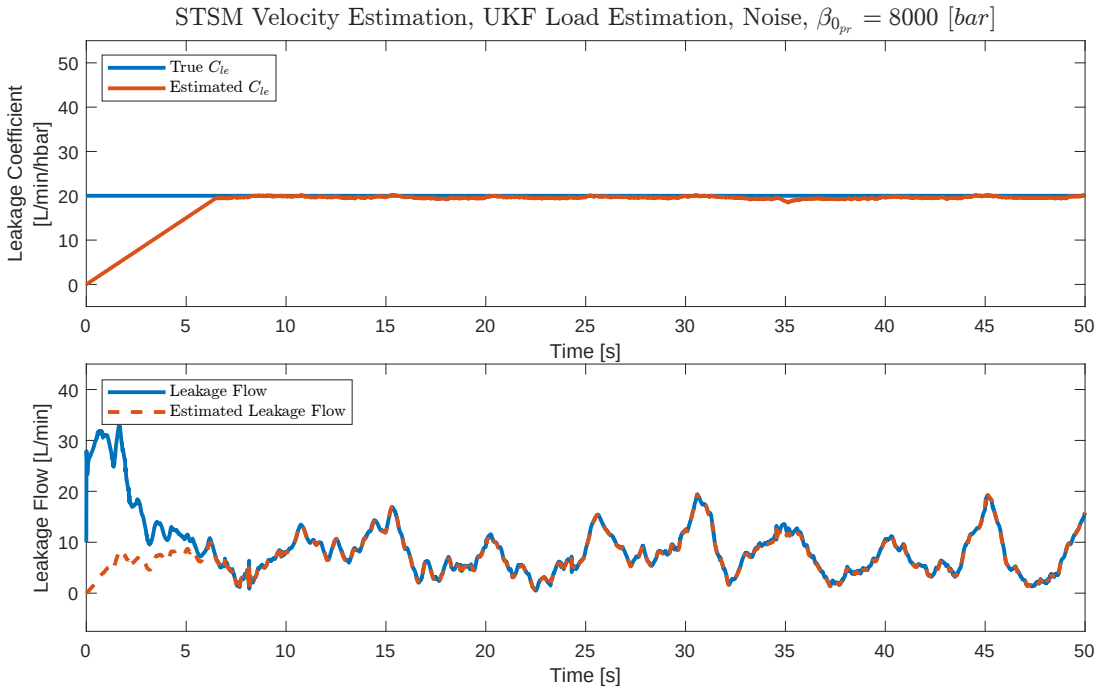

Figure E.3. Results of leakage estimation robustness test.

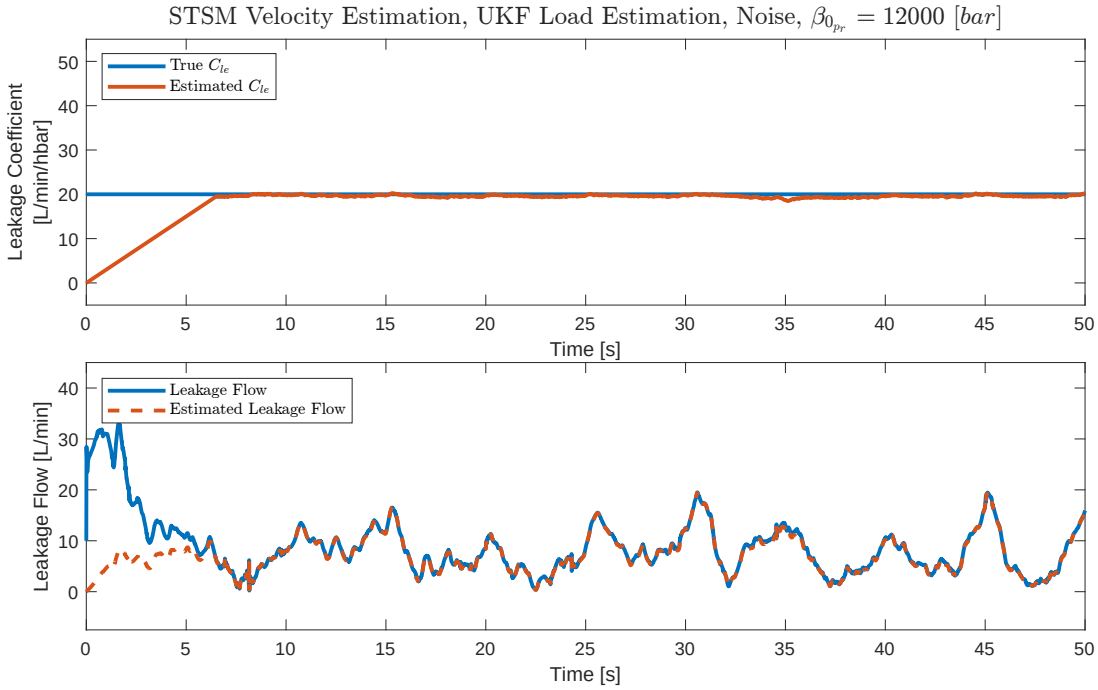

Figure E.4. Results of leakage estimation robustness test.

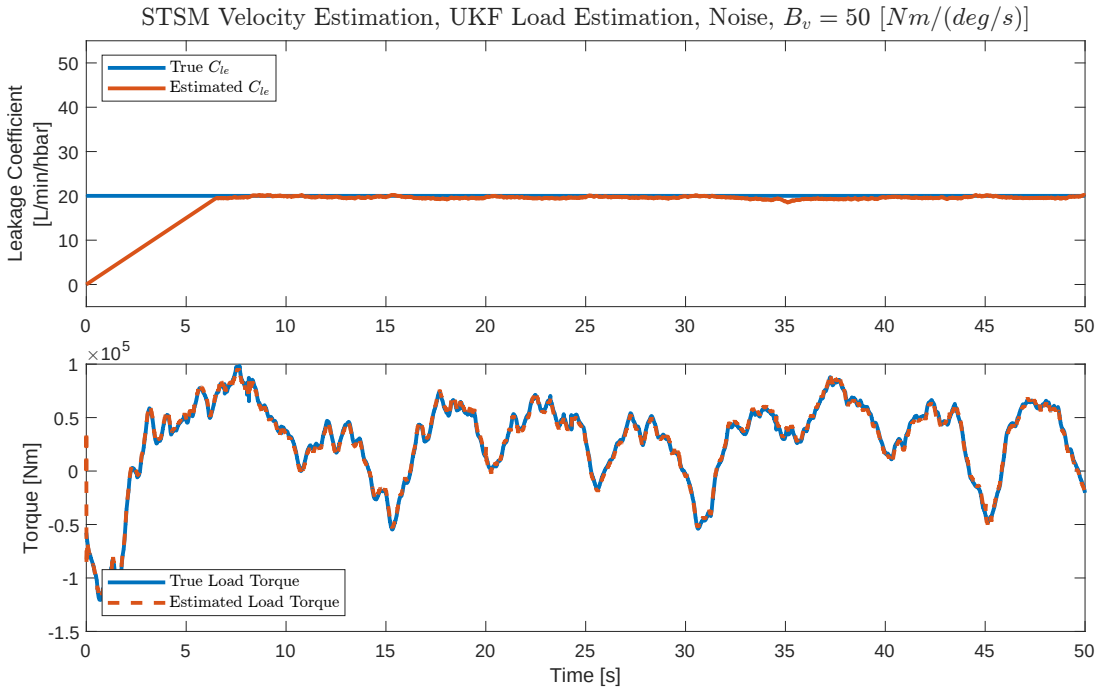

Figure E.5. Results of leakage estimation robustness test, with load estimate shown.

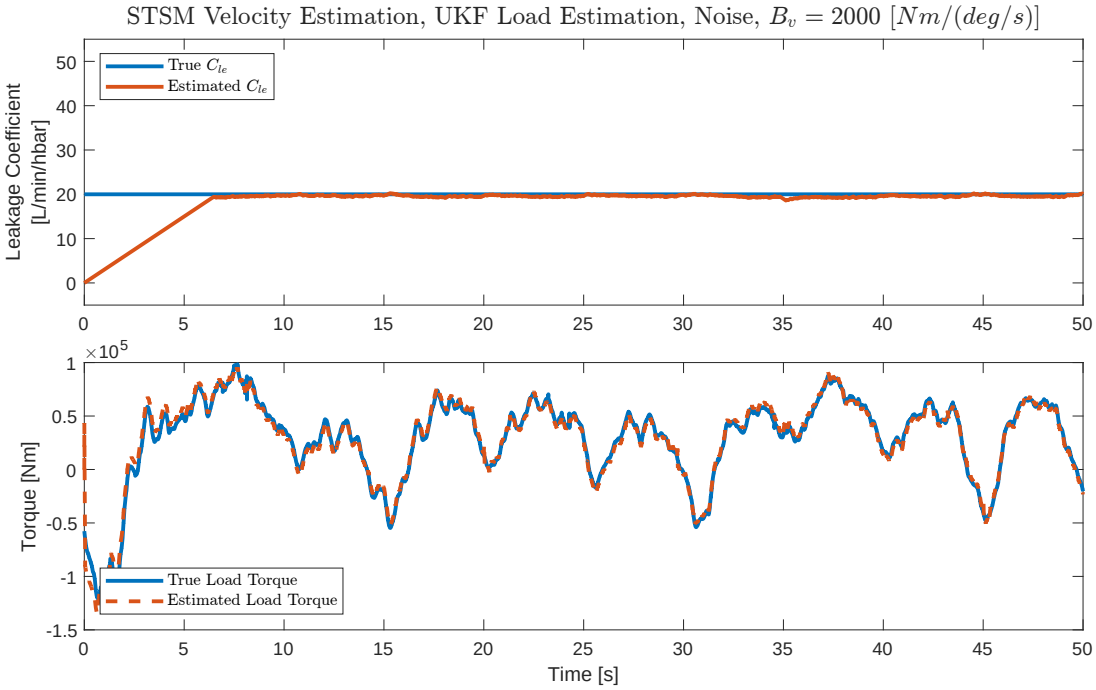

Figure E.6. Results of leakage estimation robustness test, with load estimate shown.

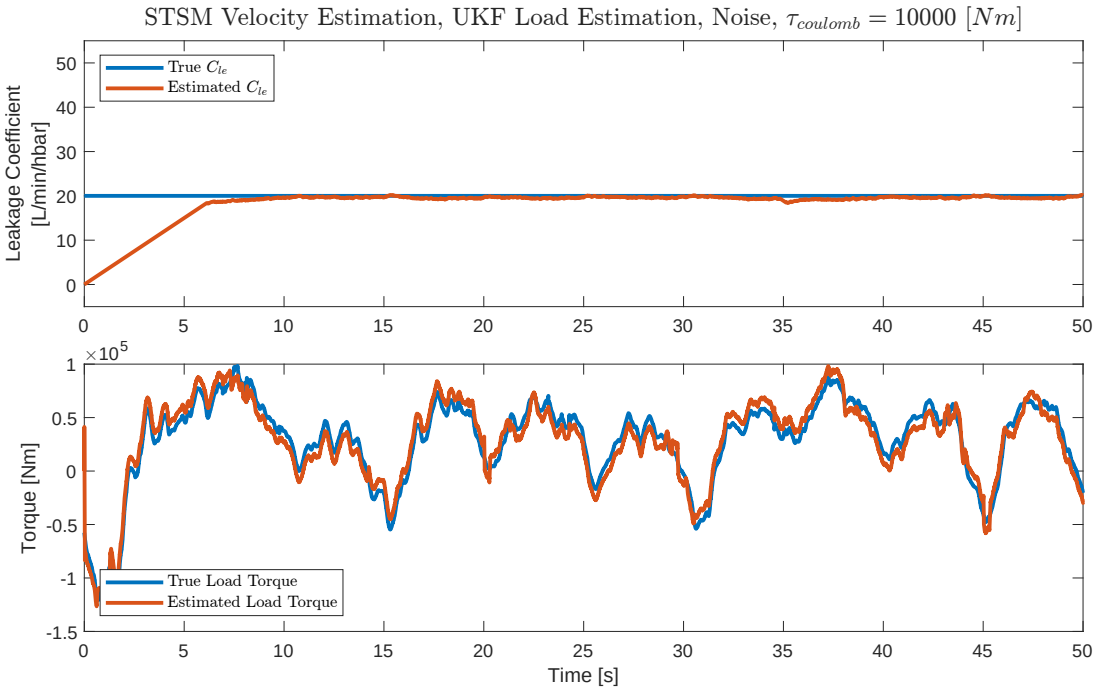

Figure E.7. Results of leakage estimation robustness test, with load estimate shown.

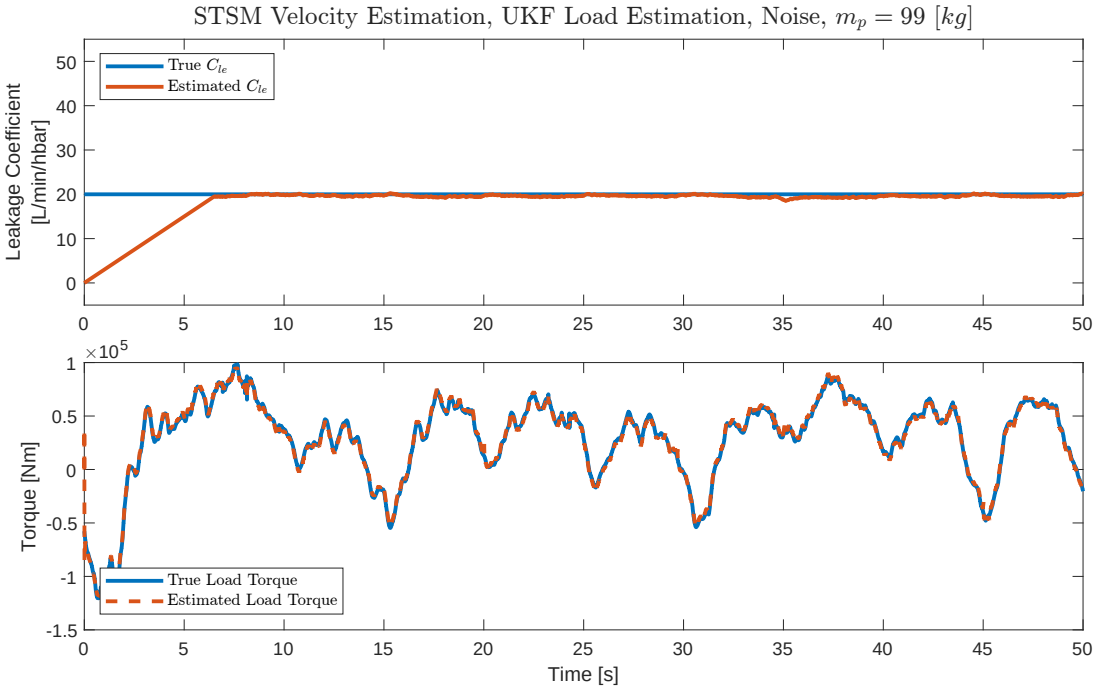

Figure E.8. Results of leakage estimation robustness test, with load estimate shown.

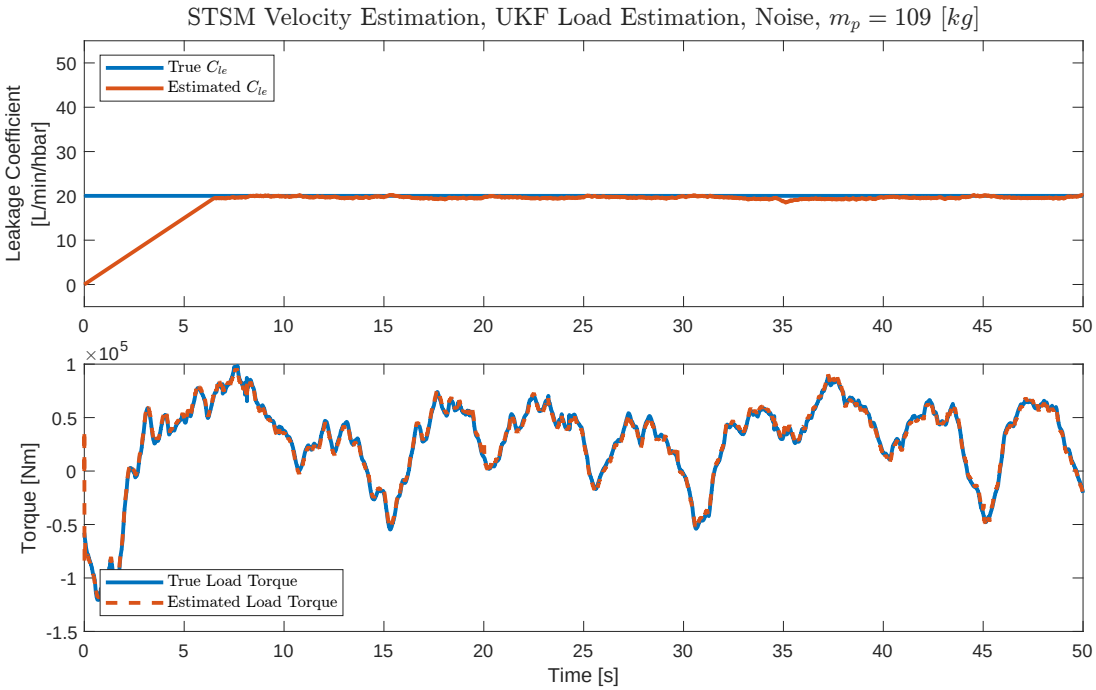

Figure E.9. Results of leakage estimation robustness test, with load estimate shown.

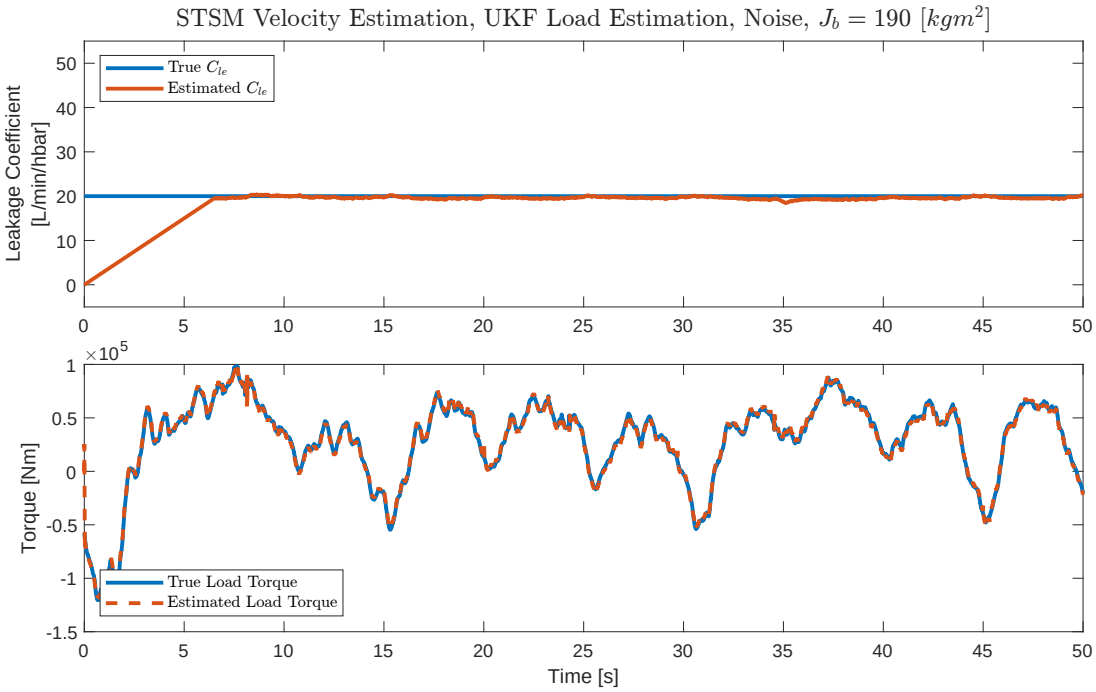

Figure E.10. Results of leakage estimation robustness test, with load estimate shown.

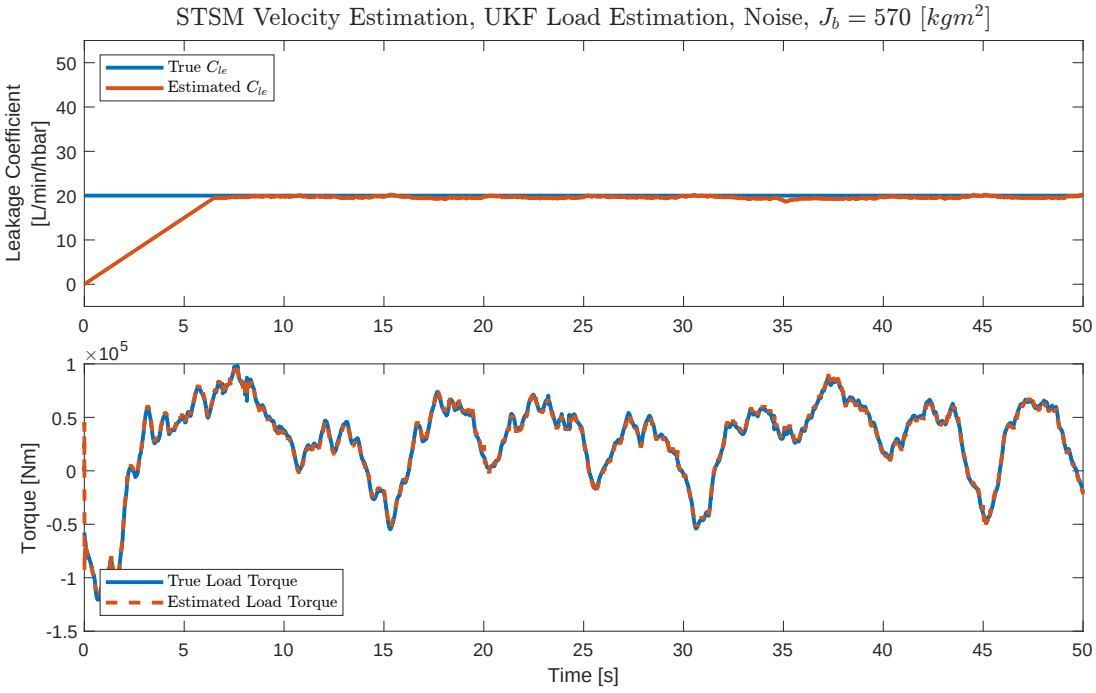

Figure E.11. Results of leakage estimation robustness test, with load estimate shown.

Additional leakage estimation Results F

In this appendix additional leakage estimation results, from the different leakage estimation tests, are shown.

F.1 Pitch Velocity Estimation

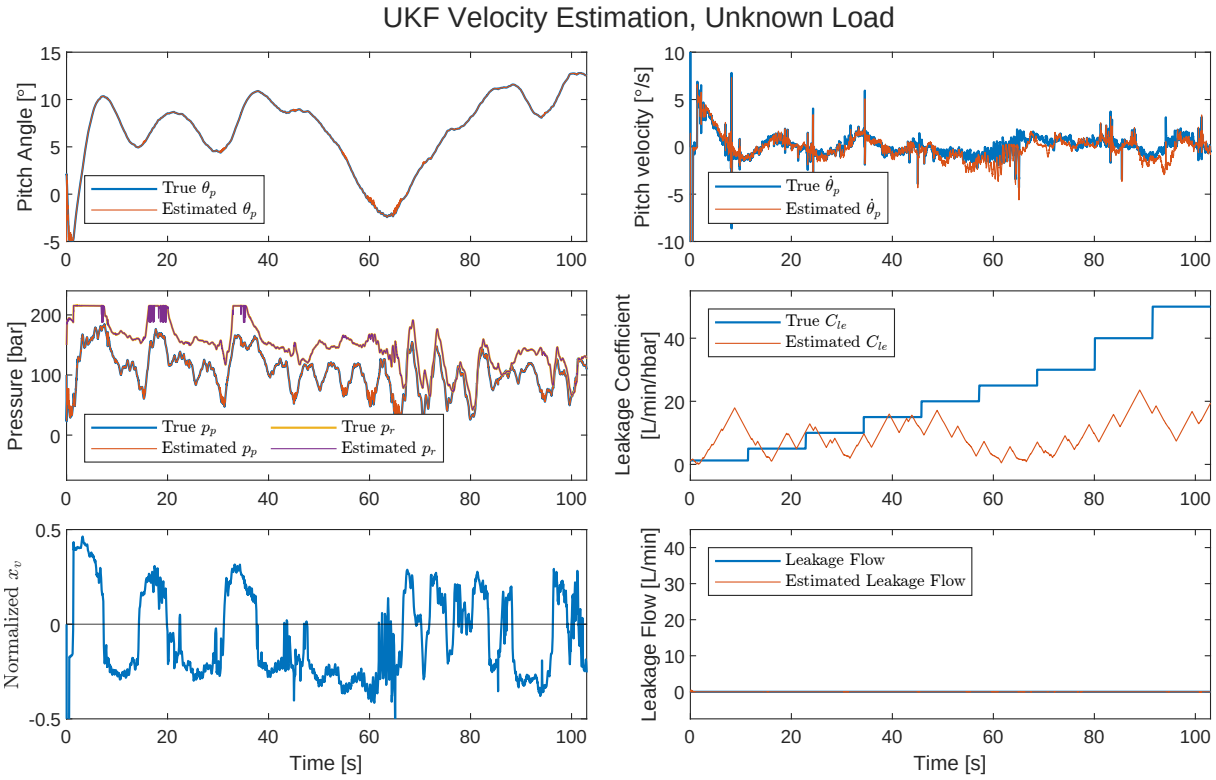

Figure F.1. Results of leakages estimation with dual estimation using an UKF, and the load torque from the wind connected. The figure shows the true value of the states and leakage coefficient, as well as their estimated values from the Kalman Filter. Valve position and leakage flow is also shown.

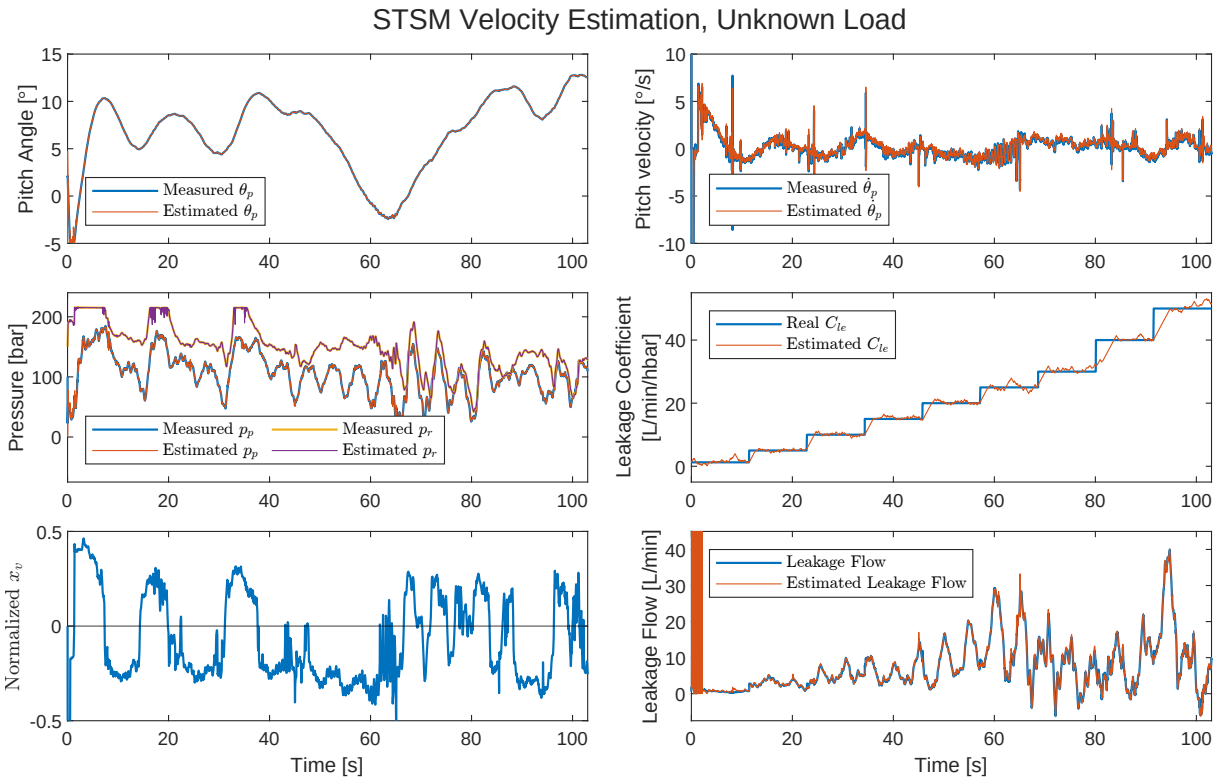

Figure F.2. Results of leakages estimation with dual estimation using an STSM observer, and the load torque from the wind connected. The figure shows the true value of the states and leakage coefficient, as well as their estimated values from the Kalman Filter. Valve position and leakage flow is also shown.

F.2 Load Estimation

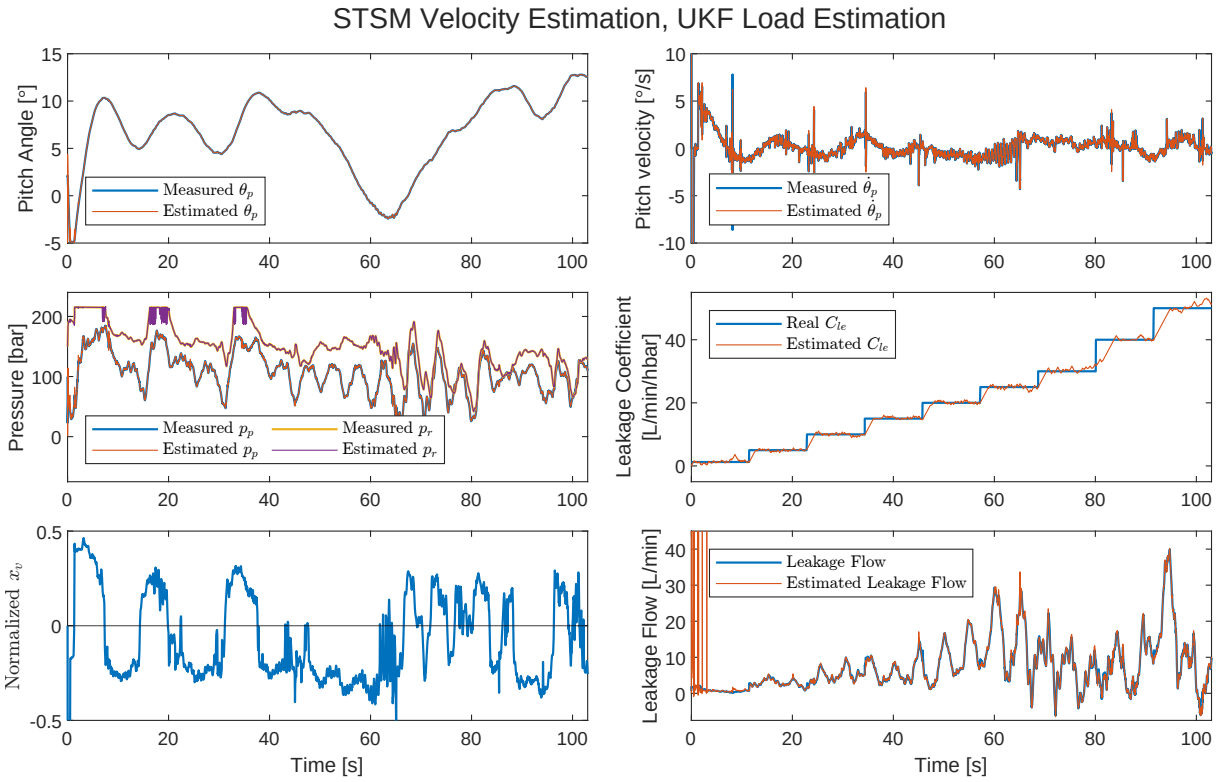

Figure F.3. Results of leakage estimation with STSM velocity estimation and UKF load estimation. The figure shows the true value of the states and leakage coefficient, as well as their estimated values from the Kalman Filter. Valve position and leakage flow is also shown.

F.3 Noise

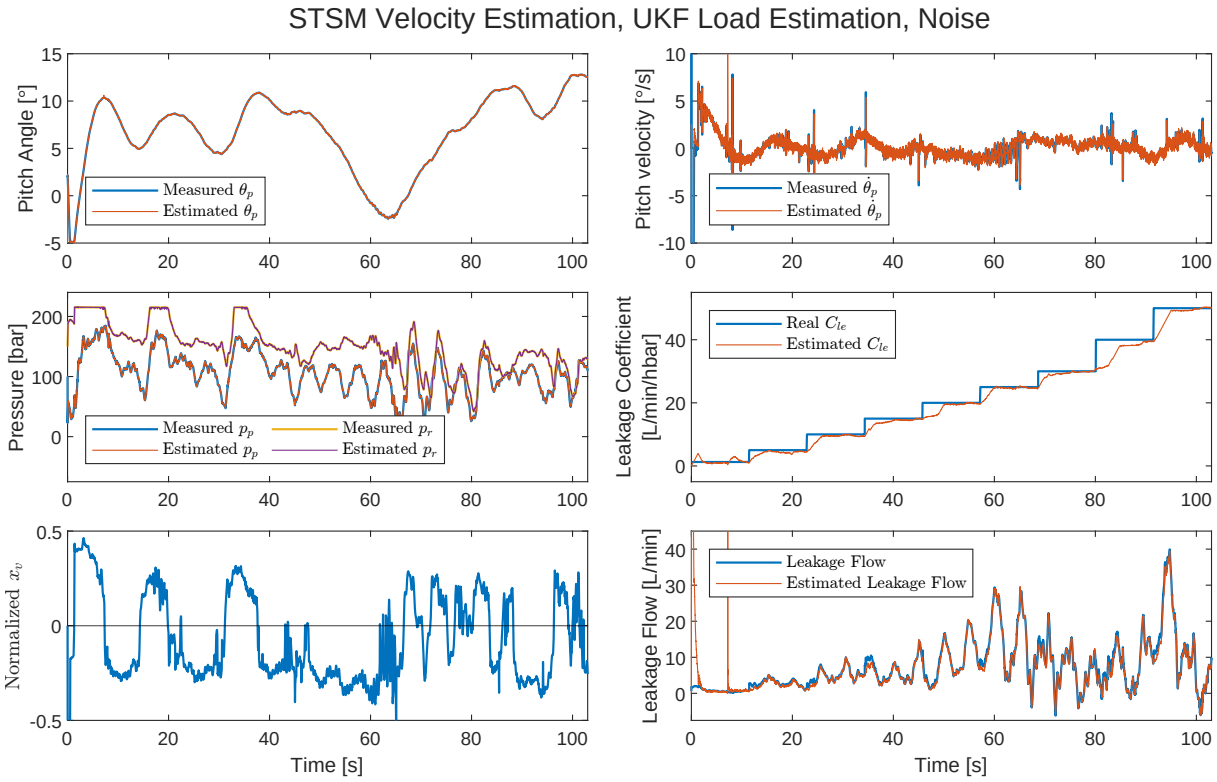

Figure F.4. Results of leakage estimation with STSM velocity estimation, UKF load estimation and noise. The figure shows the true value of the states and leakage coefficient, as well as their estimated values from the Kalman Filter. Valve position and leakage flow is also shown.